Keio University

Thesis Abstract

Registration Number	■ "KOU" □ "OTSU" No. *Office use only	Name	Chinnapat Sertthin

Thesis Title

An Indoor Positioning Architecture Based on Visible Light Communication and Multiband Received Signal Strength Fingerprinting

Thesis Summary

In this dissertation, we focus on developing a new indoor positioning architecture that does not require any extra infrastructure and has long life cycle. The study approach focuses on the following technologies; visible light communication (VLC) that uses next generation light bulb as transmitter and multiband received signal strength (MRSS) fingerprinting created from existing wireless infrastructure.

Chapter 1 presents an introduction to the localization technology. First, we explain the need of indoor positioning system, including the key performance evaluation index for positioning system. Then, we move on to introduce our proposed architect, which does not require any modification on the core equipments after being implemented. We deploy machine learning algorithms in both subsystems to ensure the system involvement throughout the system.

Chapter 2 presents VLC based positioning subsystem architecture. The detailed investigation on characteristics of VLC based positioning subsystem is presented in this chapter. Based on system characteristic, field of view (FOV) limit and sensitivity limit, we proposed a switching estimated receiver position (SwERP) scheme that can improve positioning accuracy more than 80 % over the conventional VLID system.

Chapter 3 presents an additional module that help eliminating sensitivity limit requirement to enable SwERP scheme. To be specific, nearest transmitter classification (NTC) method based on optical orthogonal code (OOC) is used instead of relying on the presence of sensitivity limit. Moreover, based on FOV limit we propose a physical layer simulation model as a reference for future simulation purpose.

Chapter 4 is the proposal on deploying frequency diversity in received signal strength (RSS) fingerprinting, denoted as multiband received signal strength (MRSS) fingerprinting, which can improve positioning accuracy of the conventional RSS fingerprinting system over 50%. The characteristics and parameters that affect the positioning accuracy are provided in this chapter.

Chapter 5 concludes this dissertation. Design and implementation guidelines are suggested based on the performance study of the proposed indoor positioning architecture. The future possible developments based on this proposed architecture are also explained.

An Indoor Positioning Architecture Based on Visible Light Communication and Multiband Received Signal Strength Fingerprinting

by

Chinnapat Sertthin

A dissertation submitted in partial satisfaction of the requirements for the degree of Ph.D. in Engineering

Keio University

1858

CALAMVS GLADIO FORTIOR
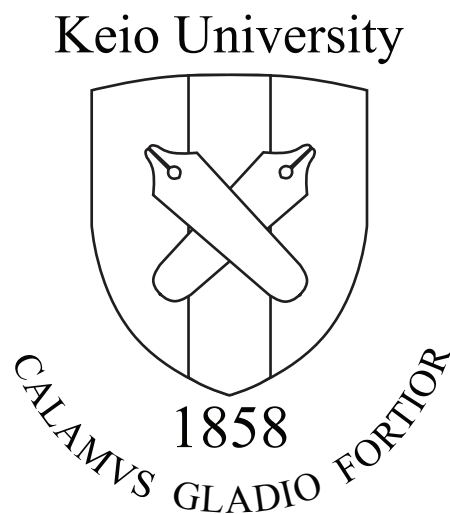
Graduate School of Science and Technology
Keio Uninversity, Yagami Campus

August 2011

**An Indoor Positioning Architecture Based on Visible Light Communication
and Multiband Received Signal Strength Fingerprinting**

Abstract

An Indoor Positioning Architecture Based on Visible Light Communication and Multiband Received Signal Strength Fingerprinting

by

Chinnapat Sertthin

Doctor of Philosophy in Engineering

Keio University, Yagami

Professor Tomoaki Ohtsuki, Chair

In the recent years positioning has become basis for a number of emerging technologies such as wide area ubiquitous network, robotics, cognitive radio and LTE release 9+. Location information can provide additional context for location-aware mobile stations. The meaning and the relevance of data can be interpreted differently as the mobile station's location changes with time. The outdoor localization can be achieved by the assist of GPS; nevertheless, GPS accuracy in indoor environment is highly degraded due to the effects of multi-path component and obstacles. Numerous of indoor positioning systems have been proposed; such as ultra wide band (UWB) system, Pseudolite that requires extra infrastructures and high complexity transceiver for synchronization due to the property of time-of-arrival (TOA) method. Therefore, indoor location determination for mobile stations imposes a significant challenge for the success of ubiquitous and pervasive wireless computing.

In this dissertation we focus on developing a new architecture that could be an eco-friendly solution for indoor positioning system that does not require any extra infrastructure, has long life cycle, and does not generate extra carbon footprint during the implementation. The proposed platform must be able to access from anywhere, anytime, anyone and anything. We focus on the high compatibility function of the proposed platform, of which can be seamlessly implemented on the existing infrastructure. In the approach we focus on the following technologies, visible light communication (VLC) and multiband received signal strength (MRSS) fingerprinting. The studied highlight system characteristic, difficulty and breakthrough.

To my late grandmother who wished to see me complete my study,
and my family for all of the love and support.

Contents

List of Figures

List of Tables

Acknowledgments

First of all, I would like to show my deepest gratitude to Panasonic Scholarship and Tokio Marine Kagami Memorial Foundation Scholarship for their kind support during my Master and Ph.D degree. I am grateful for the opportunity I was entrusted with, and being able to contribute back to the society through this research. I wish that this research can improve many people's quality of life, and can be utilized as foundation for location base service very long time. This dissertation has been a long journey. I will not be able to complete this journey with kind support from my colleagues, professors and family.

I wish to acknowledge following group of people whom had utmost helped me on my early research life. Firstly, my previous Professor Masao Nakagawa who spent a lot of time teaching me how to do research, and also giving full authority to me on collaboration work with NTT Innovation Laboratory. Prof. Kobuta and Dr. Kuwano from NTT Network Innovation Laboratory who scarify their time coming to research meeting every month at Keio University. Ass. Prof. Takeo Fujii, Ass. Prof. Ousamu Takyu, and Prof. Yohtaro Umeda who had been assisting me from the very begging until my graduation. My dearest research fellows Dr. Koichi Adachi, thank you very much for teaching me many thing from research to Japanese culture, and previous Nakagawa laboratory's members especially Ms. Emiko Tsuji who had help me so much to understand Japanese working culture.

It is very unfortunate that Prof. Nakagawa had early retire due to his health condition. I would like to express my gratitude towards Prof. Tomaki Ohtsuki who had wonderfully take care of me since Professor Nakagawa retirement. I am indebted to his diligence in constantly stimulating me towards the completion of this dissertation. Furthermore, I would also like to express my gratitude for the panel who examined this dissertation, Prof. Iwao Sasase, Prof. Yukitoshi Sanada, and Prof. Hiroshi Shigeno. Their critical review and constructive suggestions added an extra layer of polish to this dissertation.

I would also like to express my appreciation to every professors and staffs in the GCOE program, especially Ms. Maki Adachi, Ms. Yuko Izuta, and Ms. Chinatsu Ichikawa. My fellow Research Assistants (RAs) in the GCOE program, Ass. Prof. Mamiko Inamori, Dr. Maduranga Liyanage, Dr. Alex Fung, and Mr. Oussama Souihli for the stimulating research discussions that helped give my research some perspective. As a member of Ohtsuki Laboratory, I would also like to take advantage of this opportunity to express my thanks towards my other colleagues for their support and encouragement. Particularly, Mr. Jihoon Hong and Mrs. Norharyati Binti Harum for their kind assistances on every aspect. Last but not least, I wish to express my heartfelt thanks to my family who have always been a great source of support and encouragement for me.

Chapter 1

Introduction

In the recent years positioning has become basis for a number of emerging technologies such as wide area ubiquitous network [1], robotics, cognitive radio [2] and LTE release 9+ [3]. Location information can provide additional context for location-aware mobile stations. The meaning and the relevance of data can be interpreted differently as the mobile station's location changes with time [4]. The outdoor localization can be achieved by the assist of global positioning system (GPS); nevertheless, GPS accuracy in indoor environment is highly degraded due to the effects of multi-path component and obstacles. Numerous indoor positioning systems have been proposed; such as ultra wide band (UWB) system, Pseudolite that requires extra infrastructures and high complexity transceiver for synchronization due to the property of time-of-arrival (TOA) method. Therefore, indoor location determination for mobile stations imposes a significant challenge for the success of ubiquitous and pervasive wireless computing.

Positioning estimation or location determination refers to a process used to obtain location information of a mobile station (MS) with respect to a set of reference positions within a predefined space. In many literatures, this process is usually also widely known as radiolocation [4], position location [5], geolocation [6], location sensing [7], or localization [8]. This dissertation will primarily use positioning but all of these terms are also used interchangeably throughout the document. A system developed to determine or estimate the location of a targeting unit is called a positioning system. The term positioning system will be used to represent the system throughout this document. An existing infrastructure refers to a previously installed infrastructure for the other purpose such as light bulb for the purpose of illumination, mobile phone infrastructure or wireless local area networks (WLANs), for the purpose of communication. An emerging wireless infrastructure refers to the future wireless technology infrastructure that will be implemented for communication purpose to its subscribed user. A set of coordinates or reference points within the predefined space is typically used to indicate the physical location of the entity. For example, an indoor positioning system may include position information such as a floor number, a room number, and other reference objects to represent an entity's position.

In this dissertation we focus on developing a new architecture that could be an eco-friendly solution for indoor positioning system that does not require any extra infrastructure, has long life cycle, and does not generate extra carbon footprint during the implementation. The proposed platform must be able to access from anywhere, anytime, anyone and anything. We focus on the high compatibility function of the proposed platform, of which can be seamlessly implemented on the existing infrastructure. In the approach we focus on the following technologies, visible light communication (VLC) and multiband received signal strength (MRSS) fingerprinting. The studied highlight system characteristics, difficulty and breakthrough solution. First, this chapter presents the background of indoor positioning systems, identifies the challenges of such systems, and briefly describes indoor positioning systems. Next, the assumptions of study, the overview of approaches, and the contributions are presented. Finally, the organization of this dissertation is outlined.

1.1 Background of Indoor Positioning Systems

The success of location service technologies provides an incentive to the research and development of indoor positioning systems. Most of the outdoor location based services such as Google Map or Foursquare[1] are provided based on GPS system support. Unfortunately, the GPS system cannot be used effectively inside buildings and in dense urban areas owing to the reasons explained in the preceding context. As the result, many divertive technologies are being developed. As a result, indoor positioning systems require alternative means to detect the MS's location without relying on the direct radio frequency (RF) signal from GPS satellites. Infrared, RF, and ultra sound signals are major technologies used for indoor positioning systems [6]. Different types of sensors are required to detect these signals depending on its characteristics. Such as, a photodiode is used as a sensor to detect signals that lie in the range of infrared to visible light. Sensors process the received signal and convert by the selected algorithm into quantifiable metric such as distance or latitude and longitudes for later location determination [6]. Unlike outdoor areas, the indoor environment imposes different challenges on location discovery due to the dense multipath effect and building material dependent propagation effect. Thus, an in-depth understanding of signal characteristic for positioning is crucial for efficient design and implementation.

Concurrently, there has been an increasing deployment of new wireless infrastructures such as WLANs, digital terrestrial broadcasting system (DTBS), Worldwide Interoperability for Microwave Access (WiMax), and femtocell for mobile communication by many organizations. Thus, the popularity of wireless infrastructure opens a new opportunity for location-based services. In addition to wireless infrastructure, smart ambient environment is enabled by visible light communication (VLC) is also attracting many attentions. The focus of this dissertation is to enable new indoor positioning system architecture based on VLC and wireless technology without deploying additional infrastructure. We consider a terminal

---

[1]Foursquare is a location-based social networking website based on hardware for mobile devices.

that poses VLC and multi-frequency band capability as a kind of sensor device. Location information has become a mandatory requirement for many emerging technologies such as cognitive radio and LTE release 9+ [3]. We are convinced that our proposed architecture can possibly become a prevalent solution for many emerging technology of the future. Krishnamurthy [4] identifies four areas of challenges in position location in mobile environment which are performance, cost and complexity, security, and application requirements. We elaborate our proposed architecture with the preceding issues are elaborated as follows.

- **Performance:** Accuracy is the most important metric used to evaluate performance of positioning system; usually error distance between the estimated location and the actual mobile location. The report of accuracy should include the confidence interval of the estimated distance error. Other essential performance metrics are delay, coverage, scalability and capacity of the positioning system. The delay metric refers to the time taken between sensing of the location to reporting the information. The capacity metric measures the number of location estimations that a system can process per unit time. The coverage metric reports the boundary of a space that location information can be estimated. Scalability is a metric that suggests how well the system performs when it operates with a larger number of location requests and a larger coverage [9]. The proposed architecture uses existing infrastructure, of which are installed everywhere. Therefore, low delay, high coverage, scalability and capacity can be achieved. Details of the proposed architecture are described in chapters 2 to 4.

- **Cost and Complexity:** The cost incurred by a positioning system can come from the cost of extra infrastructure, additional bandwidth, fault tolerance and reliability, and nature of deployed technology. The cost may include installation and survey time during the deployment period. Our proposed architecture utilizes purely existing infrastructure. Thus, implementation cost, and communication bandwidth can be saved. Moreover, existing communication signals can also be used for location sensing. After the system becomes operational, the extra power consumption at each mobile can be considered as a cost for the positioning system [9]. However, the proposed architecture solely uses existing infrastructure, only marginal power consumption is increased from additional positioning server that we introduce as shown in Fig. 4.1. The complexity of the signal processing and algorithms used to estimate the location is another issue that needs to be balanced with the performance of positioning systems. Trade-off between the system complexity and the accuracy affects the overall cost of the system. Therefore, we use only low-complexity algorithm to illustrate the advantage of the proposed architecture.

- **Application Requirements:** There are three major application requirements for the location information, the granularity, the performance, and the availability. All of which, we had explained in the preceding parameters. The necessities are depending

on the type of application. Firstly, the granularity can be classified into temporal granularity and spatial granularity. Temporal granularity determines the frequent at which the location information is requested, while spatial granularity indicates the level of location information detail. Secondly, the performance requirements can be the combination of any performance metrics discussed above. Based on the types of applications, the requirement of location information entities may be different. For example, utilizing position information at a centralized server is more appropriate for application such as user tracking. Based on the entity that estimates the location information, there are two approaches for location systems: self-positioning and remote-positioning [4].

- **Security:** Users privacy is one of the most important issue for mobile user, the position of any mobile user can be easily inquire via remote-positioning. Thus, location information should be made available only to those with authorized access. It is also related to how the system determines the location information and the type of application. For example, GPS device can derives its own position from the GPS satellites which is completely. On the other hand, a location tracking such as the E-911 system [10] with the main purpose to capture the user location can be misused by unauthorized groups if there is no security protection in place. Thus, the location system requires security protocol embedded within the system to protect the location information. Unfortunately, the security of the system is limited by the location sensing technique. For instance, a positioning system that reuses the communication signals for the purpose of location detection cannot completely secure the MS's privacy because of its active nature [9].

1.2 Principle of Localization Technology

The need to locate people and objects as soon as possible have always been an important part of many organizations and industries, such as in robotic, telemetry and logistics. With the increasing sophistication of wireless technology, it is now possible to remotely locate objects or people within a predefined time frame.

In this section, we discuss types and techniques used in localization technology. The type of localization technology can be majorly classified by either the access methods or measurement classes. Both types based on the same technique which are either ranges or angulations [11].

1.2.1 Access Methods

The access method can be classified in to three major types, which are received signal based, time of arrival based and angle of arrival based types. Three of which can be used to explain any localization technology that enable distance measurement, and estimated location from

analysis of specific physical characteristic. Details of each access method are provided as follows and also in Table 1.1. We use all of the mentioned access methods advantages to compromise their disadvantage and create solution architecture for indoor positioning that can fully operate in any environment. Details of how we utilize each access method in our proposed architecture are provided in section 1.6

Received Signal Strength (RSS)

The signal strength of received signals from at least three transmitters are used to determine the location of the object or person being tracked. The greatest advantage of RSS method is that the accuracy of the system is irrelevant with modulation scheme, and system bandwidth. We use this access method as one of key technology to enable our proposed platform solution.

Time of Arrival (TOA)/Time Difference of Arrival (TDOA)

Both TOA and TDOA are based on time access method, which use measured elapsed time for a transmission between a transmitter and a receiver. TOA method is based on the exact time difference between transmitters and receiver. Therefore, synchronization between transmitters and receiver becomes significantly important. On the other hand, TDOA method is based on time differences from transmitters to receiver, only synchronization among transmitters is required. Moreover, the system bandwidth has direct impact on positioning accuracy in multipath environment.

Angle of Arrival (AOA)

This method is for determining the direction of propagation of a received signal. By using direction sensitive antennas on a receiver, the direction to a transmitter can be obtained. In practical wireless systems, the measurement of the difference in received phase at each element in the antenna array is used for calculating AOA. In our proposed platform AOA is achieved by the embedded 6-Axis sensor that provides angulations information.

Table 1.1: Comparison of advantage and disadvantage among access methods

Method	Advantage	Disadvantage
TOA	High positioning accuracy can be achieved	Achievable accuracy is depended on system bandwidth
AOA	Generally used with TOA method to enhance positioning accuracy	More than one transmitters are required to perform AOA
RSS	Achievable accuracy is irrelevant with system bandwidth and modulation types	Low positioning accuracy owing to multipath reflections and interferences

1.2.2 Measurement Types

Distance measurement has two major classes, which are instantaneous measurement and fingerprinting method. The major difference between both classes is an instantaneous measurement estimate position based on prior knowledge of source location with only one time measurement. On the other hand, fingerprinting method does not require the prior knowledge of the transmitters' coordination. Premeasured of desired signals must be conduct to create the database in relationship to coordinate in the usage area, which will be used to estimate position.

Instantaneous Measurement

Instantaneous measurement refers to detection of a mobile terminal by a single measurement within signal range of a fixed location so that the mobile is known to be within an area around that location. The measured accuracy of this class is lower than the other due to the effects of multipath and Doppler effects. However, it is the most popular measurement class because pre-measurements of the desired signals are not required.

Fingerprinting (Database)

RSS fingerprinting, or radio map [12], uses the statistical approach. Rather than estimating distance to the transmitters and performing triangulation to estimate position, RSS fingerprinting estimates positions by recognizing correlation between measured RSS and the premeasured RSS database; denoted as fingerprint. Therefore, exact locations of the wireless infrastructures are not required. RSS fingerprinting consists of two phases, which are training and positioning phases. In the training phase, fingerprint of each location is created as reference database. In the positioning phase, the instantaneous measured RSSs are compared to the fingerprint, from the training phase to estimated location.

1.2.3 Techniques in Positioning System

Four geometric arrangements for calculating location coordinates by the combination of basic measurements of distances, (ρ) and angulations (θ) are described

Distance (ρ) and Angulations (θ)

When both direction finding and distance measurement capability are available, only one terminal is needed to determine the position coordinates of the target as shown in Fig. 1.2. The target is located on the intersection between a circle whose radius is ρ, the distance between fixed terminal T_x and target R_x, and a bearing line that is at an angle of θ referenced to north.
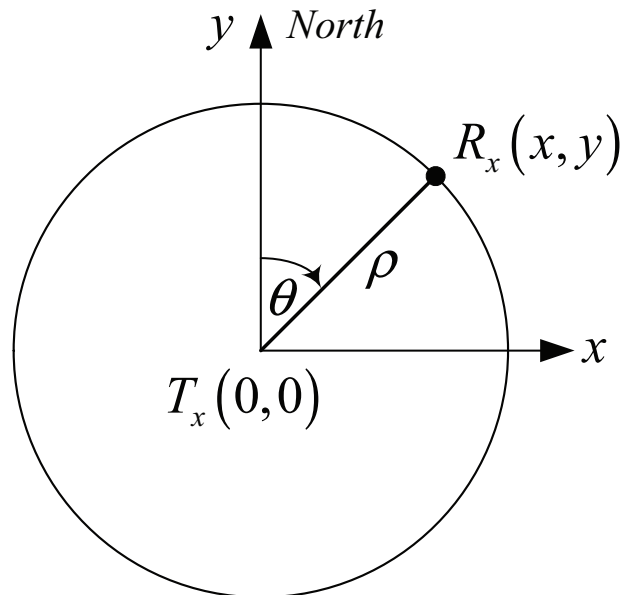
Figure 1.1: Rho-Theta location measurement configuration

If the distance is estimated by RSS the perimeter line may result as a contour rather than circle. Coordinates of R_x can be derived as

$$x = \rho \cdot \sin(\theta), \ y = \rho \cdot \cos(\theta) \tag{1.1}$$

Two Angulations (θ)

Directional antennas can be used at two or more fixed terminals to find target location when the coordinates of the terminals are known relative to a reference point. The geometric procedure for calculation location is called triangulation. The advantage of this method is that synchronization and modulation type have no impact on positioning accuracy. When coordinates of T_{x1} and T_{x2} are known, the angles of arrival, θ_1 and θ_2 of the signal reference clockwise from north are measured; as in Fig. 1.2. Coordinate of R_x can be derived as

$$x = y \cdot \tan(\theta_1), \ y = \frac{y_2 \cdot \tan(\theta_2) - x_2}{\tan(\theta_2) - \tan(\theta_1)} \tag{1.2}$$

Spherical Curves

Time-of-arrival (TOA) location is determined by trilateration using distance data only. Distance can be estimated using received RSSI data or time-of-flight (TOF) measurements, where the transmitter and receiver must have synchronized clocks. In this method, three or more fixed positions are required.
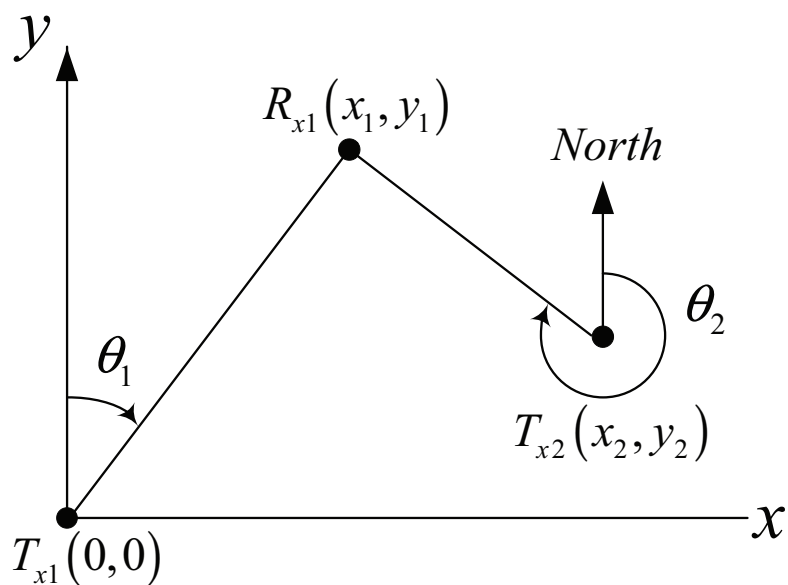
Figure 1.2: Theta-Theta location measurement configuration
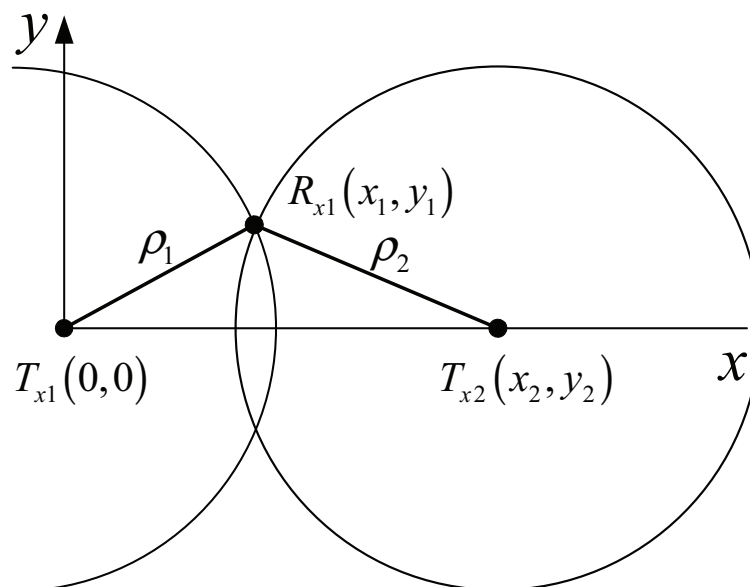
Figure 1.3: Rho-Rho location measurement configuration

Regarding Fig. 1.3, if we can find the distances ρ_1 and ρ_2, we can determine the location of R_x from the intersection points of two circles. If there is no other knowledge to eliminate the ambiguity, a third fixed terminal is required.

In the case of TOA, assuming that all of the transmitters are synchronized, the one-way distance between R_x to T_{x1} or T_{x2} can be derived from relationship between propagation speed of light, c, and receive times, t. The transmission time is defined as t_0, and received time from T_{x1} and T_{x2} are t_1 and t_2 consequently.

$$\rho_1 = (t_1 - t_0) \cdot c, \ \rho_2 = (t_2 - t_0) \cdot c \tag{1.3}$$

The equations of the two circles are

$$\rho_1^2 = x^2 + y^2, \ \rho_2^2 = (x - x_2)^2 + (y - y_2)^2. \tag{1.4}$$

These two nonlinear equations can be solved to find x and y.

Hyperbolic Curves

Hyperbolic curves are used in time difference of arrival (TDOA), which has the advantage over TOA on synchronization. In TDOA method synchronization among fixed transmitters and receiver are not required [11][13]. Nevertheless, the achievable accuracy is low, comparing with TOA method.

The TDOA method uses time difference in the reception of that starting point at the several fixed transmitter, not the actual TOF of the signal from the target to the fixed stations. Therefore, one time difference value is not enough to calculate the two coordinate values of the receiver position. Thus, in order to have sufficient data to find receiver's coordinate, TDOA requires one more reference station than TOA. Geometric layout of TDOA in two dimensions is shown in Fig. 1.4, the clock of T_{x1} and T_{x2} are synchronized but R_x's clock is not. So, t_0 is unknown. The difference of the distances between the two fixed stations and the target is $d = d_2 - d_1 = c(t_2 - t_1)$. The locus of points of d is a constant, which described hyperbola. Thus, the estimated position is located somewhere on that hyperbola. The expression for the hyperbola is

$$\frac{x^2}{a^2} - \frac{y^2}{b^2} = 1. \tag{1.5}$$

Expressing a and b in terms of the known quantities Δd and D, we have

$$a^2 = (\Delta d/2)^2 \tag{1.6}$$

$$b^2 = \left(\frac{D}{2}\right)^2 - a^2 \tag{1.7}$$

The equations (1.5)−(1.7) are not sufficient to find the coordination of the receiver. Hence, the time of arrival at a third fixed transmitter, T_{x3}, is needed to pinpoint the target location.
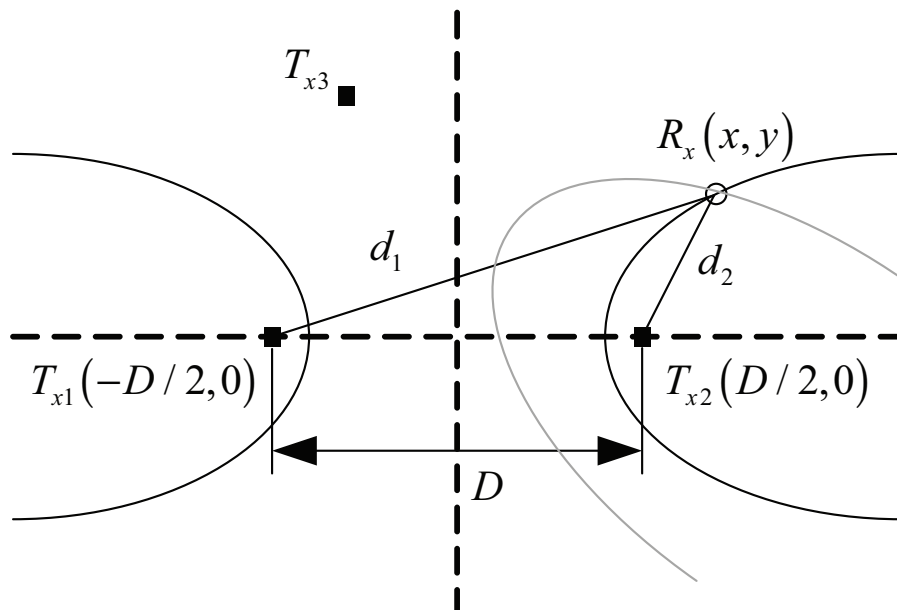
Figure 1.4: Geometry of TDOA location method

1.2.4 Limitations

Normally, distance measurement system design involves compromises among parameters of accuracy, bandwidth, clock rate, measurement time, and complexity. High accuracy in a short time needs a high clock rate and consequently high bandwidth. A large bandwidth, in turn, means greater noise power and reduced range and high clock rates increase complexity and current consumption, and cost.

In this subsection, the basic terms and factors those have effect on positioning system are introduced. The ability to use radio transmission for distance measurement, and the estimated location accuracy that can be achieved depend on basic parameters of the signal, as well as the nature of its propagation.

Time Resolution

Figure 1.5 expects that the initiator's time base clock has been added. A pulse is transmitted and the time interval until reception is measured. The distance resolution is directly proportional to the period of the clock. The one-way distance resolution, Δd, of a pulse signal with a 100MHz clock can be calculated as follows.

$$T_c = 1/100 \text{ MHz} = 10 \text{ ns}, c = 3 \cdot 10^8 \text{ m/s}$$
$$\Delta d = (T_c \cdot c) = 3 \text{ m} \tag{1.8}$$

In case of radar system assuming the same configuration, (1.8) must be divided by 2 to
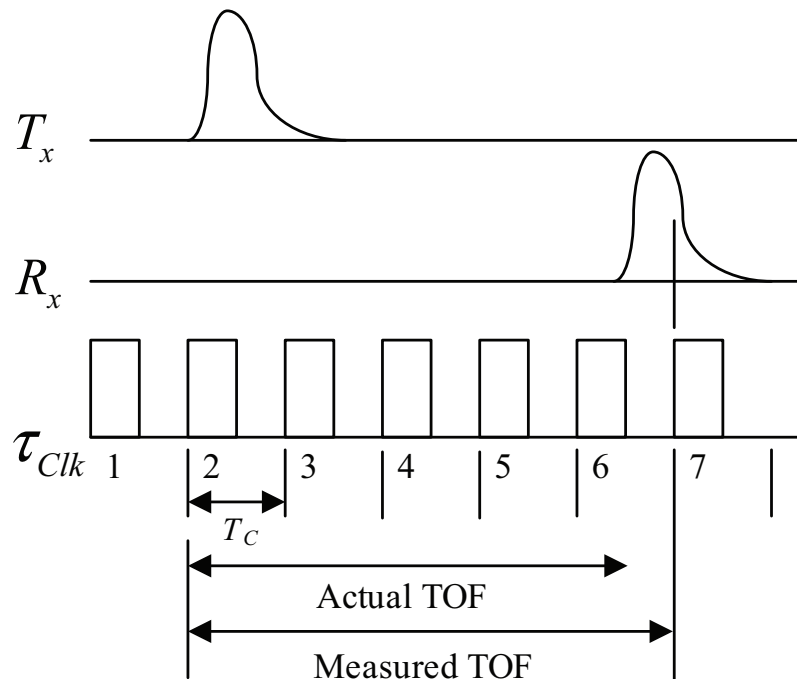
Figure 1.5: Illustration of time resolution (τ_{clk})

find the one-way distance resolution, Δd, as in (1.9)

$$\Delta d = (T_c \cdot c)/2 = 1.5 \text{ m} \tag{1.9}$$

The minimum measurement period is equal to the time of flight.

Bandwidth Resolution

The system bandwidth is a factor in the resolution of the time of detection. Note that while the resolution is involved, the influence of the bandwidth is different from that of the clock rate dealt with in section 1.2.4 and therefore bandwidth is discussed separately here. The bandwidth referred to is the total bandwidth of the signal path between the generation of the pulse in the transmitter and its detection in the receiver. Therefore, it includes transmitter and receiver intentional and unintentional filtering, as well as the frequency response of transmitter and receiver antennas and that of the propagation path, which is not a constant function of frequency.

In effect, the pulse rise time depended on the bandwidth, according to the relationship (1.10)

$$B_{bb} = k \cdot \frac{1}{2 \cdot T_r} \tag{1.10}$$

where B_{bb} is the total noise bandwidth referred to as baseband signal (one-half of the bandwidth in the RF pass band) and T_r is the rise time. k depends on the particular transfer function that determines B_{bb} and on how T_r is defined. As a useful approximation we assume $k = 1$

$$B_{bb} = \frac{1}{2 \cdot T_r} \text{ hence, } B_{bp} = \frac{1}{T_r} \qquad (1.11)$$

where B_{bp} is the RF bandpass bandwidth, equal to twice of the baseband bandwidth. The rise time is important because it creates an uncertainty as to the instant of arrival in a receiver of a transmitter pulse.

An important consequence of the bandwidth is its effect on multipath resolution. Radio signals arrive at a receiver over multiple paths because they are reflected from objects situated between the transmitter and the receiver. The paths of the reflected signals are longer than that of the direct, line of sight path, to a degree that depends on the distance of the reflecting object from the direct path.

Accurate distance measurement depends on identifying the earliest arriving pulse, since its time of arrival is needed to find the true distance between transmitter and receiver. When bandwidth is relatively low, the rise time is long and the extended leading edge of the line of sight signal may be interfered with or smeared by pulsed arriving along the multipath; thereby, making it difficult to distinguish.

The bandwidth needed in a multipath environment depends on required accuracy, on the differences in path lengths of reflected echoes, and on the strength of the echoes relative to the line of sight signal. Assume a one-way distance accuracy of 3 m is specified. A two-way time-of-flight resolution of $2 \times (3 \text{ m}/3 \times 10^8 \text{ m/s}) = 20$ ns must be achieved. A rule of thumb bandwidth is $B_{bp} = 1/20$ ns $= 50$ MHz. Bandwidth can be traded for measurement time in order to obtain a given accuracy with lower bandwidth than indicated by (1.11), when the interference is random noise.

1.3 Common Components of Indoor Positioning Systems

A basic function of wireless positioning system block diagram is suggested in [6]. It consists of 2 parts, which are sensing devices, a positioning algorithm, and display system. Figure 1.6 from [6][9] illustrates their components and their relationships. First, the sensing devices detect incoming signals from known or unknown sources such as radio frequency (RF), infrared (IR), visible light (VL) or ultrasound. The sensing techniques can be any method mentioned in both section 1.2.1 and section 1.2.2. Then, the positioning algorithm processes the measured information using approaches such as signal processing [5], deterministic approach [14], or probabilistic approach [15]. Finally, the display system interprets location information into a suitable format for the end user.

Location Merics
TOA, AOA, RSS, etc

Estimated Location
Coordinate (x, y, z)

Sensor 1

Received
Signal

Positioning
or
Location
Estimation
Algorithm

Display
System
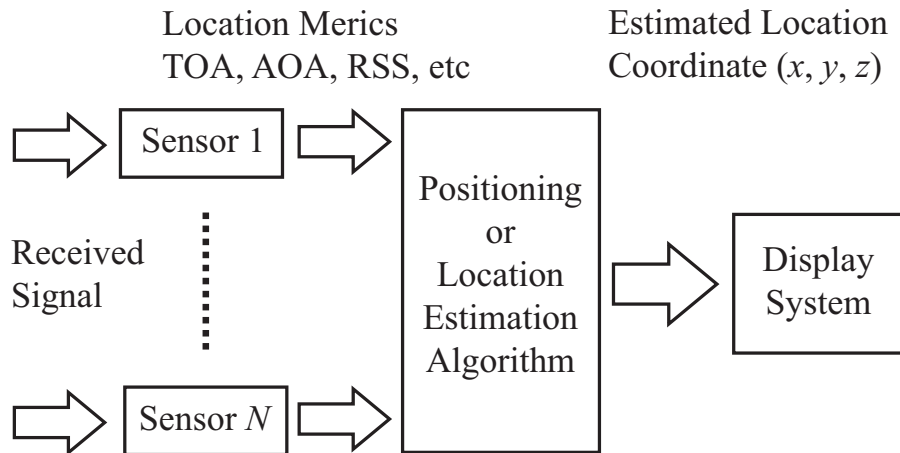
Sensor N

Figure 1.6: A general wireless positioning system functional block diagram

1.3.1 Sensing Technologies

In this dissertation we use visible light and multiband radio wave sensors in our proposed platform. Based on the sensing technologies deployed, we must investigate the characteristics and limitations on both types of the deployed signal. The propagation delay, reflection, transmission, diffraction, and scattering are general characteristic of all signal types. The effective range, available bandwidth, regulatory constraints, interference, power constraints, safety, and cost are technology limitations [9]. Note that other technologies such as infrared, ultrasound, laser ranging, scene analysis, and inertial based systems are also possible for indoor positioning system, but are beyond the scope of this study.

Visible Light Sensor

The visible light signal has the same properties as infrared. It cannot pass through walls or obstructions; therefore, it has a rather limited range in the room size. However, the propagation speed is high, approximately 3×10^8 m/s; therefore general method for short range positioning such as TOA cannot be utilized. Indoor lighting interferes and external sun light can causes problems on accuracy of sensor. The photodiode is used as visible light sensor; limitation of photodiode is owing to its field-of-view (FOV).

Multiband Radio Wave Sensor

The motivation of using multiband radio wave sensor is based on the emerging of cognitive radio technology. Cognitive radio is very well known for two of its unique property, dynamic spectrum allocation and multi-frequency band capable terminal. The radio frequency (RF) signal can penetrate most indoor building material; therefore, it is affected by reflection, transmission, diffraction and scatter. So as the visible light, RF propagation speed is also

approximately 3×10^8 m/s. With the multiband capable of cognitive radio numerous frequencies unlimited radio sources can be accessed such as WLAN 2.4 GHz, 5.2 GHz and digital terrestrial broadcast television.

1.3.2   Related Indoor Positioning Systems

Excellent comprehensive surveys of positioning systems can be found in [7] and with a special focus on indoor positioning systems in [9]. Therefore, this section will not delve into greater details of each of the forerunners of indoor positioning systems. A subset of these systems is reviewed as examples. The major characteristics of these systems are summarized.

Active Badge

The Active Badge location system [16] is one of the first generation of indoor positioning systems. This system uses a central server to determine user's location, sensors are used to pick up either periodically transmitted or on demand signals from infrared badges attached to the mobile user. Each infrared badge has its unique identifier. The achievable accuracy is very low as in room-size, for the reason that location determination is based on the proximity of badge and the sensors. The main limitations of this system are its range and interference from sunlight and fluorescent lights on infrared signal [7].

Active Bat

The second location system called Active Bat [17] is evolved from Active Badge by utilizing both radio and ultrasound signals instead of infrared signal. The system consists of a set of ceiling-mounted sensors that detect the on demanded ultrasound signal from the Active Bat tag that respond to an RF request packet from the centralized controller. Active Bat is also a centralized computation system that determines distance based on time-of-flight (TOF) of the ultrasound signal. The ceiling mounted sensors calculated the distance measurement between the time they transmit RF request packet and the time they receive ultrasound pulse from the mobile "Bat". This achievable accuracy is in the range of 9 cm for 95 % of locations.

SpotON

The SpotON is an ad hoc based location system [18], which uses distance measurement based on received signal strength instead of TOF. The system inventers combine the ideas of ad hoc networking with object localization. All of the targeting objects are attached with RF tags. Ad hoc lateration is performed using the estimated inter-tag distance instead of the distance from known sensors or base stations. Therefore, the system could provide both relative and absolute referencing. A dynamic cluster of tags enables any participating node

to exploit correlation of multiple measurements and improves the location accuracy as the tags' cluster becomes denser [18].

Cricket

Cricket location-support system is a location-based system designed with four objectives: privacy, decentralization, low cost, and room-sized granularity [19]. Unlike the preceding systems, Cricket is an independent of data network technology, which do not contain centralized server. Thus, the mobile device calculates its own location using both ultrasound and RF technologies. The main equipment is a beacon that transmits an RF pulse with a unique ID for that particular room. The RF signal is used for synchronization, and to identify the period of the ultrasound signal which is used in order to calculate the range with TDOA techniques. This mobile-based approach ensures its privacy. Nevertheless, RF beacon interference between two adjacent rooms can cause accuracy degradation.

These pioneer works in this area have some disadvantages such as the limitation of the infrared or ultrasound sensing signals that cannot penetrate the walls and doors which are common inside most buildings. The cost of sensor infrastructure installation and badges or tags for most of these systems becomes significant for a building with a lot of small rooms or offices. Notice that the angular or direction-based measurement was not used in any of these systems due to the dense multipath effect inside buildings. However, these positioning systems have only demonstrated their success empirically, and they all lack theoretical explanation of their system and performance.

1.4   Signal Characteristics

In this section, we discuss the fundamental factors that make differences between VLC and RF channel, which are wavelength property, reflection, diffraction, and transmission. In order to compare its behavior with RF signals, we view visible light as electromagnetic wave that has frequency in the range of THz. The first factor is the property of wavelength, since the electromagnetic wave with wavelength of λ cannot penetrate through the gap that has distance equal to or smaller than the $\lambda/2$. Thus, specular reflection points in each frequency band can be varied in different environments, of which alter the propagation paths in each frequency band. The more obstacles in environment are, the more diverse propagation paths in each frequency band becomes. The varied specular reflection points in each frequency band are considered to be the major impact to all of the following factors [20].

1.4.1   Reflection

The second factor that causes diversity is reflection. The normal handling of specular reflection is simplified by physical optics. Reflection is the function of frequency, polarization and
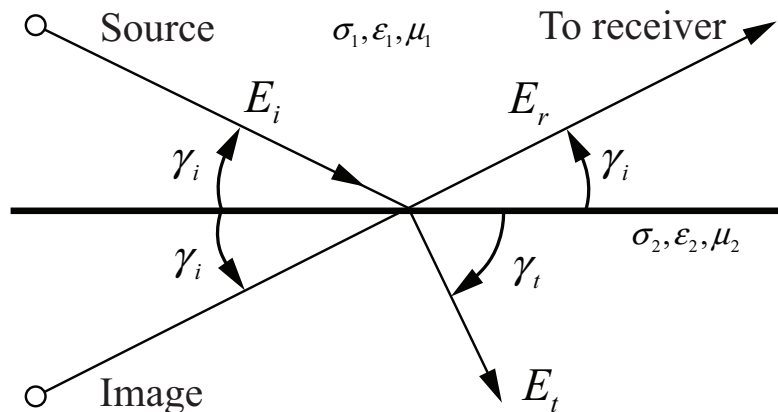
Figure 1.7: Specular reflection with source image

incident angle. In our experimental case, by utilizing dual-band access points as transmitters, reflection coefficients are mainly impacted by only two factors; frequency of the transmitted wave and incident angles of each frequency band alternated from the wavelength property. The reflection coefficients of parallel and perpendicular polarizations are shown in (1.12) and (1.13).

$$R_\parallel = \frac{\eta_2 \sin \gamma_t - \eta_1 \sin \gamma_i}{\eta_2 \sin \gamma_t + \eta_1 \sin \gamma_i} \qquad (1.12)$$

$$R_\perp = \frac{\eta_2 \sin \gamma_i - \eta_1 \sin \gamma_t}{\eta_2 \sin \gamma_i + \eta_1 \sin \gamma_t} \qquad (1.13)$$

where y_i is the angle of incidence relative to a tangent plane at the point of reflection and $\eta_{1,2}$ is the complex permittivity given by (1.14).

$$\eta_{0,1} = \sqrt{\frac{j\omega\mu_{1,2}}{\sigma_{1,2} + j\omega\varepsilon_{1,2}}} \qquad (1.14)$$

where σ, ε, and μ are the conductivity, permittivity, and permeability of the air and the reflecting material and ω is the frequency of the incident radiation in radians.

1.4.2 Diffraction

The third factor, diffraction, is also the consequences of discrepancy of specular reflection points in different frequency band caused by wavelength property and reflection. Diffraction is the function of frequency and incidental angle. It occurs when there is a partial blocking of a portion of the wave front by an object. Luebbers model [21] is regarded as one of the most accurate model that included reflection coefficient, which is also the function of frequency,
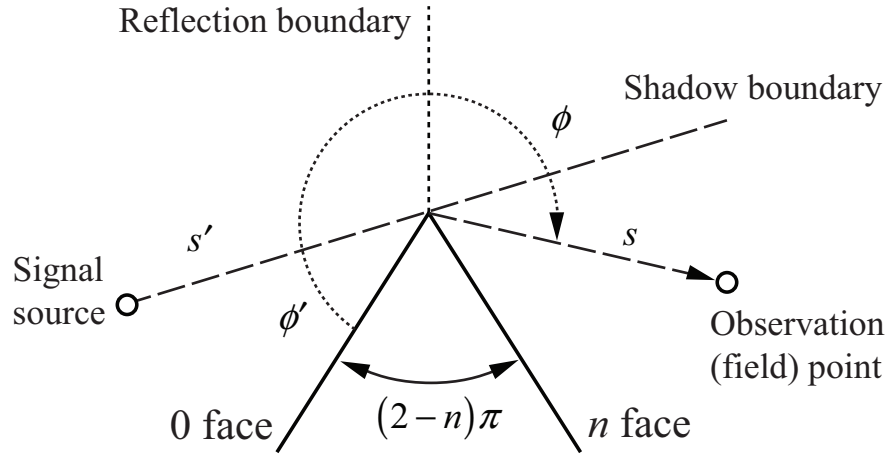
Figure 1.8: 2D of view wedge diffraction geometry

into the uniform theory of diffraction (UTD) as shown in (1.15).

$$
D_{\parallel}^{\perp} = \frac{-e^{j(\pi/4)}}{2n\sqrt{2\pi k}}
\begin{bmatrix}
\cot\left(\dfrac{\pi + (\phi - \phi')}{2n}\right) F\left(kLa^+\left(\phi - \phi'\right)\right) \\[2mm]
+ \cot\left(\dfrac{\pi - (\phi - \phi')}{2n}\right) F\left(kLa^-\left(\phi - \phi'\right)\right) \\[2mm]
+ R_{\parallel,0}^{\perp} \cot\left(\dfrac{\pi - (\phi + \phi')}{2n}\right) F\left(kLa^-\left(\phi + \phi'\right)\right) \\[2mm]
+ R_{\parallel,n}^{\perp} \cot\left(\dfrac{\pi + (\phi + \phi')}{2n}\right) F\left(kLa^+\left(\phi + \phi'\right)\right)
\end{bmatrix}
\tag{1.15}
$$

where $\parallel$ and $\perp$ denote diffraction coefficient of parallel and perpendicular incident wave, respectively. Symbols ϕ' and ϕ are the angles of incidence and diffraction, and $n\pi$ is exterior wedge angle. The phase constant, k, is directly proportional to wavelength as $2\pi/\lambda$. The Fresnel integral to correct for the singularities at the shadow boundaries is given by

$$
F\left(X\right) = 2j\sqrt{X}e^{jX}\int_{\sqrt{X}}^{\infty} e^{-j\tau^2}\,d\tau
\tag{1.16}
$$

where X represents the various possible arguments of $F(\cdot)$ in (1.15). The distance term L is

$$
L = \frac{ss'}{s + s'}
\tag{1.17}
$$

where s is the distance from diffracting edge to the field point, which can be varied in each frequency band due to the wavelength property, and s' is the distance from the edge to the source. The parameter a in (1.15) is given by

$$
a^{\pm}\left(\phi - \phi'\right) = 2\cos^2\left(\frac{2n\pi N^{\pm} - (\phi \pm \phi')}{2}\right)
\tag{1.18}
$$
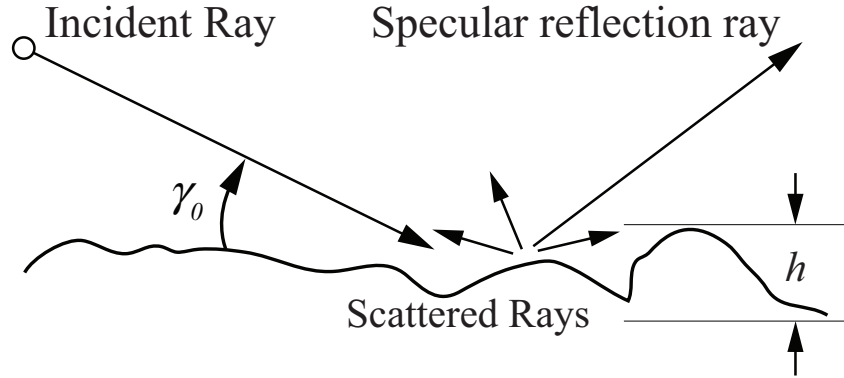
Figure 1.9: Reflection and scattering from a rough surface.

In (1.18), the parameters $N^\pm$ are integers, which most closely satisfy the equations

$$2\pi n N^+ - (\phi \pm \phi') = \pi \qquad (1.19)$$
$$2\pi n N^- - (\phi \pm \phi') = -\pi \qquad (1.20)$$

The terms R_0 and R_n refer to the reflection coefficients of the incidence wedge face (0 face) and the opposite wedge face (n face). They are computed for parallel and perpendicular polarizations by using (1.12) and (1.13), respectively.

1.4.3 Transmission

The fourth factor is transmission, which is occurred when an electromagnetic wave penetrates from one medium to another. Part of the energy is reflected and the rest is transmitted into the second medium. The transmitted wave changes amplitude and direction as it continues into the second medium. The transmission coefficients take a form similar to the reflection coefficients; transmission is also functions of frequency and incident angle, as follows

$$T_\parallel = \frac{2\eta_2 \sin \gamma_i}{\eta_2 \sin \gamma_t + \eta_1 \sin \gamma_i} \qquad (1.21)$$

$$T_\perp = \frac{2\eta_2 \sin \gamma_i}{\eta_2 \sin \gamma_i + \eta_1 \sin \gamma_t}. \qquad (1.22)$$

The RSS of EM wave that transmitted through human body, is greatly attenuated with 2.4 GHz frequency band [9][22]. Since water, which also has a resonance frequency at 2.4 GHz, is a significant part inside the human body.

1.4.4   Scattering

A smooth reflecting surface is an idealized surface that is only occasionally encountered in real propagation environments. Typically encountered surfaces have random variations as in the earth's surface or have systematic variations such as in the walls and roofs of artificial structures. Depending on the wavelength of the wireless signal, the height of these variations may or may not be significant in terms of how reflection amplitude is calculated. In extreme cases, the surface may appear to be a pure scattered. The degree of roughness, or the criterion on which roughness warrants considerations, is often given by [23] which is also known as the Rayleigh criterion:

$$h_R \geq \frac{\lambda}{8 \sin \gamma_0} \tag{1.23}$$

where h_R is the difference in the maximum and minimum surface variations as illustrated in Fig. 1.9. For a frequency of 2 GHz and an incident angle of 20 degrees, $h_R = 5.5$ cm. Terrain and the outside surfaces of buildings can easily exhibit surface variations greater than this.

1.4.5   Similarity and Differences

Geometrical optics (GO) is used to describe both light and electromagnetic propagation in terms of "rays". The "ray" in geometric optics is used to approximately model how wave will propagate. Together with UTD described in section 1.4.2 form a widely used as a radio wave propagation modeling known as 'ray-tracing'. The limitation of ray-tracing is that the physical dimension of the scattering objects must be large compared to the wavelength. The five propagation primitives, four of which were described in section 1.4, usually included in a ray-tracing model are free-space propagation, reflection, diffraction, diffuse wall scattering and wall transmission.

Although both VLC and RF signal are electromagnetic wave, their characteristics are relatively different owing to their operational frequency. Therefore, not all of propagation primitives in ray-tracing model can be applied to VLC. In VLC system only free-space propagation, 1 time reflection, and diffusion are included in the simulation model [24]. On the other hand, RF propagation use 7 times reflection scattering, 1 time diffraction, and 7 times transmission [20]. Details of both VLC and RF systems are fully discussed in chapter 2, 3 and 4.

1.5   Motivation of This Research

The main motivation behind this research is that GPS accuracy in indoor environment is highly degraded due to the effects of multi-path component and obstacles. Apart from the fact that GPS accuracy is highly degraded in indoor environment. There are two more motivations for this research. Firstly, general wireless technology has short lifetime such as mobile

Approximate timeline:
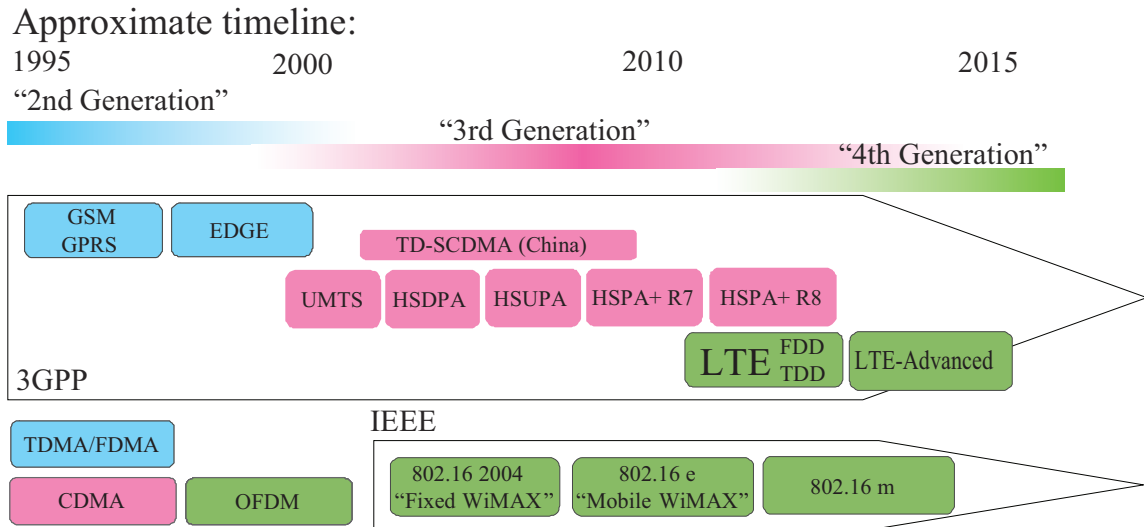
Figure 1.10: Approximate timeline of the mobile communications standards landscape.[25]

phone system that lifetime approximately 5-10 years in each generation [25], of which use different transmission technology; as shown in Fig. 1.10. Thus, high investment is required for upgrading infrastructures to the newer generation. Secondly, the entire conventional technologies such as Pseudolite [26], active badge [16], Active bat [17], and SpotON [18] require new infrastructure that cannot be used for other purpose. Thus, high investments on unnecessary infrastructures are required for wide area deployment. In this dissertation, we focus on developing a new indoor positioning architecture that has long lifecycle and can utilize the existing infrastructures in order to make it widely deployable with low cost.

1.6 Proposed Positioning System Architecture

The momentous goal of this research focuses on creating a new solution architecture for indoor positioning, which has lower complexity, irrelevant with available bandwidth, compatible with existing and emerging systems. In order to accomplish this goal, we had been studying on numerous potential solutions and came up with two candidate systems that fit the previously mentioned objectives. We believed that both VLC and multiband received signal strength (MRSS) fingerprinting can be a lifetime solution for indoor positioning system. In this dissertation, we define the word lifetime solution as a solution that after being implemented, it does not require any modification on the core equipment and can be used throughout our lifetime. We deploy machine learning algorithms in both subsystem to ensure the system involvement throughout its lifetime. In the proposed architecture, we carefully design both systems to be very flexible. Thus, they can operate solely on their own, or can be collaboratively operate, as shown in Fig. 1.11. Details of both subsystems are explained
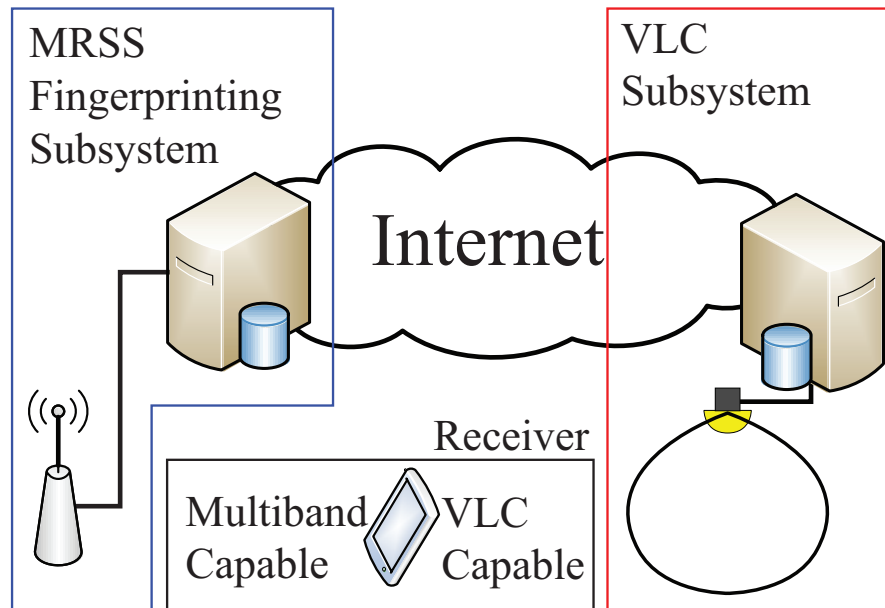
Figure 1.11: The proposed lifetime indoor positioning solution architect block diagram, each subsystem can either work separately or collaboratively.

in the following subsections.

1.6.1 Visible Light Communication Subsystem

The first subsystem, our proposed VLC based positioning focuses on the improvement of visible light communication identification (VLID) system that provides positioning information via LED light bulb, which is a part of VLC system. VLC is the communication technology that uses illumination from light bulb to transmit data. The visible light is everywhere around our daily life in the indoor environment, such as in office, supermarket, museum, etc. Undeniably, vision is one of the most important human sensory to perceive day-to-day information. Illumination of the visible light is also has a great impact on deliberating aesthetic and practical effect. For instance, illuminations in supermarket are designed to be vividly bright in order to make customer feel secure. On the other hand, illuminations in fine dining restaurant are designed to deliberate the elegance of the inhabiting space. Lighting architect plays important role on adding these secondary sensory function into illumination. Prof. Masao Nakagawa had taken visible light into the further step by adding the third functionality, communication, into visible light. VLC is finalized as Japanese communication standards JEITA-1221 [27] and JEITA-1222 [28], and currently being pushed forward as international standard under IEEE802.15 TG7. By combining VLC with power line communication (PLC) ubiquitous communication can be achieved without installing any extra infrastructure [29].
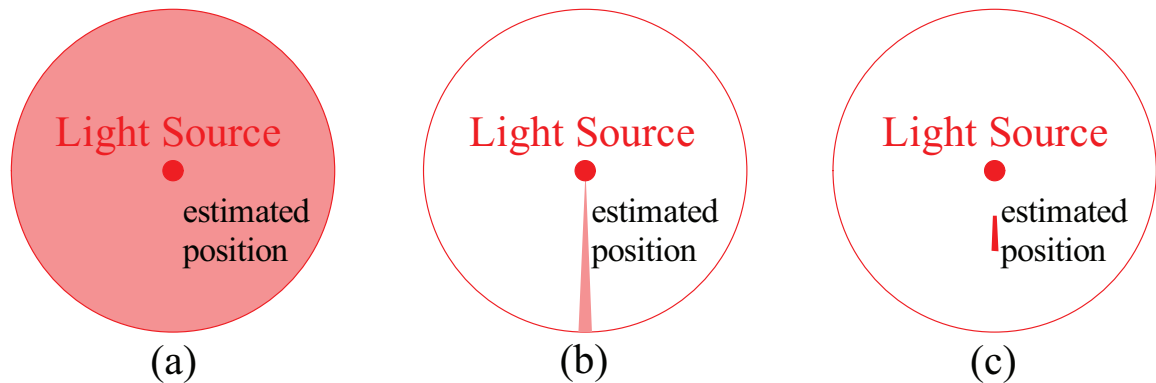
Figure 1.12: Estimated position by (a) only data from VLID, (b) data from VLID and 6-axis sensor (c) data from VLID, 6-axis sensor and switching estimated position technique.

VLC with positioning information broadcasted from the LED light source, visible light ID (VLID) [28], can offer many opportunistic applications; such as application in area of barcode reader for supply management system. In basic positioning systems, where only VLID is used, the direction and position from light source of estimated position cannot be identified. The achievable positioning accuracy only by VLID is very low as in room level as shown in Fig. 1.12(a). In our approach, neither additional infrastructure nor modification is required on the transmitter side, as shown in Fig. 1.13. On the receiver side, 6-axis sensor is embedded to provide 3-axis of Azimuth and 3-axis of tilt angulations information to perform positioning estimation. The higher estimated position accuracy can be achieved contributed to angulations information from 6-axis sensor. Hereafter, we denote this generic system as a general orientation sensor's information (GOSI), the estimated achievable accuracy is shown in Fig. 1.12(b). Furthermore, we proposed a positioning scheme called switching estimated receiver position (SwERP) scheme that can further enhance the positioning accuracy over GOSI system, as shown in Fig. 1.12(c). Details of the proposed architecture and its subsystem are elaborate in the following paragraphs.

Chapter 2 presents the characteristics investigation of the proposed VLC architecture. Extensive experiments was performed and compared to the previously proposed VLC models [28]. By incorporating 6-axis sensor into VLID receiver, we discovered two unique characteristics, based on our proposed architecture, which are field of view (FOV) and sensitivity limits. FOV limit is contributed to receiver limitation and sensitivity limit are the effects of channel characteristic of VLC. Both FOV and sensitivity limit are the fundamental attributes to enable the proposed SwERP scheme. SwERP scheme is a low complexity that took advantage of the occurrences of FOV and Sensitivity Limit. We use root mean square error of distance error to evaluate the performance of the proposed architecture. The results show that SwERP can provide higher accuracy and tolerant from receiver's height variation than GOSI scheme. The uniqueness of the proposed VLC architecture is only one transmit-

Power Line Communication : PLC   Visible Light Communication : VLC
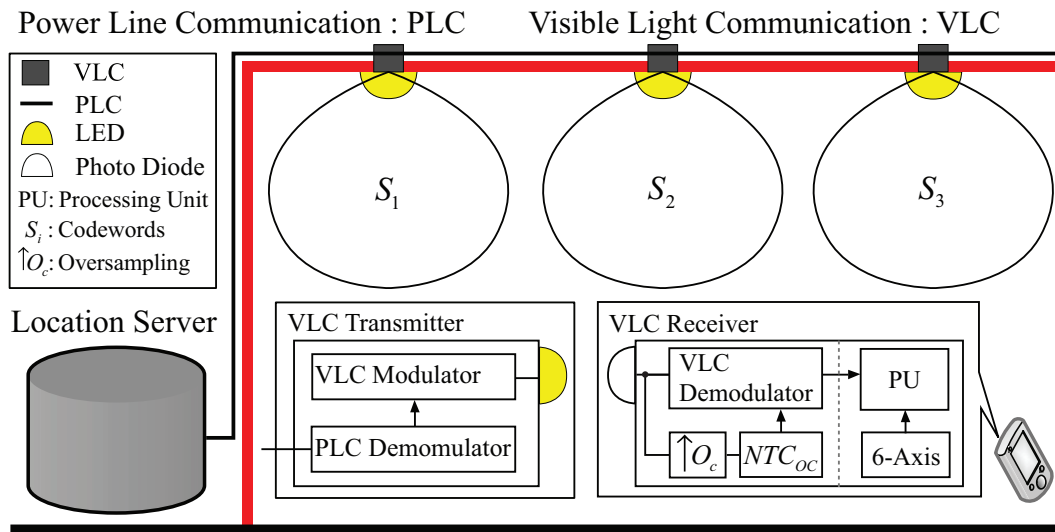
Figure 1.13: Visible light communication based positioning system

ter is required for positioning estimation. Thus, higher accessibility can be achieved from the proposed scheme.

On the contrary, SwERP scheme requires the presences of sensitivity limit. Therefore, in chapter 3 we introduce optical orthogonal code (OOC) into conventional VLID system for positioning purpose. Apart from gaining higher capacity from OOC codes [30], we propose a nearest transmitter classification method based on optical orthogonal code (NTC_{OC}). The proposed NTC_{OC} uses TDOA access method to enable SwERP scheme. Thus, even without the presences of Sensitivity Limit, SwERP can still be utilized. The breakthrough came from the courtesy of oversampling deployment that yields time resolution of OOC autocorrelation function's resolution. Furthermore, in section 3.2 we used system characteristics studied from chapter 2 to create a physical layer evaluation model. A machine learning algorithm, specifically support vector machine (SVM), is used to solve the geometrical problem of FOV limit's projection. All of the parameters that curtail in modeling process are also discussed in section 3.2.

Apart from defining VLC based positioning architecture we propose three novel subsystems that helped us realized the positioning accuracy enhancement, which are switching estimated receiver positioning (SwERP), optical orthogonal code (OOC) based nearest transmitter classifier method (NTC_{OC}) and physical layer simulation model for VLC based positioning system. To sum up, the proposed VLC based positioning subsystem provides an opportunistic indoor positioning solution from utilize existing illumination infrastructures. The achievable accuracy from this subsystem is less than 1 meter. However, the VLC based positioning has an unavoidable communication limitation, owing to its wavelength property that has low transmission property as explained in section 1.4.3. To ensure the success of
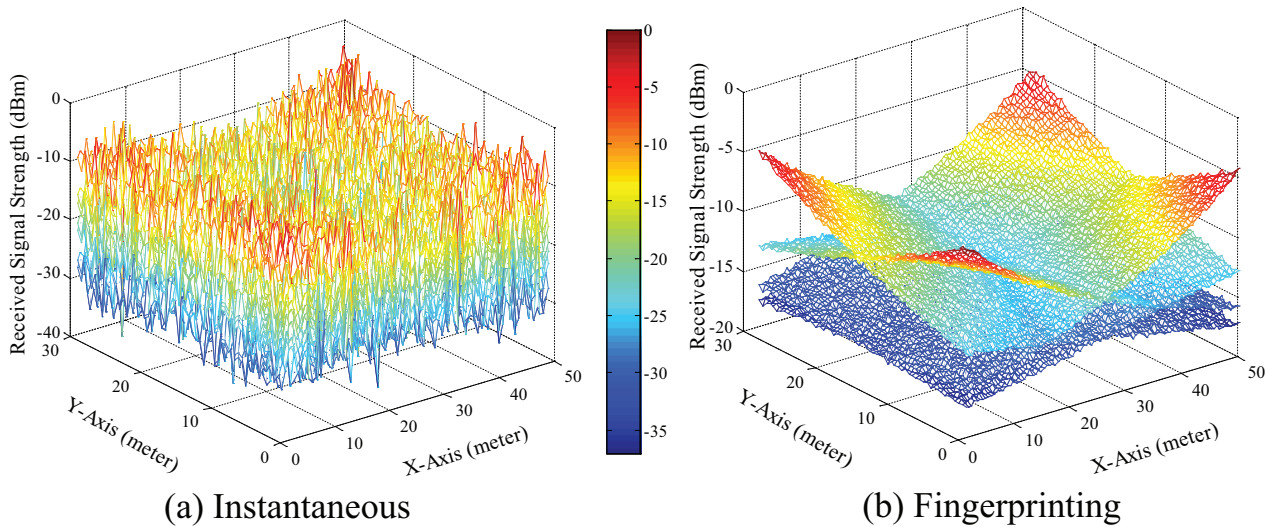
Figure 1.14: Simulation of (a) instantaneous RSS (b) RSS fingerprinting of 2.4 GHz band in LOS environment (30 × 50 meter), based on log-normal distribution with 4 transmitters located outside at each corner of the simulation area.

accessibility, we introduced MRSS fingerprinting subsystem as a complimentary into the proposed architecture. The extensive discussion on VLC based positioning subsystem and its contributions can be found in chapter 2 and 3.

1.6.2 MRSS Fingerprinting Subsystem

In the second subsystem, we develop the system architect based on RSS fingerprinting system by deploying frequency diversity at receiver in order to capture multi-band received signal strength (MRSS). RSS fingerprinting system utilizes the radio frequency (RF) of the existing WLANs infrastructure endorsing many location based services (LBSs). The fingerprinting technique refers to a technique that exploits the relationship between any premeasured value at a specific location. There are many types of fingerprinting technique, all of which named after its premeasured value. In the RADAR case [14], the RF received signal strength is the stimulus, also known as RSS fingerprinting technique. The advantage of fingerprinting technique is no specialized hardware other than the ordinary wireless network interfaces equipment required. RSS is the most suitable access method over AOA and TOA owing to its robustness under indoor environment. The current limitation on achievable accuracy from RSS fingerprinting method is presented in [9][22][31][32]. Thus, in this dissertation we focus on improving the conventional RSS fingerprinting system. We introduce MRSS fingerprinting, from the courtesy of cognitive radio multiband capability, as a part of our solution architecture. The proposed architecture can incorporate RF signal not limit to only WLAN but also any existing wireless infrastructure. Like conventional RSS fingerprinting

system, MRSS deployment of fingerprinting based positioning systems can be divided into two phases.

First, in the training or off-line phase, the MRSS fingerprinting created by performing a site survey for collecting RSS from multiple frequency band. To prove that frequency diversity itself can improve the fingerprinting performance. We use dualband access points (APs) which can simultaneously transmit signal in both frequency bands as our multiband transmitter. The objective for deploying frequency diversity on RSS fingerprinting is to increase its resolution. Thus, we record the premeasured RSS value from each frequency band separately. The entire studied area is measured by a rectangular grid points. The distance between two closest grid points, grid spacing, defines the minimum achievable accuracy. However, some part of the grid points can be omitted due to inaccessibility of measurement. The differences between instantaneous RSS measurement and RSS fingerprinting is shown in Fig. 1.14. Due to the RSS fingerprinting map liked characteristic, it is also called as radio map [22]. The vectors of RSS values from each frequency band are stored respect to the fingerprint location of than point.

Second, in positioning or on-line phase, MS measures multiband RSS signals vector from several APs and existing wireless infrastructures compare with the premeasured database. The measured RSS vector is compared to premeasured MRSS fingerprinting database in the training phase. Position estimation can be done either on MS station or processed at central server depended on the complexity of utilized algorithm. The most common algorithm used for positioning estimation is the computation of Euclidean distance between the samples measured in positioning phase and MRSS fingerprinting database. The fingerprint location that provides lowest Euclidean distance is selected as the estimated position. There are many advances algorithms such as neural network [31] and Bayesian modeling [33] that can be used for positioning estimation. However, we focus only on using simple algorithm, such as nearest neighbor (NN) and k-th nearest neighbor (KNN) method, to prove that frequency diversity can improve the performance of RSS fingerprinting system. Details of this proposed MRSS fingerprinting subsystem is elucidated in chapter 4.

Utilizing MRSS gives us numerous advantages as follows. Firstly, no synchronization is required between transmitter and receiver. Secondly, modulation schemes and system bandwidth do not have impact on RSS [11]. Moreover, radio wave provides higher accessibility than VLC based positioning system; remote positioning can be achieved even without LOS between transmitter and receiver. Last but not the least, transmitted signal from existing infrastructures (e.g. WLAN, digital broadcasting system, cellular network) and other emerging wireless technology infrastructures will provide numerous frequency bands. In cooperation with multi-band capable receiver; such as cognitive radio [2], receiver can simultaneously access to the numerous frequency bands. Hence, no additional infrastructures are needed to perform localization.

There are two major advantages of MRSS fingerprinting based indoor positioning system. Firstly, the fingerprint at each location can be created by RSS from numerous types of existing wireless network infrastructures, as a result of deploying frequency diversity on
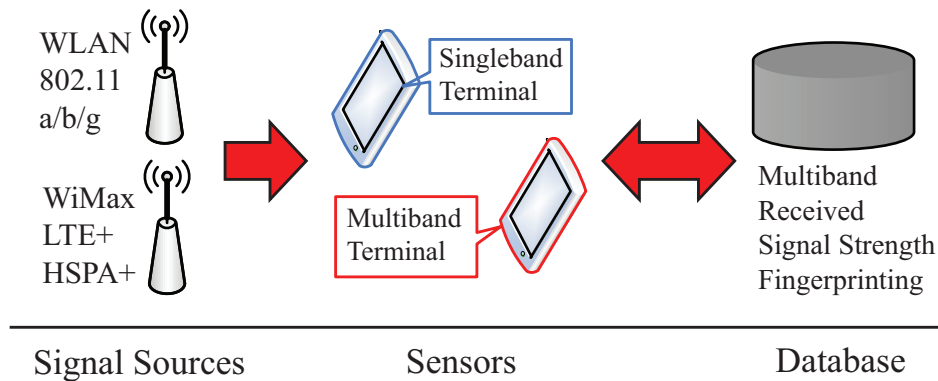
Figure 1.15: Multiband received signal strength based positioning system

RSS fingerprinting, without prior knowledge of those transmitter locations. Secondly, Fingerprinting method is a database approach that can initiate highly compatible platform as shown in Fig. 1.15. MRSS fingerprints are constructed from both singleband and multiband radio terminal. Therefore, any type of terminal that has premeasured RSS recorded in MRSS fingerprinting server can utilize the database for localization.

To sum up, MRSS fingerprinting provides an opportunistic indoor positioning solution from the existing wireless infrastructures and any emerging wireless infrastructure. MRSS fingerprinting utilizes RF signals for localization. Thus, this system has lower limitation on accessibility, owing to wave propagation, than the previously described VLC based positioning system. In contrast, MRSS fingerprinting requires abundant manpower to create database during training phase. Intuitively, using estimated position from VLC based positioning subsystem to calibrate MRSS fingerprint in radio wave pre-measurement process can greatly reduce manpower during the training phase, as shown in Fig. 1.11. However, performance of the mention system is not evaluated since it is out of this dissertation scope. The extensive details and discussion on MRSS fingerprinting subsystem are provided in chapter 4.

1.6.3 Positioning Engine (Machine Learning)

In order to ensure the objective of the proposed solution architecture, we include machine learning algorithms into each subsystem of the proposed architecture, to enable the system adaptation during its lifetime. To be slightly more specific, the architecture of a typical machine learning "agent" described in [34] is shown as Fig. 1.16. This agent perceives and models its environment and computes for appropriate actions. The updated made to any of the components in the figure counted as learning process. Different learning algorithms might be employed depending on which system it's being implemented on. Prof. Nils J. Nilsson defined definition of machine learning in [34] as

Machine learning usually refers to the changes in systems that perform tasks
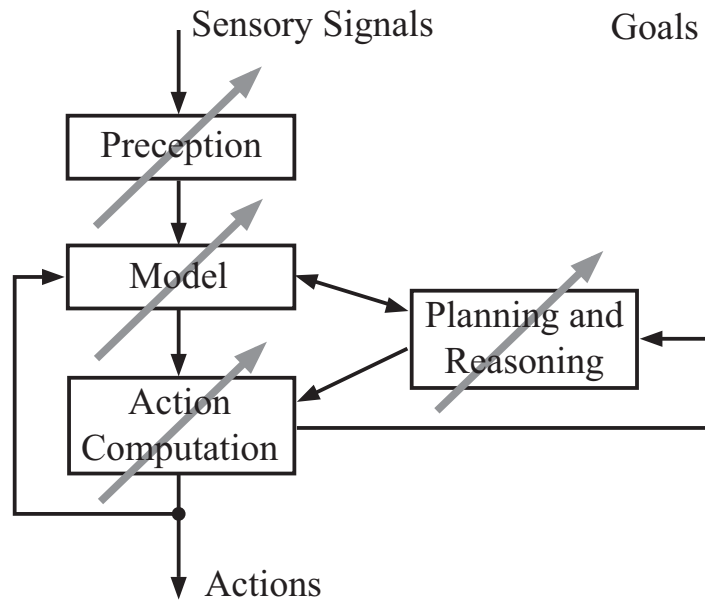
Figure 1.16: A machine learning diagram

associated with *artificial intelligence* (AI). Such tasks involve recognition, diagnosis, planning, robot control, prediction, etc. The "changes" might be either enhancements to already performing systems or *ab initio* synthesis of new systems.

The reasons that we need machine learning algorithms because some algorithms used in practical system cannot be accurately designed. By letting machines adjust their internal structure to compute the output is more appropriate for large number of sample inputs such that in our system. Moreover, there is a possibility that hidden among large piles of data can have important relationships and correlation. Machine learning algorithms were introduced to extract these relationships [34]. Lastly, the environments can change over time. A platform that could adapt to a changing environment is vital for lifetime solution and can definitely reduce the need for constant redesign.

1.7   Advantage and Disadvantage of Each Subsystem

As mentioned in section 1.6, the study approach focuses on VLC that uses next generation light bulb that provides illumination as transmitter and MRSS fingerprinting created from existing wireless infrastructure. The mention technologies are based on infrastructures that necessary for our life (illumination and radio wave communication). Each technology has its advantage and disadvantage and is complimenting each other, details are being discussed as follows:

Table 1.2: Advantages and disadvantages of each subsystem

Subsystem	Advantage	Disadvantage
Visible Light	• VLC uses illumination for communication. • Light bulbs are everywhere in indoor environment. • High accuracy can achieved without pre-measurement.	• Receiver's field-of-view (FOV) limits communication connectivity. • VLC cannot be operated under shadowing environment.
MRSS Fingerprinting	• MRSS fingerprinting uses radio wave transmitted from existing wireless infrastructure. • The MRSS fingerprinting does not have communication problem in non-line-of-sight (NLOS) and high shadowing environment.	• Pre-measurement of RSS signal is required to create fingerprinting. • Human presences have impact on positioning accuracy.

For the reasons mentioned in table 1.2, we require both technologies to in order to provide all time accessibility. We design our proposed architecture to have two subsystems that can operate parallely.

1.8 Approaches and Contributions

This dissertation is a systematic study of the proposed indoor positioning lifetime solution architecture based on eco-friendly approach. The overview of this dissertation is shown as in Fig. 1.17, where existing wireless infrastructure are used for localization purpose. Beginning with an investigation of the system characteristic of VLC approaches, a model of the VLC based positioning is derived. Next, a MRSS fingerprint model of positioning system is proposed to compromise the limitation of VLC based proposed system. Both of the outline systems consist of three main components: the model of localization subsystem, path loss propagation model, and the positioning algorithm. The result models are considered for a system design framework for the indoor positioning system. Finally, system design and implementation guidelines are suggested based on the performance study of the proposed indoor positioning architecture.

There are two main subsystems for the proposed architecture, which are VLC based positioning subsystem and MRSS fingerprinting subsystem. Machine learning algorithms are the key factor to accomplish lifetime solution, for the reasons mentioned in section 1.6.3. We limit scope of this research into five main assumptions as follows. First, this study is limited to the investigation of stationary mobile, no mobility tracking is considered. Second, the placement of wireless infrastructure is not considered. The indoor positioning is assumed to

Power Line Communication Local Area Network

Visible Light Identification #1

Digital Telestrial Broadcasting

Visible Light Identification #2

Femto Cell (WLAN, LTE+)

Mobile Station (MS)
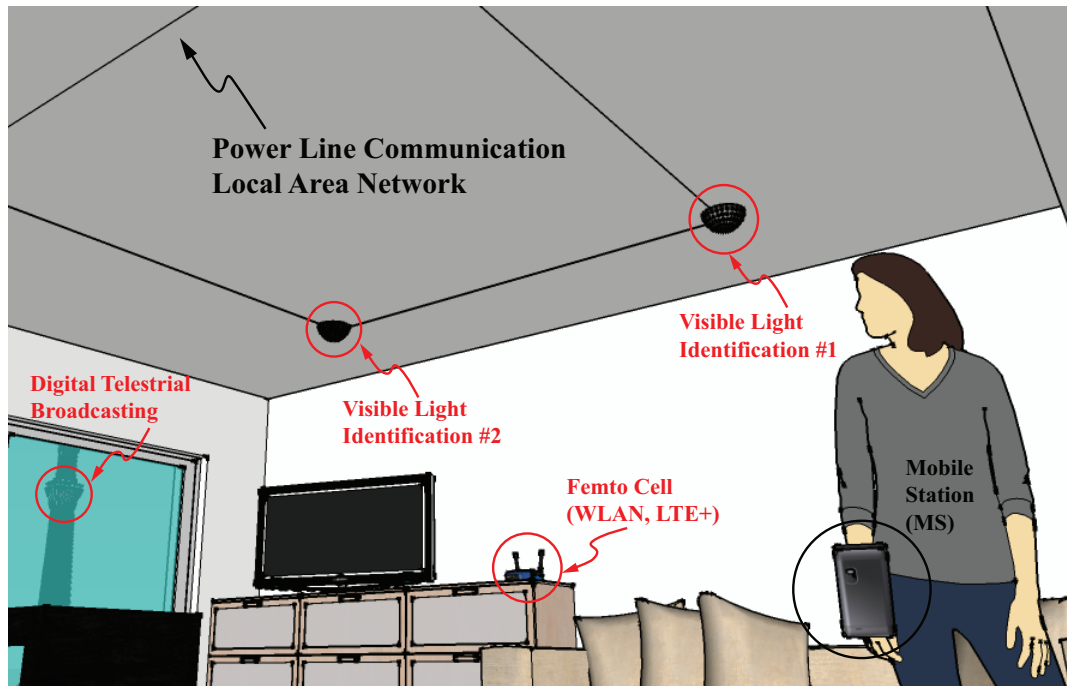
Figure 1.17: Illustration of the proposed architecture.

be overlaid on top of existing infrastructure. Therefore, the performance of the positioning system depends on the placement of wireless infrastructure. Third, this study does not consider the search of an optimal positioning algorithm, but assumes generic algorithms as baseline to prove that the proposed architecture can operate properly. Finally, although it is intuitive that both of the proposed subsystem can be combined. We only provide the analysis of the individual subsystems. The performance of the combined subsystems is beyond the scope of this dissertation.

We start with channel analysis of VLC based positioning system from analytical and experimental result. This study performs an extensive data analysis of the VLC based positioning system in order to understand its underlying features. We proposed an algorithm based on system characteristic to enhance system performance. Furthermore, we proposed two subsystems that enhance the VLC system performance. This dissertation provides theoretical understanding and concrete recommendations on how to design the indoor positioning system. The VLC based positioning system has unavoidable communication limitation, owing to its wavelength property that has low transmission property. To ensure the success of accessibility, we introduced MRSS fingerprinting system as a complimentary system. So as VLC based positioning system, we made analysis and experiment to prove our claim. The work on this subsystem is mainly focus on proving that frequency diversity can greatly improve the accuracy of conventional fingerprinting subsystem. The main goal is to prove

that both of the proposed subsystems can solely work on itself. The following is the list of contributions:

- Study and characterization of the proposed VLC and MRSS fingerprinting through an extensive measurement and simulation.

- Proposed minimum requirement infrastructures and algorithms for VLC and MRSS fingerprinting subsystem.

- Identified system parameters used for designing indoor positioning system such as the grid spacing, number of access points, oversampling ratio and switching angle. We quantify the impact of these system parameters on the performance of proposed architecture.

- Recommended design guidelines to facilitate the deployment of indoor positioning system based on the proposed architecture.

We summarize the problems of conventional systems in each chapter, and categorize them by difficulty, breakthrough solution and discuss the effect of the proposed scheme. Details of the study are provided in Table 1.3.

1.9   Organization

Chapter 2 reports on our detailed investigation of the first subsystem VLC based positioning characteristics and infrastructure. We define FOV and sensitivity limits, of which are key factor to positioning accuracy improvement. Based on both limits, we propose a switching estimated receiver position (SwERP) scheme that can greatly enhance positioning accuracy. In chapter 3, we propose two enhancement modules to help enabling the SwERP scheme. Firstly, an optical orthogonal code (OOC) based nearest transmitter classification (NTC) method is proposed to yield the necessity of sensitivity limit presence. Secondly, based on FOV limit we propose a physical simulation model to help evaluating the effectiveness of the proposed SwERP scheme. For the reason that VLC has unsolvable shadowing problem. Thus in chapter 4, we propose MRSS fingerprinting subsystem as a parallel system to ensure the pervasiveness of accessibility. The fundamental infrastructure and its characteristics are discussed in this chapter. Finally, the conclusion and discussion of the future work is presented in Chapter 5. The overall structure of this dissertation is shown in Fig. 1.18.

Table 1.3: Problems of existing schemes and the contribution of the proposed schemes

Chapter 2	Topic	Visible light communication based positioning subsystem
	Problems of existing research [28]	In conventional visible light identification (VLID) system, the direction and position from light source of estimated position cannot be identified. The achievable positioning accuracy only by VLID is very low as in room level.
	Proposed solution	We integrated 6-axis sensor into the receiver to provide Azimuth and Tilt angulations information. FOV and sensitivity limits are defined based on the integrated system. Thus, switching estimated receiver position (SwERP) scheme is proposed based on the presences of sensitivity limit.
	Effect of proposed scheme	SwERP is a low computation scheme that could provide over 85% of accuracy improvement with higher tolerance to terminal height variation.
Chapter 3: (Section 3.1)	Topic	Nearest Transmitter Classification (NTC) Method
	Problems of existing research [52]	SwERP scheme requires the sensitivity limit controlling module, which is unnecessary for communication and complicate.
	Proposed solution	NTC based on optical orthogonal code (NTC_{OC}) is utilized as the complimentary module to presences of sensitivity limit.
	Effect of proposed scheme	Optical orthogonal code can be used for communication and NTC_{OC} provides higher correct classification rate.
(Section 3.2)	Topic	Physical Layer Simulation Model
	Problems of existing research [52]	Integrating 6-axis into VLC based positioning system changes conventional VLC system characteristics. Thus, new simulation model must be developed for further study of the proposed VLC based positioning subsystem.
	Proposed solution	We use characteristic study from chapter 2 to construct simulation model. Support vector machine (SVMs) is used to classified the FOV limit, of which one of the most important parameter to enable SwERP scheme.
	Effect of proposed scheme	Apart from successfully constructing simulation model for VLC based positioning subsystem. We found out that from the proposed simulation model can reduce computation complexity up to 90%

Chapter 4	Topic	Multiband Received Signal Strength Fingerprinting Subsystem Architecture
	Problems of existing research [64]	Conventional RSS fingerprinting system has limitation on achievable accuracy, and can only be used with WLAN infrastructure.
	Proposed solution	We deploy frequency on RSS fingerprinting to enhance achievable accuracy. Moreover, with the proposed solution architecture every existing wireless infrastructure can be used as signal sources.
	Effect of proposed scheme	Higher achievable can be achieved in non line-of-sight (NLOS) environment, owing to the deployment of frequency diversity on RSS fingerprinting.

Chapter 1
Introduction:

(Chapter 1.1~1.4)   Background and technologies utilized in positioning system.

(Chapter 1.5)   Proposed solution architecture.

Research on VLC based positioning subsystem.

Research on MRSS fingerprinting subsystem.

Chapter 2
Solution Architect of VLC Subsystem

(Chapter 2.1~2.3)   VLC based positioning system characterization and modeling.

(Chapter 2.4)   Switching estmated receiver position (SwERP) scheme.

(Chapter 2.5)   Performance evaluation.

Chapter 3
Enhancements for VLC Subsystem

(Chapter 3.1)   Nearest transmitter classification method based on optical orthogonal code.

(Chapter 3.2)   Physical layer simulation model for VLC subsystem.

Chapter 4
MRSS Fingerprinting Subsystem

(Chapter 4.1~4.2)   MRSS fingerprinting system characterization and modeling.

(Chapter 4.3) k-th nearest neighbor classification on MRSS fingerprinting.

(Chapter 4.5)   Performance evaluation.

Chapter 5: Conclusion and Future Development of The Proposed Solution Architect

Figure 1.18: The overall structure of this dissertation.

Chapter 2

VLC Based Positioning Subsystem Architecture

In this chapter, we study the characteristic of the proposed VLC subsystem through extensive measurements and confirm with simulation results. As mentioned in 1.6.1, embedding 6-axis sensor into conventional VLID system greatly change system characteristics. In the study, we identify system parameters used for enhancing positioning accuracy. Based on the studied characteristics we proposed a switching estimated receiver position (SwERP) scheme that can greatly enhance positioning accuracy.

2.1   Proposed Infrastructure

In the first proposed system, we focus on developing low-complexity indoor positioning system that utilizes existing infrastructure based on VLC transmitted via power line communication (PLC) [28][29]. The VLC based positioning is eco-friendly because no carbon footprint (CF) is produced from construction, and VLC uses LED light bulb, which consumes less electricity and longer usage life cycle as transmitter. In addition, old style incandescent light bulb is banned from European Union since September 2009 and will be obsolete at the end of 2016 [35]−[37]. The United States of America also has announced its plan to phase out old style incandescent light bulb and finish by year 2014 [38]. By that time, we would be able to fully realize the pervasiveness of VLC system. In addition to the conventional VLC system, we embedded the 6-axis sensor, which provides 3-axis of Azimuth and 3-axis of Tilt angulations information, at a receiver to provide information. We propose a positioning scheme base on system characteristic to enhance positioning estimation accuracy.

Table 2.1: Standard of Visible Light ID System

Wavelength	380-780 mm
Data rate	4.8 kbps
Modulation method	SC-4PPM
SC Modulation frequency	28.8 kHz
Payload length	512 bit
Frame length	542 bit
Frame time	0.113 s
Payload	ID, General Data

SOF (Start of Frame)		Payload	EOF (End of Frame)
PRE (6-bit)	F-Type (8-bit)	DATA (512-bit)	CRC-16 (16-bit)

(1) TYPE A

SOF (Start of Frame)		Payload		EOF (End of Frame)
PRE (6-bit)	F-Type (8-bit)	ID (128-bit)	DATA (512-bit)	CRC-16 (16-bit)

(2) TYPE B

Figure 2.1: Visible Light ID Frame Construction.

2.1.1 Visible Light Communication (VLC)

Visible light communication (VLC) [24] is regarded as one of the most promising alternative to radio wave communication. VLC system can provide various opportunistic solutions to the deficiency of frequency band in radio wave communication, for the reason that visible light is not interfering with radio frequency band. Moreover, by integrating VLC into existing power line communication [29], true indoor ubiquitous environment can be achieved. VLC system is adopted as Japan Electronics and Information Technology Industries Association standard body number CP-1221. Currently, VLC is being considered as one of the candidates for IEEE 802.15 in task group 7 (IEEE 802.15.7). VLC standard promises both indoor and outdoor applications such as traffic control infrastructure, outdoor advertising, infrastructure-to-mobile communication, mobile-to-mobile communication, secure indoor LAN and position information (VLID) [28]. At present stage, VLC can transmit data up to 1 Gbps [39].

Table 2.2: Parameters of VLC Development Tool Kit

VLC data rate	4.8 kbps
Modulation method	28.8 kHz SC-4PPM
Semi-field of view (FOV: ψ_c)	$25^o, 17.5^o$, and 10°
Half-power angle ($\Phi_{1/2}$)	50°
Transmit optical power (P_T)	400000 nW
Rx sensitivity ($R_x S$)	16 nWrms
Refraction index (n)	1.460 (Plastic)
Concentrator gains ($g(\psi)$)	11.9346 ($\psi_c = 25^o$)

2.1.2 Visible Light Identification System (VLID)

Positioning information broadcasted from LED light source, visible light ID (VLID), can provide many opportunistic applications; such as application in area of barcode reader for supply management system. VLID was adopted as JEITA (Japan Electronics and Information Technology Industries Association) CP-1222 standard since June 2007. In this section, standard and modulation method of VLID system are described.

Standard of Visible Light ID System

Standard of VLID system is shown in Table 2.1. Wavelength used in VLID system is in the range of visible light. Frame construction detail is illustrated in Fig. 2.1. There are two types of frame construction type A and B. Both of frame constructions contain SOF (start of frame), payload and EOF (end of frame). SOF consists of PRE (preamble) and F-TYPE (frame type). The payload part contains only data for Type A, while containing both ID and Data in Type B. In EOF part, cyclic redundancy check (CRC-16) is contained. The VLID from each transmitter is multiplexed by TDMA [29], and self-position can be obtained by the received VLID only.

Modulation Method

Modulation method of visible light ID system is SC-4PPM, with subcarrier modulation frequency of 28.8 kHz and data rate of 4.8 kbps. Fig. 2.2 illustrates signal waveform of SC-4PPM, where parameter a, b and c are defined as follows.

Amplitude of signal $= (c - a)$ and degree of modulation $= (c - b)/c$. We can vary signal waveform for many applications from value of a, b and c. In this evaluation we use VLID development kit[2], which is consisted of a pair of transmitter and receiver. The specification of transmitter and receiver are described in Table 2.2.

---

[2]Visible Light ID System Development Kit, Nakagawa Laboratory Inc.

Data	0		0		0		1		1		0		1		1	
4PPM Symbol	1	0	0	0	0	1	0	0	0	0	1	0	0	0	0	1
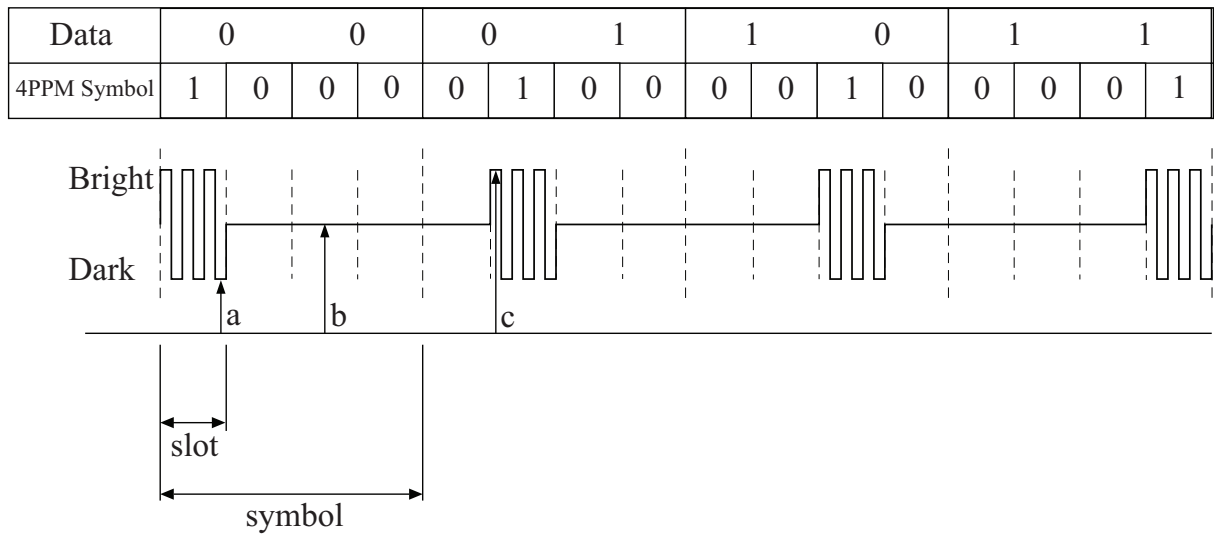
Figure 2.2: Signal Waveform of SC-4PPM.
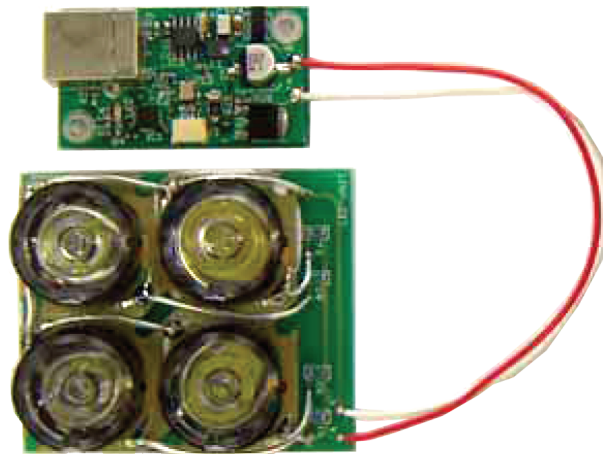
Figure 2.3: VLID development kit (Transmitter).

VLID Transmitter (T_x)

Visible Light ID System transmitter consisted of NVT-001 module and 4 LED, Fig. 2.3 satisfied standard JEITA CP-1222. The transmit data is configurable via NVT-001's USB module. The specifications are stated in Table 2.2.

VLID Receiver (R_x)

Visible Light ID System receiver, Fig. 2.4, satisfied standard JEITA CP-1222, the connection is done via USB connector and enabled serial communication. In the receiver, bandpass filter
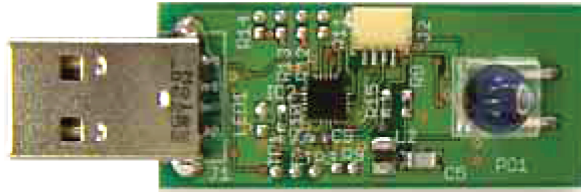
Figure 2.4: VLID development kit (Receiver).

Table 2.3: Specification of 6-Axis Sensor Model AK8976A[3]

Azimuth measurement	3-axis magnetic sensor
Inclination measurement	3-axis magnetic sensor
Magnetic sensor sensitivity	1 μT/LSB
Acceleration sensor sensitivity	45 LSB/G
Operation temperatures	-30° C to $+85^o$ C
Operating supply voltage	$+2.5$ V to $+3.6^o$ V
Package size	4.5 mm $\times$ 4.5 mm $\times$ 1.0 mm

is embedded for optical noise filtering to make the receiving VLID and data stable. CRC and limiter are also embedded to enhance the satiability when the receiving high level optical power.

2.1.3   6-Axis Sensor

6-axis sensor development kit[3] model AK8976A is developed by ASAHI KASEI MICROSYS-TEMS CO., LTD. The AK8976A is a geomagnetism detection type electronic compass IC with built-in 3-axis acceleration sensor; specifications are stated in Table 2.3. The packet size of AK8976A is very small, as shown in Fig. 2.5 (4.5 mm$\times$4.5 mm$\times$1.0 mm), which can be integrated into normal mobile phone. By embedding the AK8976A into the system, a navigation system is achieved with reduced space in a PDA or mobile phone incorporating the GPS function.

Specifically, the AK8976A has the following features. Firstly, Azimuth (β) measurement, where the geomagnetism can be detected by processing 3-axis magnetic sensor output data. Secondly, tilt (ϕ) measurement. The posture (inclination) of the sensor (the equipment incorporating the sensor) can be detected by processing 3-axis acceleration sensor output data. Currently, there are many mobile terminals available in market that embedded 6-axis sensor to provide function of accelerometer and compass, such as iPhone and iPad from Apple, HTC and many other manufacturers.

---

[3]6-Axis sensor model AKD8976A-std, Asahi Kasei Corporation.
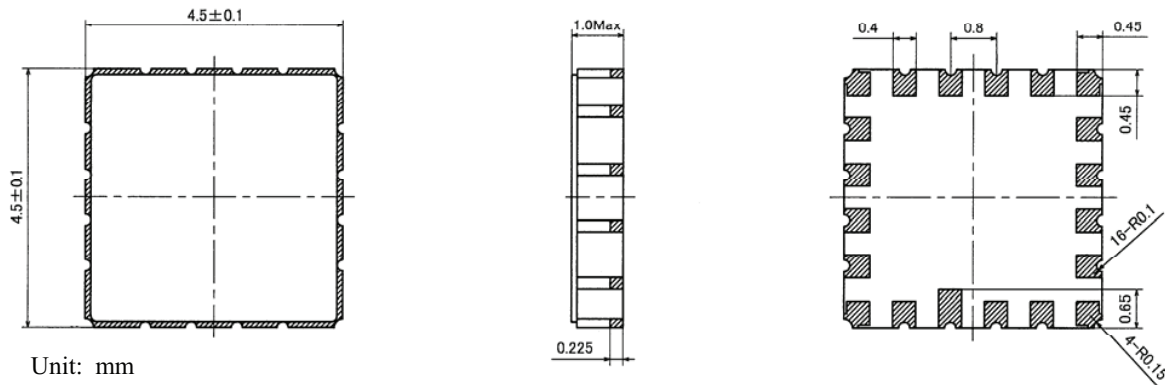
Figure 2.5: Outline dimensions of 6-axis sensor AK8976A.

Table 2.4: Difinition of 6-Axis Sensor AK8976A Log File[3]

TM	Time (hour: minute: second.milisecond)
HH	Geomagnetic measurement data
AA	Acceleration measurement data
TH	Azimuth angle (degree)
PH	Pitch angle (degree)
ET	Roll angle (degree)
TE	Temperature (Converted to centigrade)

   The AK8976A evaluation kit can capture the 6-axis sensor orientation as the log file. Fig. 2.6 illustrates the log file capturing window, where definition of log file is described in Table 2.4. The processing procedures of captured log files are described in the following subsection.

2.1.4   Positioning Display System (PDS)

Evaluations of the proposed architect were conducted numerous times by performing both experiment and simulation to confirm the results. VLID development kit and 6-axis sensor development kit were developed separately, thus the data formats are different. In order to ease up the investigation procedure, graphic user interface (GUI) of VLC based positioning system is developed, as discussed in section 1.3. The developed GUI consists of two parts, which are experimental data acquisition for positioning estimation in section 2.3.2, and data analytical part for receivable range experiment in section 2.3.1.
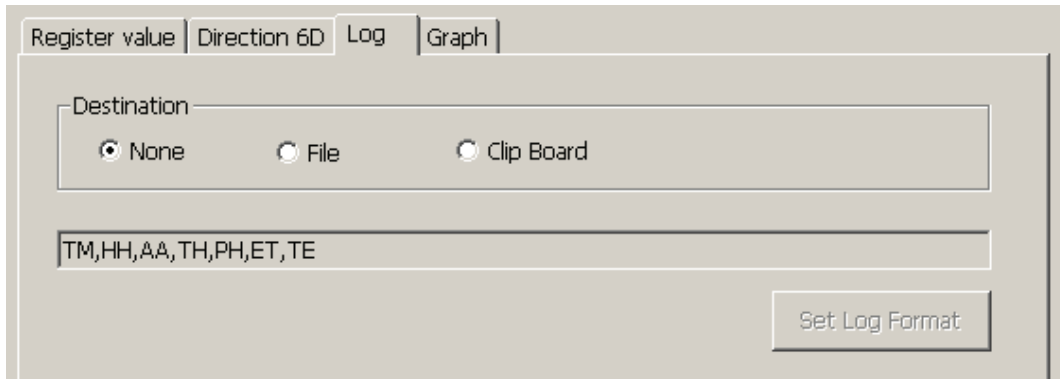
Figure 2.6: Log format of 6-axis sensor AK8976A.
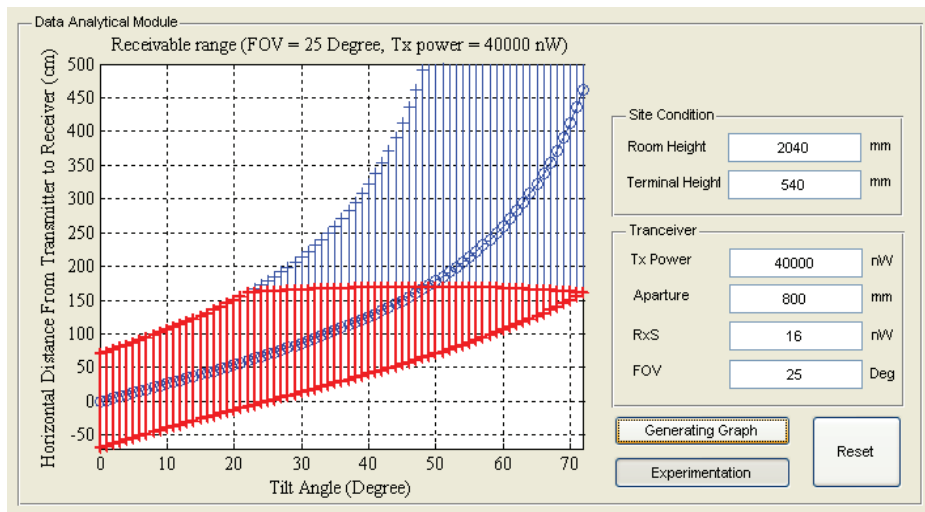
Figure 2.7: GUI of VLC based indoor positioning system (Data analytical module).

Data Analytical Module

The data analytical module is created in order to observe the relationship between the terminal tilt angle and the furthest receivable point of only effect from FOV, effect from channel DC gains. The experimental results are compared in Fig. 2.7. This GUI is used for receivable range calculation, as experimented in section 2.3.1.

Data Acquisition Module

Data acquisition module, as shown in Fig. 2.8, is used for the experiment of positioning estimation, in section 2.3.2. The input of the program is $x-$axis, $y-$axis and times (hour, min, second) of the experimented position. The experimented database is exported in the
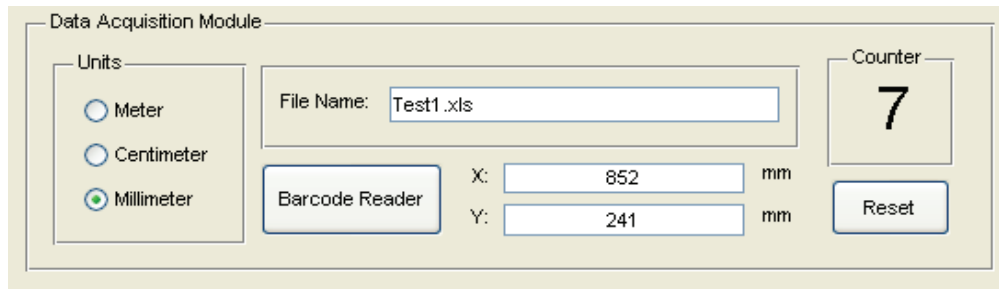
Figure 2.8: GUI of VLC based positioning system (Data acquisition module).

format of MS Excel (.xls), which is to be processed with the log file of 6-axis sensors from Fig. 2.4.

2.2 Proposed System Characterestics

Krishnamurthy [4] identifies accuracy as the most important performance metric in location positioning in mobile environments. Accuracy is usually reported as an error distance between the estimated location and the actual mobile location. The report of accuracy should include the confidence interval or percentage of successful location detection which is referred to as the location precision. To maximize system performance, we verified the proposed system characteristics by making both empirical and numerical analysis. We define two words to justify the characteristic of the proposed system, which are FOV (ψ_c) Limit and Sensitivity ($R_X S$) Limit. Both parameters have crucial impact on positioning estimation accuracy; details are discussed in the following part.

2.2.1 Positioning Characteristics

Data from both VLC tag and 6-axis sensor are combined based on the time measured at receiver, and forwarded to processing unit, as shown in Fig. 1.13. In our case, we use MATLAB as processing unit. VLID can contain information such as (X_{Tx}, Y_{Tx}) and H_R, shown in Fig. 2.9 that can be broadcasted from server via power line communication to each VLC transmitter. Thus, each VLC transmitter broadcasts its own information to the receiver. H_T is a preconfigured variable, which can be calculated from user height and user's posture (e.g. standing, sitting). Therefore, vertical height between receiver and transmitter (H) can be estimated. In our evaluation we assume that H value is equal to 150 cm, because the average vertical distance between terminal in experimenter's hand (with standing posture) to the ceiling in our campus is equal to 150 cm. Positioning estimation can be calculated by data from 6-axis sensor, ϕ and β angulations, together with VLID
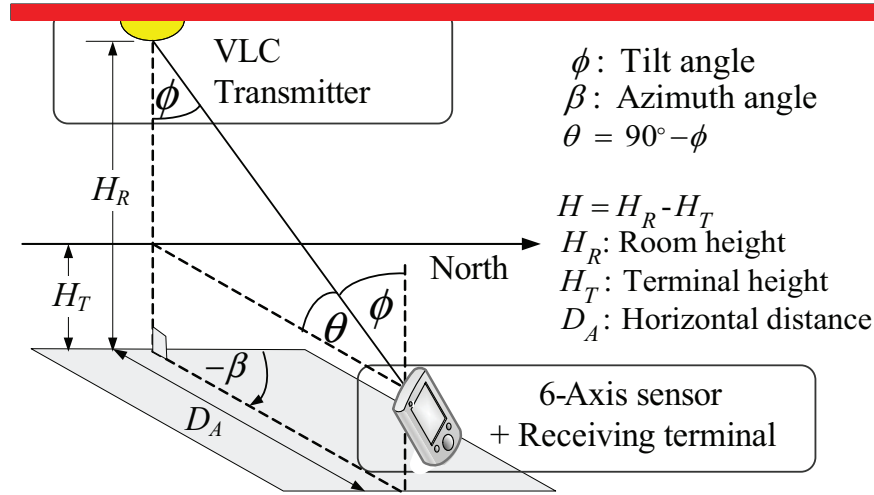
Figure 2.9: Position is estimated from Tilt and Azimuth angulations data from 6-axis sensor.

information (X_{Tx}, Y_{Tx}), as shown in Fig. 2.9 and (2.1) − (2.3).

$$D_A = (H + \Delta H(x)) \cdot \cot \theta \qquad (2.1)$$

$$\Delta H = \begin{cases} \dfrac{1}{\text{b-a}} & \text{for a} \le x \le \text{b}, \\ 0 & \text{for } x < a \text{ or } x > b \end{cases} \qquad (2.2)$$

$$[X_A \ Y_A]^T = [D_A \cos \beta \ \ D_A \sin \beta]^T + [X_{Tx} \ Y_{Tx}]^T \qquad (2.3)$$

where θ is the elevation angle from the ground (θ = 90 - ϕ). The probability density function (PDF) of vertical distance uncertainty is assumed to be uniform distribution represented by H. [a b] in (2.2) represented the uncertainty range which is assumed to be equal to [-10 10] cm. (X_{Tx}, Y_{Tx}) and (X_A, Y_A) are coordinates of the transmitters, which are broadcasted from transmitters, and estimated receiver positions (ERPs) respectively. The accuracy of ERP calculated from preceding information is area level.

2.2.2   FOV Limit

In our proposed system, we consider the effect of tilt angle, Azimuth angle from 6-axis sensor and semi FOV (ψ_c) of the receiver. ψ_c is defined as maximum of receivable signal incident angle. In Fig. 2.10, with one tilt angulations data, ψ_c of the terminal creates three estimated receiver positions (ERPs) A, B and C. ERP A is the line-of-sight (LOS) position explained in (2.1), ERP B and C are the nearest and furthest receivable positions of receivable range, respectively. The ERP and receivable range are calculated by using tilt (ϕ) angulations data from 6-axis sensor and ψ_c of the receiver, as in the following equation.
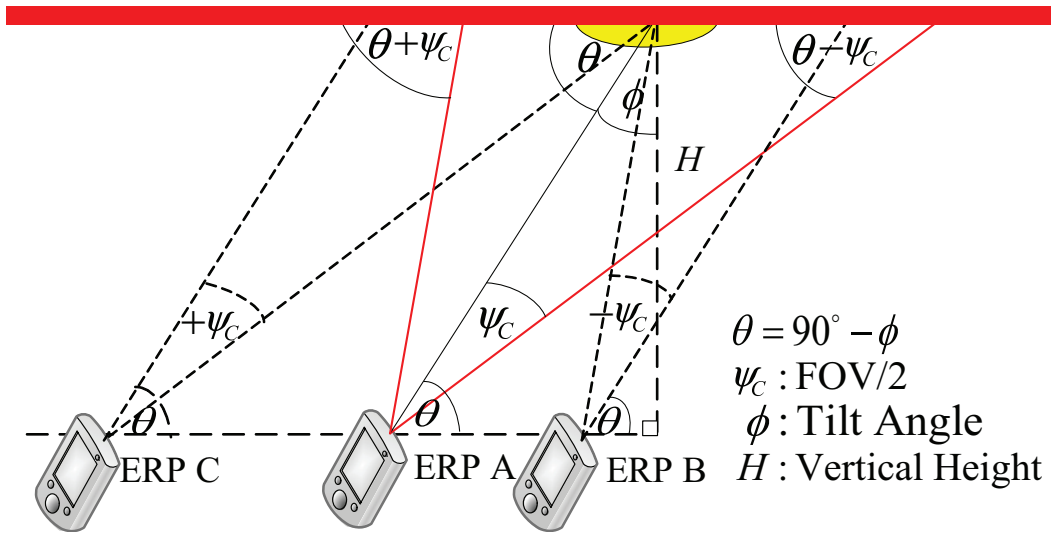
Figure 2.10: An illustration of Tilt angulations plane. ERP A shows the line-ofsight, ERP B and C are the nearest and furthest position from the transmitter.
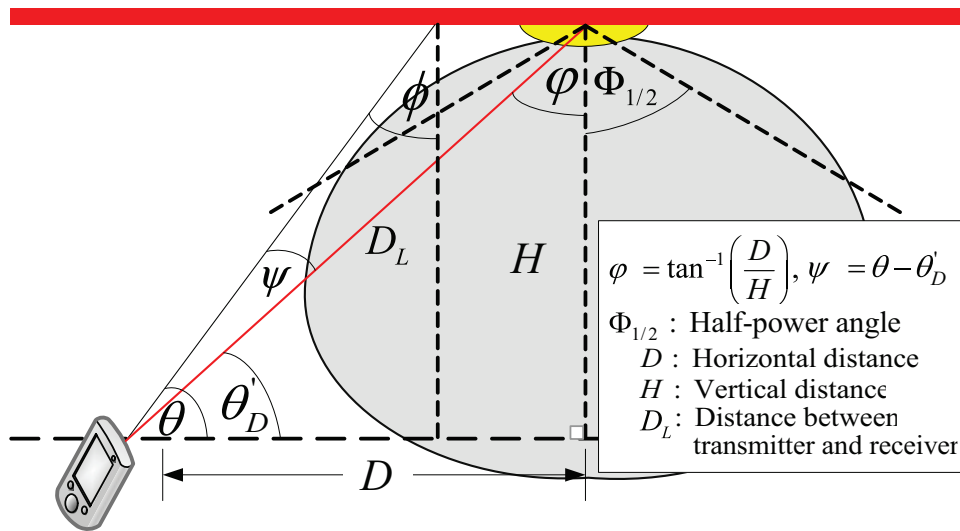
Figure 2.11: An illustration of incident angle of normal light source (ψ) and transmitter's half-power angle ($\Phi_{1/2}$).

$$|D_C - D_B| = H \cdot |\cot(\theta - \psi_c) - \cot(\theta + \psi_c)| \tag{2.4}$$

The D_B and D_C are horizontal distances from VLC transmitter to ERP B and ERP C, respectively. Distance between ERP B and C, calculated from (2.4), is denoted as (signal) receivable range. The receivable range shows the range that a receiver is able to receive VLID transmitted from VLC transmitter, which is physically limited by FOV of the receiver. The smaller receivable range is, the lower estimation uncertainty becomes. In other words, accuracy is increasing in inverse proportion to receivable range. We denote a receivable range that caused by FOV Limit as D_{FOV}, of which is calculated from geometrical line of receiver's FOV, as shown in Fig. 2.4.

2.2.3 Sensitivity Limit

In addition to FOV Limit, the (signal) receivable range can be reduced owing to the effect of channel direct current (DC) gain [24][40], when received optical power (P_r) is lower than receiver's sensitivity ($R_x S$).

$$P_r = \sum^{T_x s} \left\{ P_t H_d(0) + \int_{walls} P_t dH_{ref}(0) \right\} \tag{2.5}$$

P_r is the aggregation of direct (2.6), and reflected components (2.7), which are obtained from GO calculations [20], from all of the possible transmitters (Fig. 2.11 and 2.12).

$$H_d(0) = \begin{cases} \dfrac{(m+1)A}{2\pi D_L^2} \cos^m(\varphi) T_s(\psi) g(\psi) \cos(\psi), \\ \qquad 0 \leq \psi \leq \psi_c, \\ \qquad 0, \\ \qquad \psi > \psi_c, \end{cases} \tag{2.6}$$

where A is the physical area of the optical concentrator. D_L is the distance between a T_x and a R_x, ψ is the angle of incidence, $T_s(\psi)$ is the gain of an optical filter, and $m = -\ln 2/(\ln \cos \Phi_{1/2})$, $\Phi_{1/2}$ is the semi-angle of transmitter. φ is an angle of irradiance calculated from $\tan^{-1}(D/H)$ as shown in Fig. 2.11. ψ_c denotes the receiver's semi FOV.

$$H_{ref}(0) = \begin{cases} \dfrac{(m+1)A}{2\pi^2 D_1^2 D_2^2} \rho dA_{wall} \cos^m(\varphi) \cos(\alpha) \\ \qquad \cos(\delta) T_S(\psi) g(\psi) \cos(\psi), \\ \qquad 0 \leq \psi \leq \psi_c, \\ \qquad 0, \\ \qquad \psi > \psi_c, \end{cases} \tag{2.7}$$
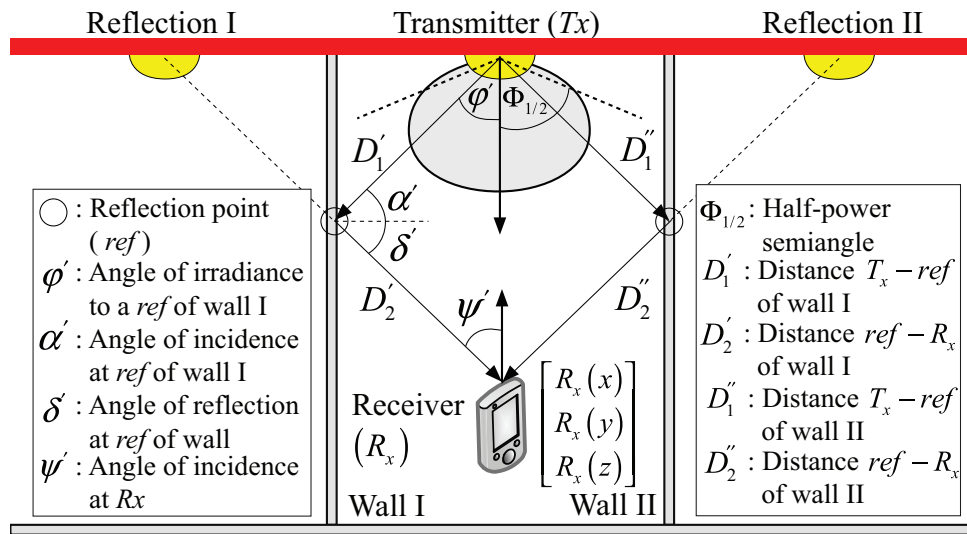
Figure 2.12: An illustration of transmitter (T_x) and its mirror, which are used in geometric optic calculation.
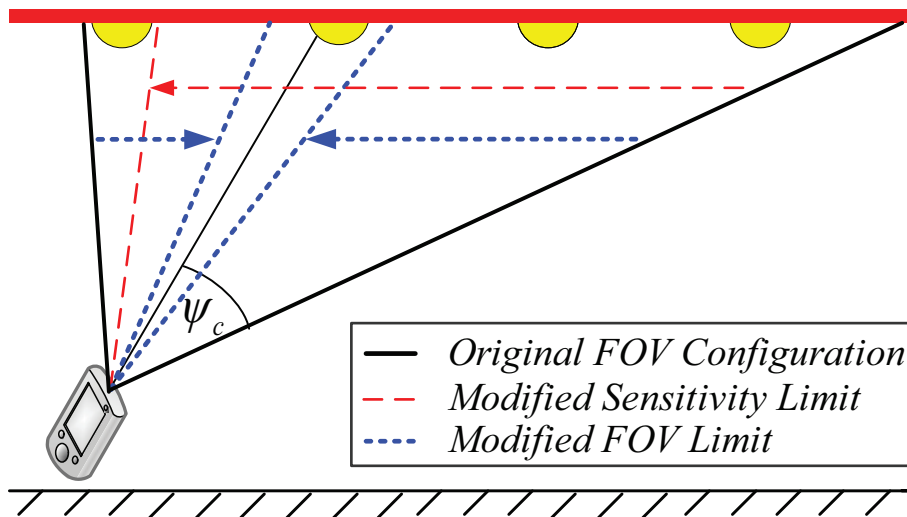
Figure 2.13: Illustration of difference between FOV (ψ_c) Limit, and Sensitivity $(R_x S)$ Limit. FOV limit is unmodifiable physical attribution of the receiver. On the other hand, sensitivity limit is a property of received optical power (P_r), which is modifiable.

Table 2.5: Parameters of Experimental Environment

Room height (H_R)	2.04 m
Terminal height (H_T)	0.54 m
Vertical distance (H)	1.50 m
Room width	1070 mm
Room length	5000 mm
Transmitter location	(490, 1250) mm
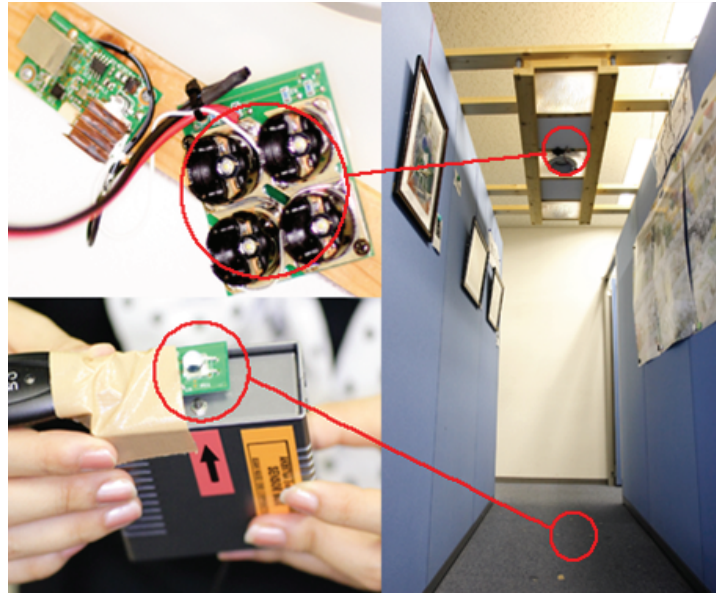
Figure 2.14: Experimental environment the VLC transmitter is attatched at the ceiling and the receiver is attached with 6-axis sensor to measured the angulations data.

where D_1 and D_2 are the distance between T_x and reflective point (ref), and distance between ref and R_x. ρ is the reflectance factor, dA_{wall} is a reflective area of small region. α and δ are the angle of irradiance to ref, and the angle of irradiance to the receiver (Fig. 2.12). The optical concentrator $g(\psi)$ is given as

$$g\left(\psi\right) = \begin{cases} \dfrac{n^2}{\sin^2 \psi_C}, & 0 \leq \psi \leq \psi_c, \\ 0, & \psi > \psi_c. \end{cases} \tag{2.8}$$

Receivers can retrieve VLID only when received optical power (P_r) is higher than the receiver sensitivity (R_xS). The shrinkage of receivable range effects are occurred when P_r is lower than R_xS in the D_{FOV}, denoted as sensitivity limit. We denote the receivable range caused
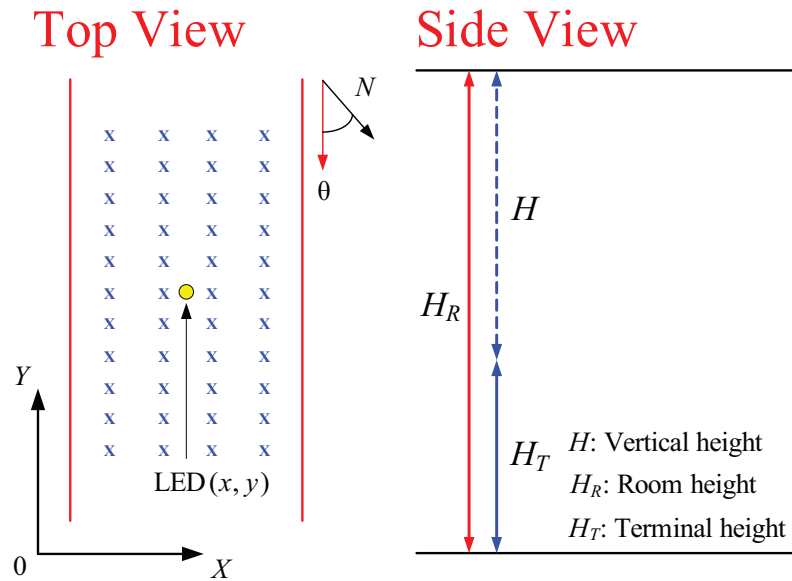
Figure 2.15: Experimentation on error distance estimation, 44 oriented positions with random tilt angle (ϕ) were experimented.

by sensitivity limit as D_{RxS}, of which $D_{RxS} \leq D_{FOV}$. The differences between D_{RxS} and D_{FOV} are shown in Fig. 2.13

2.3   Experimental Setup

Regarding performance evaluation of the proposed system, both experimentation and simulation have been conducted to confirm the results on both aspects of receivable range, and the estimated root mean square of error distance (RMSED). Experimental setup are shown in Fig. 2.14 and Fig. 2.15, where the VLC transmitter is attached to the ceiling and the receiver, and the VLC tag is attached with the 6-axis sensor experimental kit (AK8976A). Data from VLC tag and 6-axis sensor are computed in PC, by using MATLAB. This is to calculate the receivable range, estimated positions and analyze the effect of azimuth angulations error (β_{Err}) from 6-axis sensor in the experimented environment.

We tried to generalize our proposed model, by conducting several experiments with different configurations and simulation are made to confirm the experimental results. The simulation parameters are adjusted to fit the experiments. The experiment and simulation procedures are illustrated in Fig. 2.16, in the hypothesis formulation part; the accuracy of the proposed system are affected by both VLC system ($P_t, H, \psi_c, and \Phi_{1/2}$) and 6-axis sensor ($\phi$, and β). Hence, the evaluations are separated into two parts as receivable range estimation and positioning estimation.
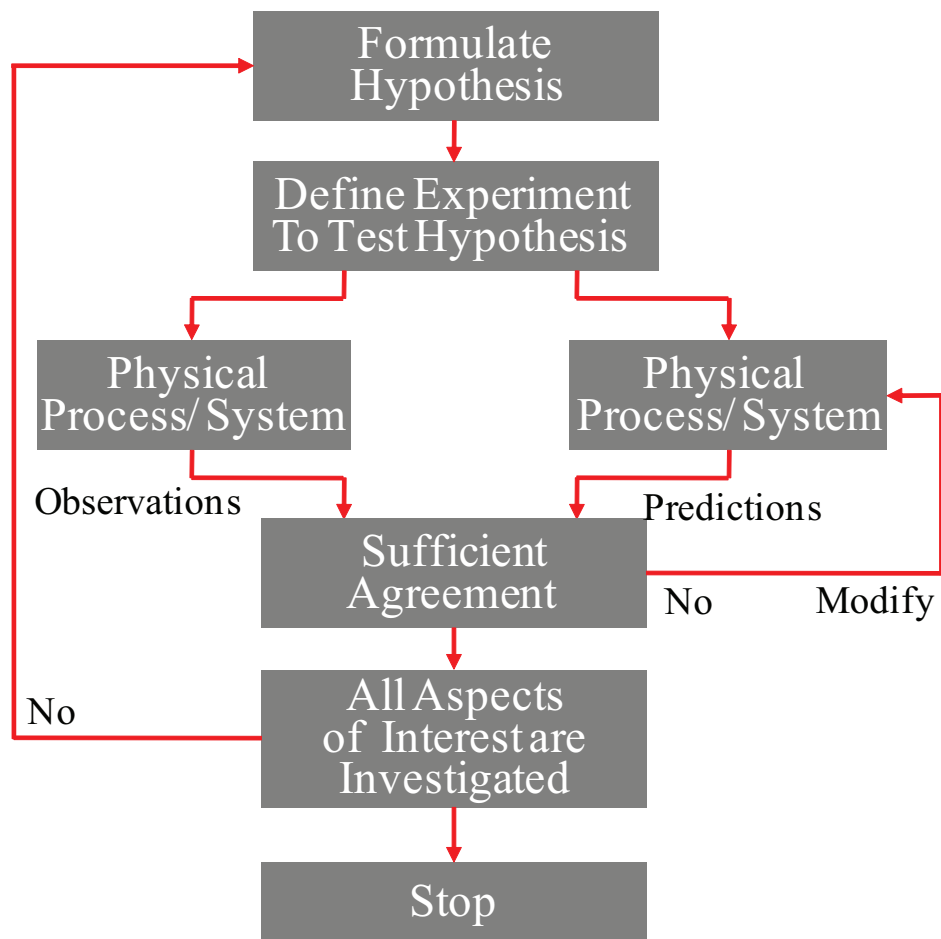
Figure 2.16: Illustration of the experiments and simulation procedures, simulation parameters are adjusted to fit the configuration of the experiments [41].

Table 2.6: Parameters of Experimental Environment

Half power angle ($\Phi_{1/2}$)	50°
Field of view (ψ_c)	25, 17.5, and 10 Degree
Light incident angle (ψ)	$0 \leqslant \psi \leqslant \psi_c$
Transmit optical power (P_T)	400000 nW
Room height (H_R)	2.04 m
Terminal height (H_T)	0.54 m
Vertical distance (H)	1.50 m
Area of receiver (A)	80 mm^2
Filter coefficient ($Ts(\psi)$)	1
R_x sensitivity (R_xS)	16 nWrms
Refraction index (n)	1.460 (Plastic)
Concentrator gains ($g(\psi)$)	11.9346 ($\psi_c = 25^o$)

2.3.1   Receivable Range

In the receivable range investigation, transmitter's optical power (P_t), vertical distance (H), FOV (ψ_c), half-power angle ($\Phi_{1/2}$) from VLC system, only tilt angle (ϕ) from 6-axis sensor are investigated; in other words, 2 dimensional system evaluation as illustrated in Fig. 2.10.

Table 2.2 shows the parameters of VLC transmitter and VLC tag[2]. The default FOV of VLC development tool kit is 25°, in this evaluation the FOVs receiver are modified by limiting the receivable light incident angle (to 17.5 and 10 Degree) rather than replacing the lenses of VLC tag. Hence, no concentrator a gain (2.8) is acquired, the calculated concentrator gains is equal to 11.9346 in every system configurations. Table 2.2 shows the parameters of 6-axis sensor model AK8976.

The experimental environment configurations are shown in Table 2.5. The vertical distance (H) is set as 1.50 m to make it the prospect of average usage height. The experiment has been conducted as illustrated in Fig. 2.10; the measured distance is in reference with the transmitter. The evaluations of receivable ranges are analyzed by the effect of channel DC gains (2.4) and transmitter half-power angle ($\Phi_{1/2}$).

2.3.2   Positioning Estimation

In the positioning estimation experiment, transmit optical power (P_T), vertical distance (H), FOV (ψ_c), half-power angle ($\Phi_{1/2}$) from VLC system, tilt angle (ϕ) and azimuth angle (β) from 6-axis sensor are also investigated; in other words 3 dimensional system evaluation. The experimental environment is set as shown in Fig. 2.15, where numbers of experimented positions are arranged under VLC transmitter. For each position, 10 experiments are performed with unarranged tilt angle (ϕ). The configuration of experimental environment is

---

[2]Visible Light ID System Development Kit, Nakagawa Laboratory Inc.
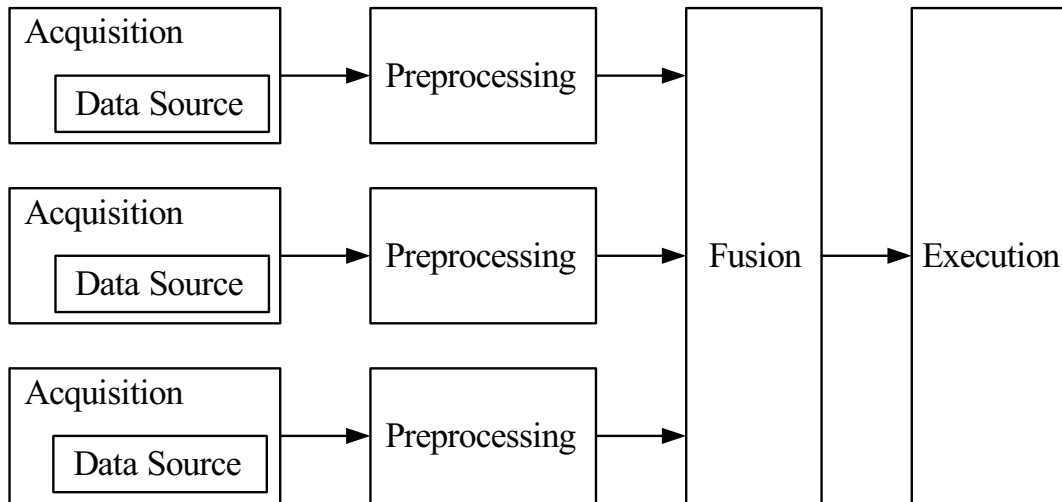
Figure 2.17: General architecture for data fusion.

stated in Table 2.2, Table 2.3, and Table 2.6. Three of FOV configurations have been investigated, under 44 oriented positions with 10 experiments at each position. Hence, 1320 (3 × 44 × 10) experiments were conducted. The evaluation process is described in the following subsections.

2.3.3   Information Fusion and Integration

Information integration corresponds to the use of information from several sources (or the same source with several times) to accomplish a particular task. Information fusion refers to particular mathematical functions, algorithms, methods, and procedures for data combination [42]. The architecture for information integration is illustrated in Fig. 2.17.

In our proposed model, data sources are from 6-axis sensor log files, section 2.1.3, and experimented positions, which is illustrated in section 2.1.4. Both 6-axis sensor in Fig. 2.18 and the experimented positions data in Fig. 2.19 are preprocessed by inserting the sample acquired time and converting azimuth angle, this is described in section 2.3.4. The data fusion process is done by matching the sample acquired time from both data sources. The executions of data are conducted under MATLAB environment, which is described in the following subsection.

2.3.4   Angulations Conversion

Before information fusion, section 2.3.3, the 6-axis sensor data must be converted from azimuth (β) angulations in reference with North into angle reference with VLC transmitter,

Figure 2.18: Experimented log file of 6-Axis sensor, the first three columns show the samples acquired time (hour: min: second), which is used as fusion indicator with data from VLC based positioning GUI.

Figure 2.19: Experimented data from VLC based positioning GUI. The first column shows experimented order, where second and third show coordination of experimentd positions. Column four to six show the samples acquired time (hour: min: second).
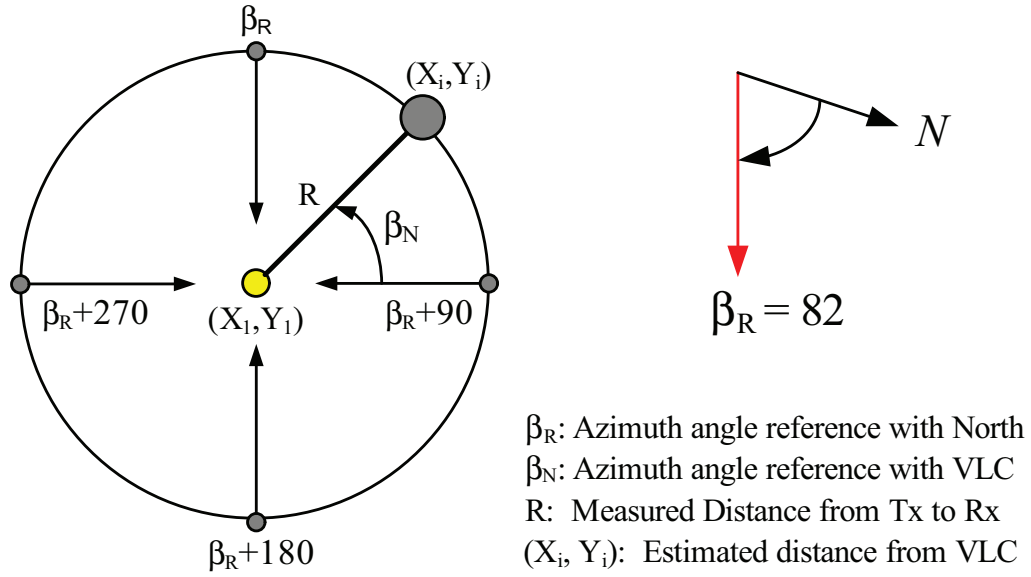
Figure 2.20: Angulations conversion, the data from 6-axis sensor is mapped in to angle reference with VLC transmitter.

as in Fig. 2.20. The derivation of azimuth angle toward VLC transmitter (β_N) is shown in (2.9).

$$\beta_N = (\beta_R + 90) - \beta \tag{2.9}$$

Besides, the actual experimented azimuth angle toward VLC transmitter (β_A) is shown in (2.10). Where R is the measured distance from T_x to R_x, but $\hat{R}$ is the distance of estimated user position A, B and C, as illustrated in (2.1) and (2.3).

$$[\beta_A] = \left\{ \cos^{-1} \left(\frac{Xi}{\hat{R}} \right) \right\} \cap \left\{ \sin^{-1} \left(\frac{Yi}{\hat{R}} \right) \right\} \tag{2.10}$$

2.4 Proposed Positioning Modules

In this section, we discuss the methodologies that are utilized for positioning estimation along with its requirements. Based on occurrence of D_{RxS}, we proposed a positioning estimation scheme which is switching estimated receiver position (SwERP) for the case that light attenuator is deployed $D_{RxS} < D_{FOV}$. We also defined the case that $D_{RxS} = D_{FOV}$ as general orientation sensor's information (GOSI), because of its similarity with other system that has FOV. The proposed SwERP scheme requires two additional modules, FOV Limit
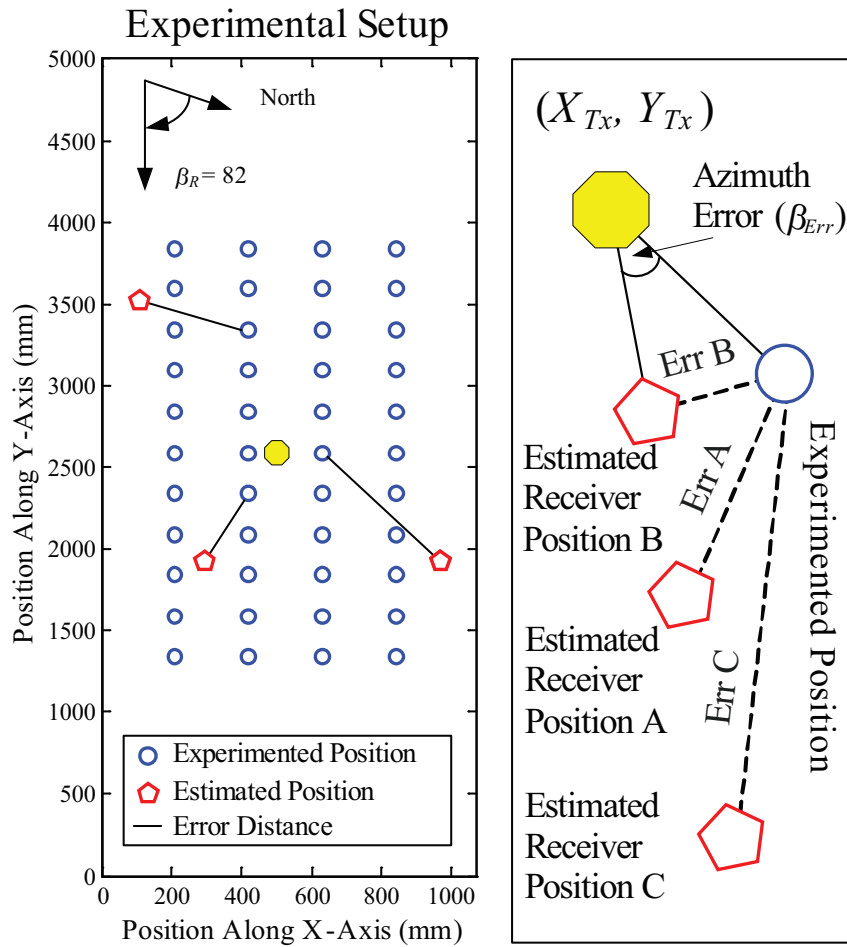
Figure 2.21: Position is estimated from receivers ψ_c, ϕ and β from 6-axis sensor.

classification and nearest transmitter classification algorithm, of which will be discussed in the following sections.

2.4.1 General Orientation Sensor's Information (GOSI)

We defined GOSI as the case that $D_{RxS} = D_{FOV}$, which is the general condition of any system that has FOV. For the simplicity in calculation only a single ERP is utilized. Root mean square is used to illustrate total distance error between each of the experimented position and its estimated receiver position as in Fig. 2.21. The root mean square of error

distance (RMSED) can be calculated by

$$RMSED = \sqrt{\frac{1}{n}\sum_{i=1}^{n}ErrD_i^2},$$

$$= \sqrt{\frac{ErrD_1^2 + ErrD_2^2 + \cdots + ErrD_n^2}{n}}, \tag{2.11}$$

where n is the numer of estimated positions. Intuitively, estimated position can be regarded as position calculated from receiver's tilt angle (ERP A). Nevertheless, in the practical usage wider FOV provides wider communication range [24], which is the main purpose of VLC. Hence, we analyzed RMSED achieved from each ERP (A, B and C) to find the one that provide the lowest RMSED.

2.4.2 Switching Estimated Receiver Position (SwERP)

The SwERP scheme utilizes more than one ERP in the positioning estimation to eliminate dependence between achievable RMSED from each ERP and tilt angulations. The proposed scheme is working on the basis that $D_{RxS} < D_{FOV}$, which is the effect of sensitivity limit. As shown in Fig. 2.13, at the higher receiver's tilt angle, receivable range is shrunken to ERP B. Intuitively, ERP B should provide higher accuracy at the higher receiver's tilt angle than those with ERP A and C. Hypothetically, when sensitivity limit occur receiver's tilt angel (ϕ) is affecting RMSED of each ERP.

In this proposed scheme, SwERP, we denote the tilt angle that estimator switched from utilizing one ERP to the other, e.g. ERP A to ERP B, and provided the lowest achievable RMSED as the proper switching angle (ϕ_S). On the other hand, the tilt angles that do not provide lowest achievable RMSED are denoted as improper switching angle (ϕ_I). In $(2.12)-(2.15)$ derive polynomial regression algorithm is used to predict relationship between RMSED calculated from each ERP versus its tilt angulations (ϕ), where x_i is the value calculated from ERP A, B or C. We use an intersection point of the 6-th order polynomial regression (m) of each ERP, from the 440 experimented positions (i) of 3 receiver's FOV configuration, to calculate a proper switching angle (ϕ_S).

$$y_i = a_0 + a_1 x_i + a_2 x_i^2 + \cdots + a_m x_i^m + \varepsilon_i, (i = 1, 2, \ldots, n) \tag{2.12}$$

$$\begin{bmatrix} y_1 \\ y_2 \\ \vdots \\ y_n \end{bmatrix} = \begin{bmatrix} 1 & x_1 & \cdots & x_1^m \\ 1 & x_2 & \cdots & x_2^m \\ \vdots & \vdots & & \vdots \\ 1 & x_n & \cdots & x_n^m \end{bmatrix} \begin{bmatrix} a_0 \\ a_1 \\ \vdots \\ a_m \end{bmatrix} + \begin{bmatrix} \varepsilon_1 \\ \varepsilon_2 \\ \vdots \\ \varepsilon_n \end{bmatrix} \tag{2.13}$$

$$Y = \mathbf{X}\vec{a} + \varepsilon \tag{2.14}$$

The estimated polynomial regression coefficients using ordinary least squares estimation is [43]

$$\hat{\vec{a}} = \left(\mathbf{X}^T\mathbf{X}\right)^{-1}\mathbf{X}^T Y \tag{2.15}$$

The objective of utilizing polynomial regression is to study the relationship between switching angle (ϕ_S) from experimental data and achievable RMSED of each ERP in the generalized manner.

2.5 Performance Evaluation

We made feasible study on all aspects of the proposed solution architect characteristic, for the purpose of future design and implementation. Performance of the proposed architecture is varied from the following factors, tilt (ϕ) azimuth angulations error (βErr), receiver's FOV (ψ_c), sensitivity ($R_X S$) and uncertainty of terminal height (ΔH). Details of each factor are explained in the following sections.

2.5.1 Azimuth Angulations Error (β_{Err})

The azimuth error (β_{Err}) is the error from magnetic sensor of 6-axis sensor. The azimuth error is calculated from actual azimuth angle (β_A) - azimuth angle toward VLC transmitter (β_N). Derivations of the actual azimuth angle (β_A) and azimuth angle toward VLC transmitter (β_N) are described in (2.10) and (2.20), respectively.

The azimuth angulations error (β_{Err}) shows normal distribution, where mean value is nearly 0°, as illustrated in Fig. 2.22. In this section PDF (Probability Distribution Function) of azimuth angulations error (β_{Err}) is studied, the normal distribution equation is illustrated as follows.

$$f\left(x|\mu,\sigma\right) = \frac{1}{\sigma\sqrt{2\pi}}e^{\frac{-(x-\mu)^2}{2\sigma^2}} \tag{2.16}$$

where μ is expected value and σ is standard deviation.

The experimental azimuth error shows $\mu = 7.84^o$ and $sigma = 36.18^o$, of 1320 experiments. Nevertheless, the PDF does not fit the azimuth error distribution. This can be the result of interference at experimental environment; further investigation is conducted by neglecting the β_{Err}, which has value more than the investigated angle, as in Table 2.7.

Table 2.7: Percentage of Error Under Investigated Angle

Azimuth error ($|\beta_{Err}|$) < 100	96.28 % of Error Distribution
Azimuth error ($|\beta_{Err}|$) < 75	94.24 % of Error Distribution
Azimuth error ($|\beta_{Err}|$) < 50	89.84 % of Error Distribution
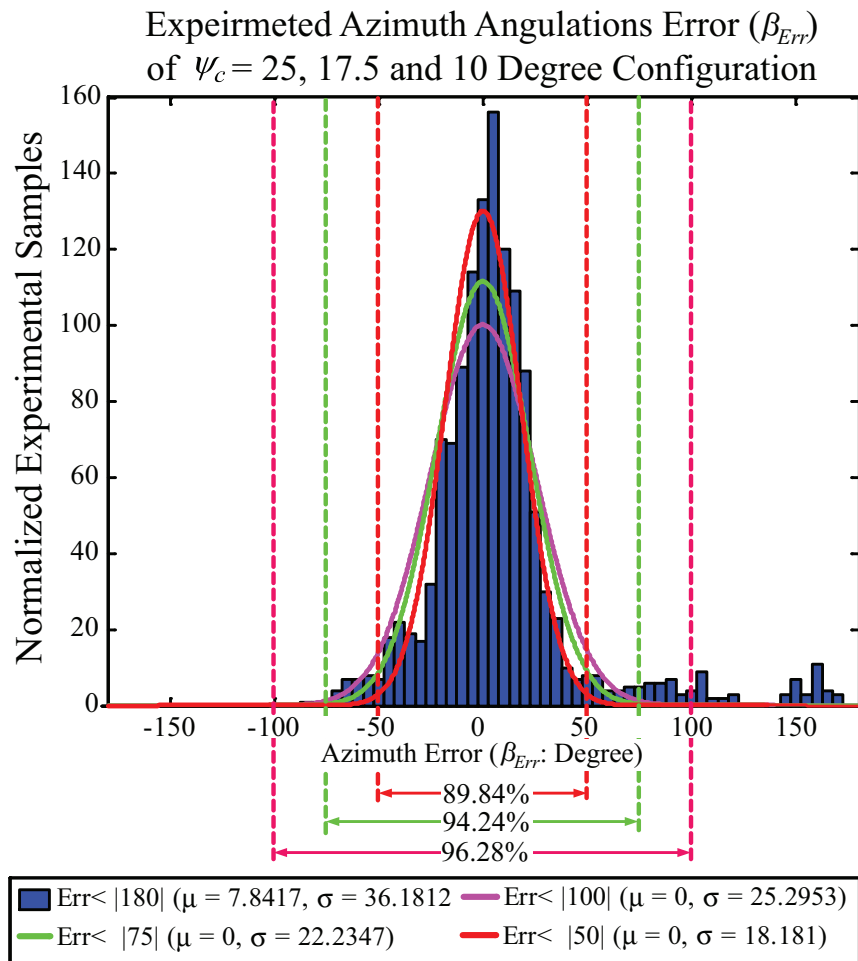
Figure 2.22: Azimuth (β_{Err}) error distribution analysis.

The azimuth error's PDF that is calculated from $|\beta_{Err}| < 50^o$ have 89.84 % of azimuth errors; this shows the highest compatibility with the experimental results. Thus, $\mu = 0^o$ and $\sigma = 18.18^o$ are selected as PDF of azimuth error distribution. Furthermore, the positions that have $|\beta_{Err}|$ more than investigated angle are illustrated in Fig. 2.23, only 6 positions from 44 positions have $|\beta_{Err}| > 50$.

2.5.2   Receivable Range Investigation Analysis

The actual receivable range of the proposed system can be shrunken from the one calculated from geometrical line of receiver's FOV due to the attenuation of channel DC gains (2.6). To be specific when sensitivity limit occurred, ERP C is shrunken. Computer simulations using the same parameter as experiments were performed, the comparison of experimental
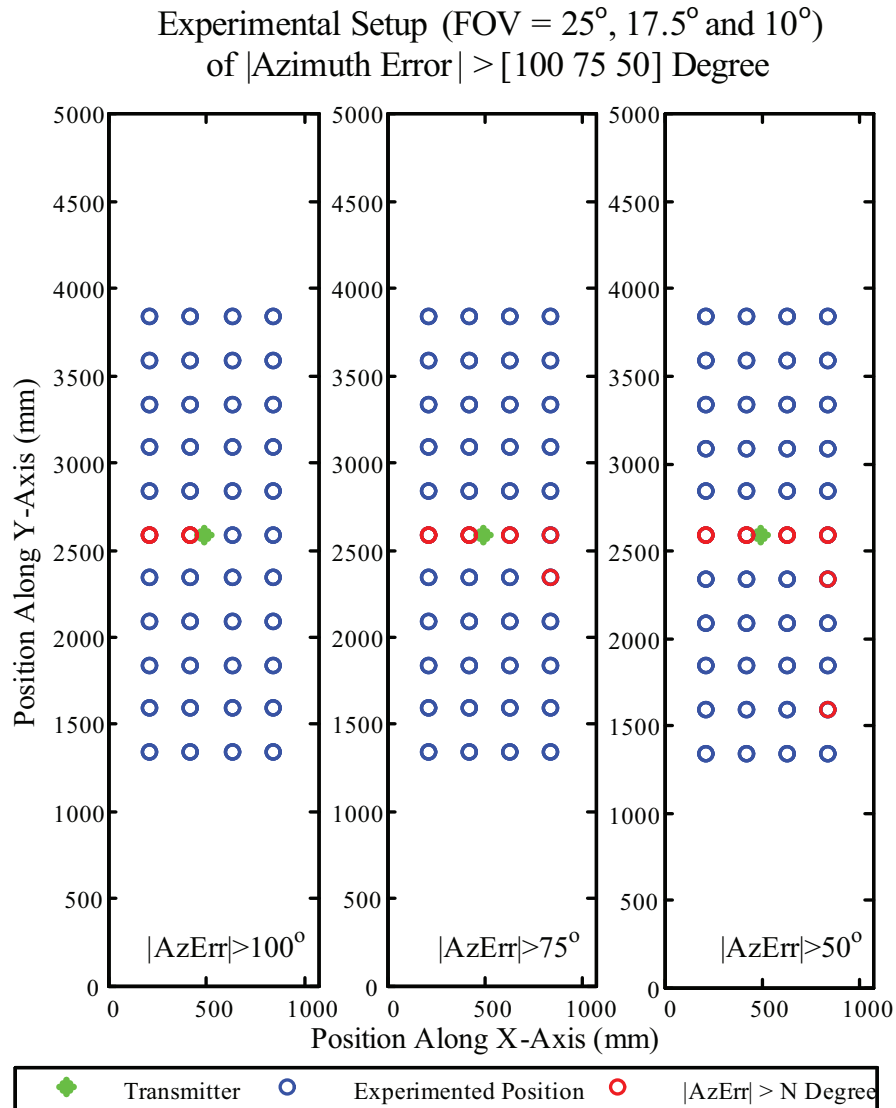
Figure 2.23: Positions that azimuth error occur higher than the investigated value (100, 75 and 50 degree).

and simulation results are illustrated as in Fig. 2.24. The x-axis shows the experimented angle, while the y-axis shows the receivable positions relative with VLC transmitter. The minus distance shows the receivable distance in the opposite direction. The line with o sign shows line-of-sight positions calculated from receiver's tilt angle, also denoted by ERP A. The trend lines with + at each end show FOV Limit, which defines receivable range (D_{FOV}). The D_{FOV} is calculated from geometrical line of receiver's FOV. Nevertheless, the actual receivable range (D_{RxS}) is shrunken from D_{FOV} due to the attenuation of channel direct
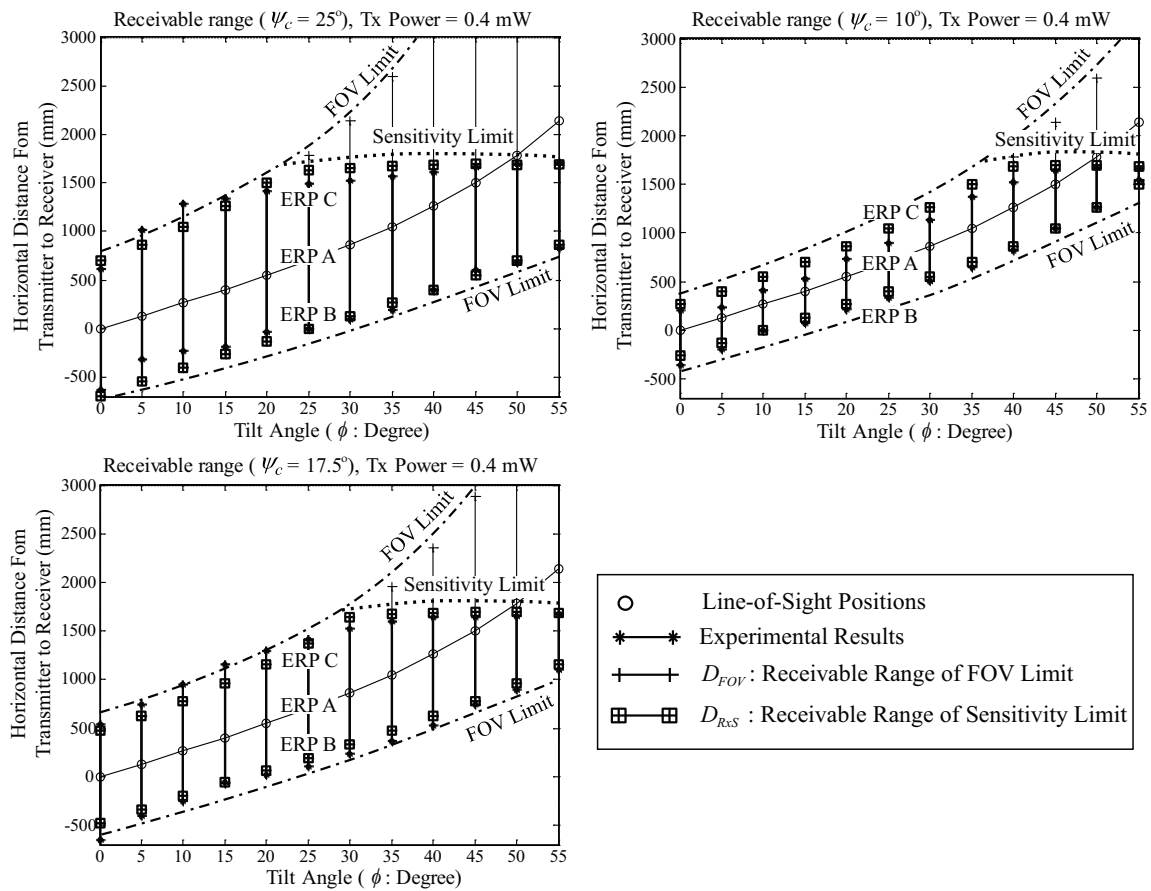
Figure 2.24: Comparison of the relationship between terminal's tilt angle ($\psi_c = 25$, 17.5 and 10 degree) and furthest receivable point (in the case of effects from FOV only, effects from channel DC gains, and experimental results, respectively).

current (DC) gains, referred to as sensitivity limit; as shown with lines with ⊞ sign at both end. The experiment of receivable range conducted to confirm the simulation results are shown as line with asterisk symbol.

The results from both empirical and analytical examination show small error, confirm that our analytical model is correct. Consequently, we perform simulation to illustrate relationship between FOV and sensitivity limit by utilizing the same parameters as shown in Table 2.5, where concentrator gain $g(\psi)$ The results from both empirical and analytical examination show small error, confirm that our analytical model is correct. Consequently, we perform simulation to illustrate relationship between FOV and sensitivity limit by utilizing the same parameters as shown in Table 2.5, where concentrator gain $\psi_c = 25^o$. Fig. 2.25 shows the comparison of receivable range simulation of each tilt angulation, from three FOV's configuration, where x-axis is receiver's tilt angle and y-axis is the receivable position
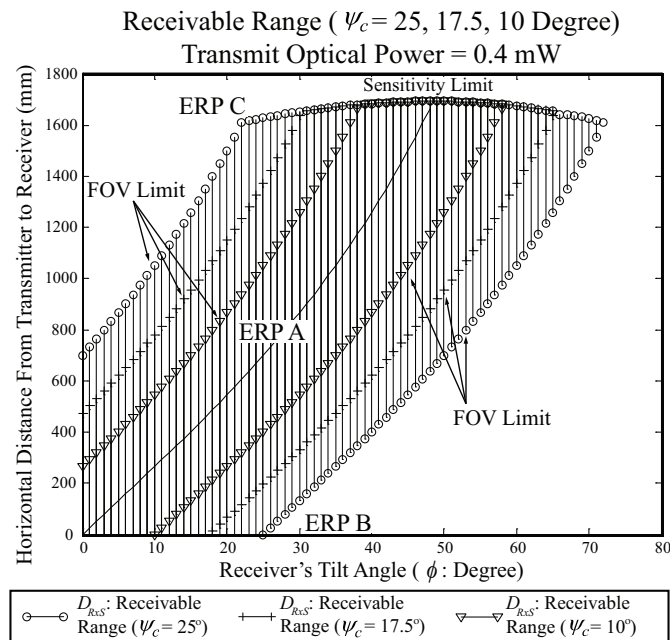
Figure 2.25: Illustration of FOV Limit of $\psi_c = 25$, 17.5 and 10 degree with $R_X S = 16$ nW.
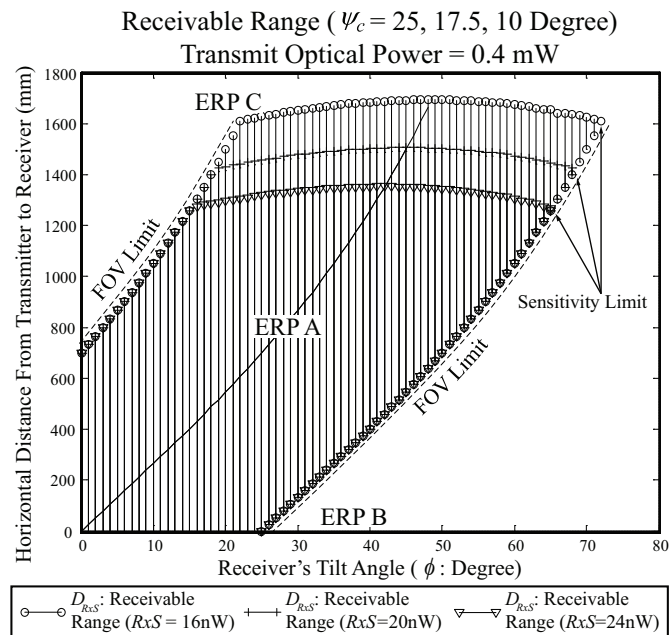
Figure 2.26: Illustration of Sensitivity Limit of $R_X S = 16$, 20 and 24 nW with $\psi_c = 25^o$.
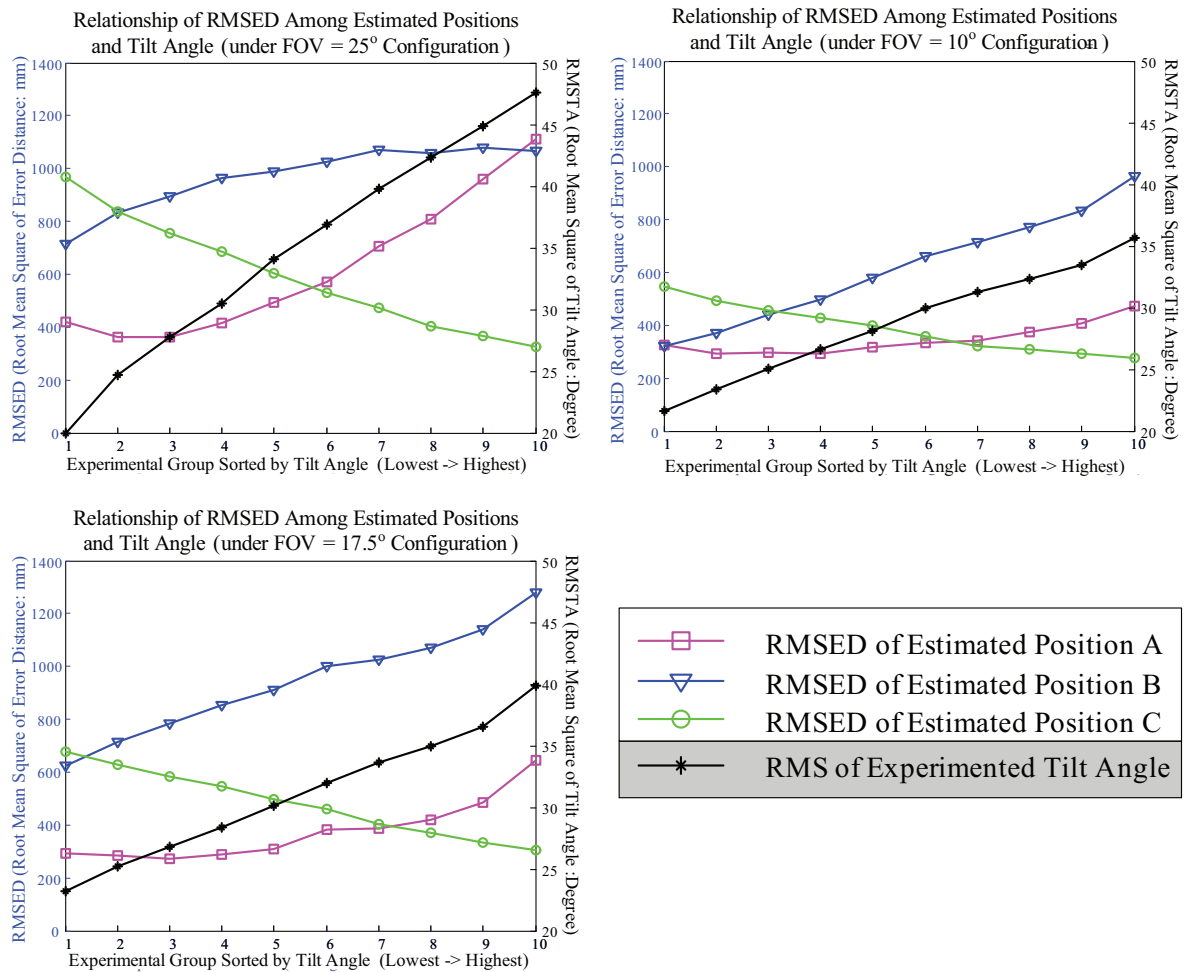
Figure 2.27: Relationship of RMSED among estimated receiver positions and tilt angle (under receiver's FOV = 25,17.5, 10 degree configuration).

relative with transmitter. The result shows that receivable range is decreasing in proportion to receiver's FOV, and receivable range is shrunken toward receiver's line-of-sight (ERP A). In all of the investigated cases, the sensitivity limit is presence. The furthest receivable position (ERP C) is start to shrink at tilt angle (ϕ_{MAX}) is equal to 22°. ERP C is equal to line-of-sight position (ERP A) at $\phi_{MAX} = 48^o$, and equal to nearest receivable position (ERP B) at $\phi_{MAX} = 72^o$. To sum up, if sensitivity limit presence, the higher tilt angulation is, the higher accuracy becomes. The effect of sensitivity limit is also presented in Fig. 2.26. Unlike FOV Limit, receivable range occurred by sensitivity limit, D_{RxS}, is shrunken toward the ERP B.
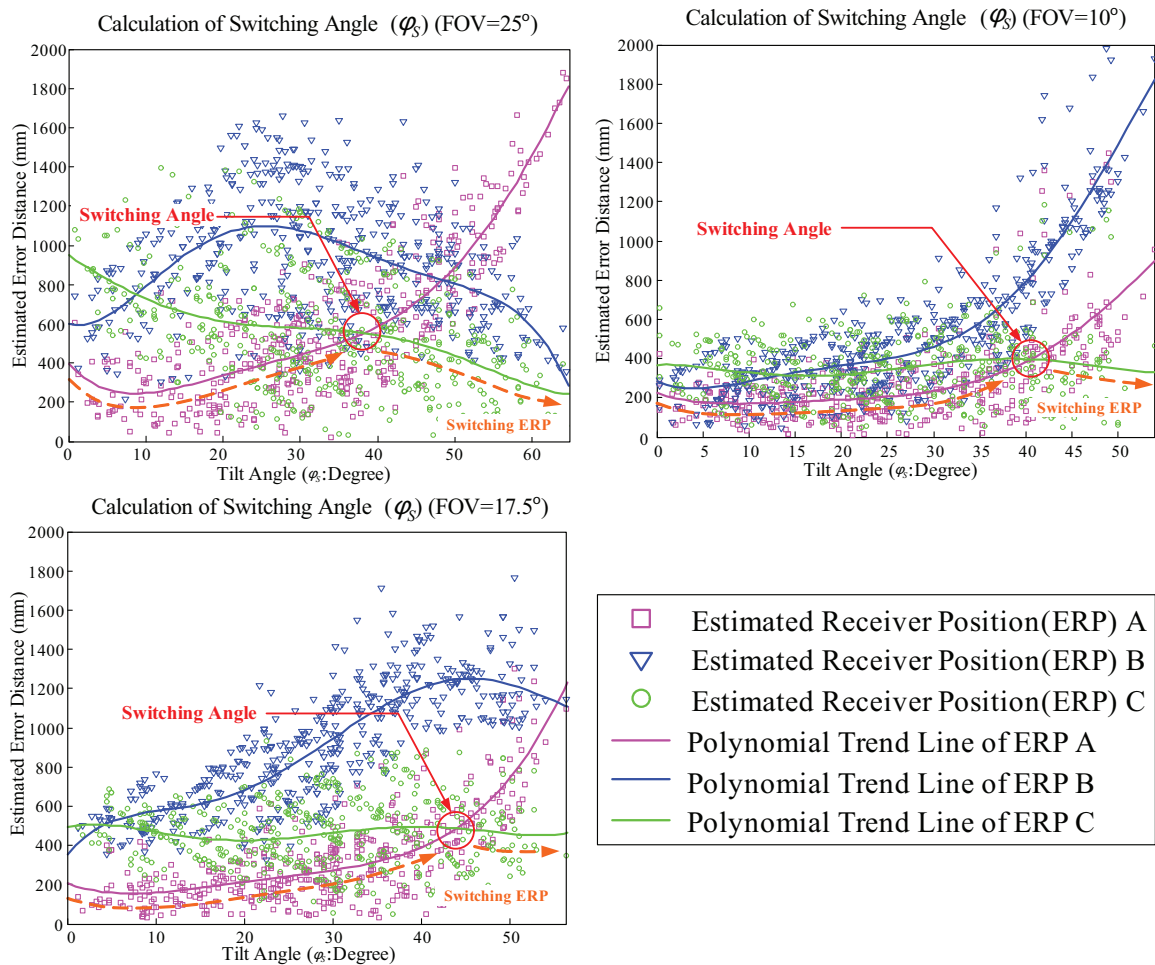
Figure 2.28: Illustration of switching angle (ϕ_S) calculation, derived from intersection point of estimated receiver position A and C polynomial 6th order trend line of receiver's FOV = 25, 17.5, 10 degree configuration.

Table 2.8: Calculated Switching Angle (ϕ_S)

Experimental Configuration	Switching Angles (ϕ_S)
$\psi_c = 25$ Degree	38.31 Degree
$\psi_c = 17.5$ Degree	43.90 Degree
$\psi_c = 10$ Degree	40.51 Degree

2.5.3 Relationship Between Tilt Angulations and Estimated Receiver Position

In this section the further investigations on relationship of RMSED among estimated receiver position and tilt angle (ϕ) is shown. In section 2.4.1, experiments were conducted in 44
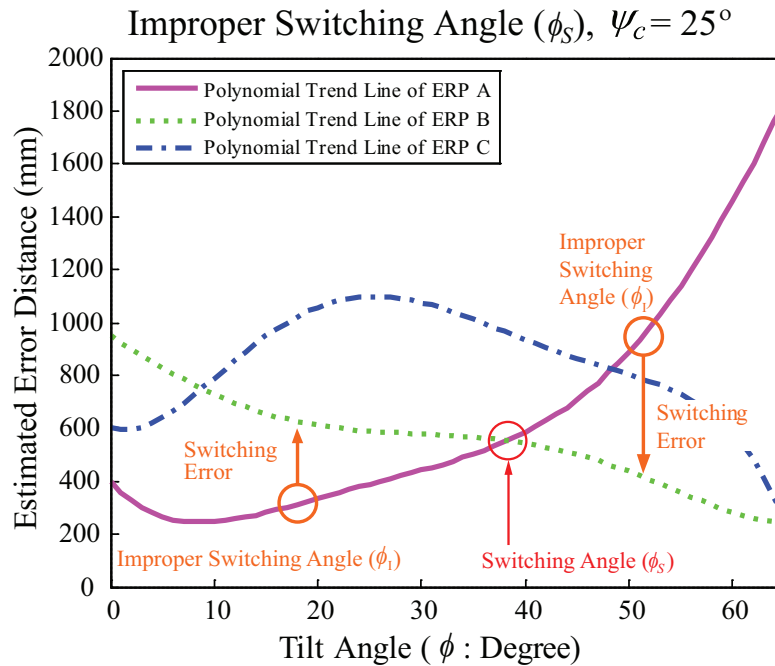
Figure 2.29: Illustration of improper switching angle (ϕ_I) and switching error of receiver's FOV = 25 degree configuration.

positions, 10 times at each position for receiver's FOV configuration.

The influence of tilt angle on RMSED among utilization of ERP (estimated receiver position) are studied, by classifying tilt angulations of each experimented position; arranged by lowest to highest tilt angulations. Thus, we got 10 experimental groups sorted by tilt angle (ϕ), in each group root mean square of tilt angle (ϕ) and error distance from utilizing each estimated receiver positions are calculated. Figure 2.27 illustrate the dependency between tilt angle and estimated error distance. The achievable RMSED of ERP A and ERP B, are increasing in proportion to the receiver's tilt angle, while RMSED of ERP C is in inverse proportion.

The x-axis shows experimental group number sorted by tilt angle; experimental group 1 has the lowest RMSTA (Root Means Square of Tilt Angle) where group 10 has the highest RMSTA. The left Y-axis shows the RMSED of each estimated receiver positions, while the right Y-axis shows the RMSTA. Figure 2.27 illustrate that by switching from ERP A to C, utilizing plural estimated position scheme, this can prevent RMSED from increasing as tilt angle become higher, or in other words solving the dependency between estimated error distance of each ERP and receiver's tilt angle. The appropriate tilt angle (ϕ), to perform switching between ERP, is studied in the following sections.
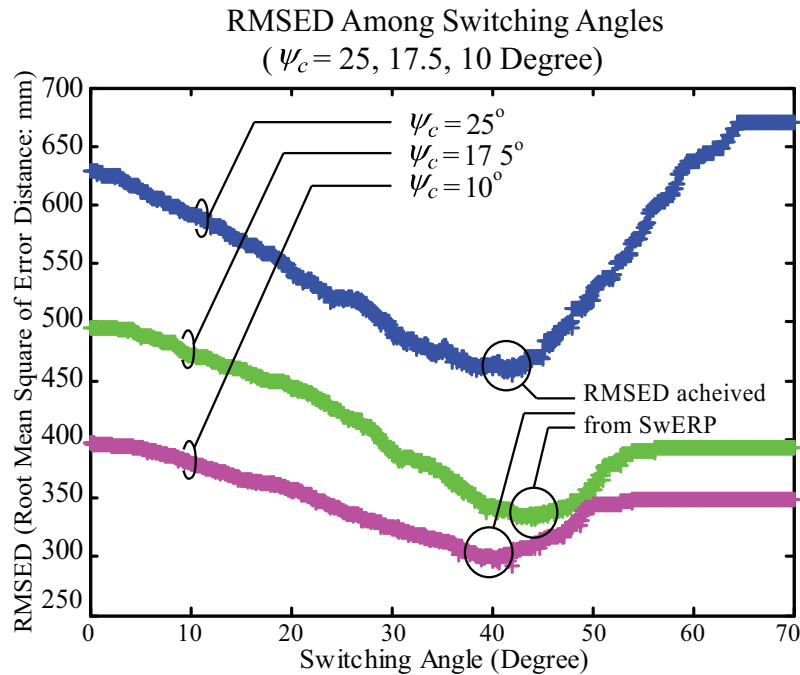
Figure 2.30: Comparison of acheivable RMSED among utilized tilt angles as switching angle (FOV=25, 17.5, 10 degree).

Switching Angle Calculation

The relationship between tilt angle and RMSED of estimated receiver positions, Fig. 2.27, show that switching ERP between A and C can prevent RMSED from increasing as the tilt angle becomes higher. In this section, the tilt angle (ϕ), which constitutes most impact on reducing system RMSED when switching between estimated receiver positions is utilized. The switching angles (ϕ_S), are shown in this section.

In this study switching angle (ϕ_S) calculation is done by utilizing polynomial regression algorithm from the ERP A, B and C. Each trend line is calculated from estimated position of 440 experiments in each configuration from (2.13) the polynomial 6th order ($m = 6$) is used as the trend line. Orange lines in Figure 2.28 illustrate the switching ERP technique, at tilt angle higher than switching angle (ϕ_S) ERP C is utilized instead of ERP A. The highest estimated error distance is limited at the switching angle (ϕ_S). The calculated switching angle (ϕ_S) of each FOV is described in Table 2.8.

Improper Switching Angle (ϕ_I)

In the case that switching is performed between ERP A and ERP B at other angles rather than the calculated switching angle (ϕ_S), we defined it as improper switching angle (ϕ_I),

Table 2.9: Performance Comparison among Conventional System and the Propose Scheme

FOV (ψ_c)	Conventional System		w/ Azimuth	GOSI (RMSED: mm)						SwERP (RMSED: mm)			
	Estimated Area (mm²)	Estimated Range (mm)	Estimated Range (mm)	w/ β_{Err}			w/o β_{Err}			Switching w/ β_{Err}	Switching w/o β_{Err}	Improvement (%)	
				C	A	B	C	A	B			w/ β_{Err}	w/o β_{Err}
25°	9,025,874	3,390	1,695	976	671	629	893	577	599	463	364	72.68	78.53
17.5°	9,025,874	3,390	1,695	960	393	496	904	295	460	336	248	80.18	85.37
10°	9,025,874	3,390	1,695	646	349	398	566	231	331	298	183	82.42	89.20

Table 2.10: N % of Error Distance

FOV (ψ_c)	N % of Error Distance without β_{Err} (mm)								N % of Error Distance without β_{Err} (mm)							
	ERP C		ERP A		ERP B		ERP C		SwERP		ERP A		ERP B		SwERP	
	90 %	95 %	90 %	95 %	90 %	95 %	90 %	95 %	90 %	95 %	90 %	95 %	90 %	95 %	90 %	95 %
25°	1375	1450	1090	1284	968.7	1089	752.0	820.1	1283	1376	958.5	1186	963.4	1088	588.8	672.5
17.5°	1297	1419	615.4	783.5	707.5	770.8	522.8	599.9	1233	1291	510	607	673.7	735.3	408.4	485.0
10°	1079	1280	503.8	633.5	544.1	633.5	421.1	500.1	971.4	1132	384.5	461.1	507.4	548.3	282.1	331.5

as illustrated in Fig. 2.29. The RMSED can be increased if the switching is performed at improper switching angle (ϕ_I). The effect of improper switching angle (ϕ_I) is shown in Fig. 2.30. The achievable RMSEDs are varied between the one achieved from utilizing only ERP B or ERP A. For the case that switching angle is set as 0°, the achievable RMSED is equal to the one achieved from utilizing only ERP B. Fig. 2.30 shows that the lowest achievable RMSED occurs at the calculated switching tilt angle (ϕ_S).

2.5.4 Achievable Accuracy

In this section we assume that $\Delta H = 0$ in order to calculate the RMSED achieved from calculable parameter, therefore $\Delta H + H = 1500$ mm. Performance improvement of the proposed methods, comparing with conventional method is provided in Table 2.9. In conventional system, which only VLID is used under experimental configuration shown in Table 2.9, provides very rough estimated position as receivable area of 9,025,874 mm². The achievable area is calculated from diameter obtained from section 2.5.2, which is equal as 3,390 mm. In the proposed system, by incorporating Azimuth angulations obtained from 6-axis sensor without utilizing any proposed scheme, the estimated position can be narrowed down from achievable area into receivable range of 1,695 mm.

The proposed estimation scheme, SwERP, we include not only Azimuth angulations but also additional information such as the effects of channel DC gains, tilt angulations and receiver's FOV into calculation, of which create 3 ERP. The comparisons on achievable accuracy between the proposed scheme and GOSI that include and exclude Azimuth error are presented in Fig. 2.31 and Table 2.9. In GOSI under 3 receiver's FOV configurations provides the lowest achievable RMSED in the range of 349 and 629 mm. If we assume that
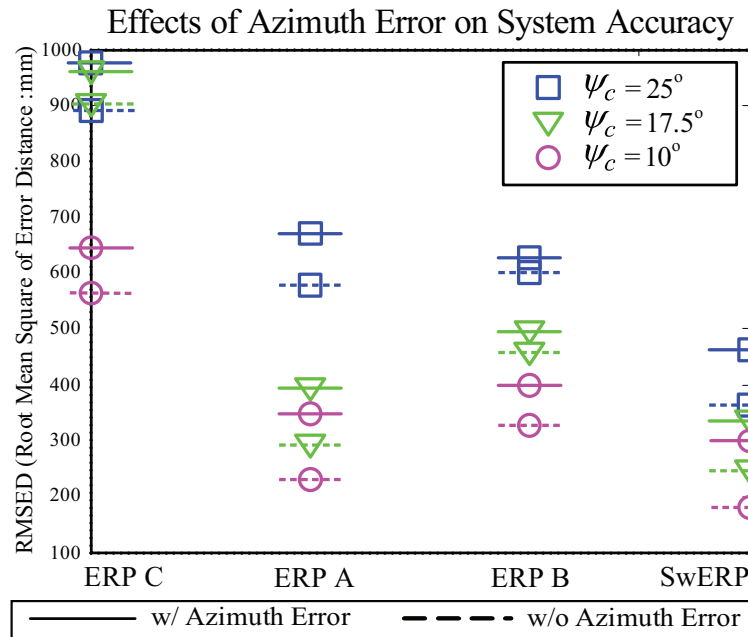
Figure 2.31: Effect of Azimuth angulations error on achievable RMSED of each positioning scheme (ψ_c =25, 17.5, 10 degree).

Azimuth angulations error can be reduced, the achievable RMSED can be reduced to the range of 231 and 577 mm. The results show that ERP A provides lowest RMSED in most of the experimental cases, except for the $\psi_c = 25^o$ where ERP B provides the lowest RMSED; as a result of sensitivity limit. As mentioned in section 2.5.3, sensitivity limit created the effect that make estimated error distances of each ERP vary in proportion to receivers' tilt angle. Therefore, the utilization of plural ERP scheme is proposed to solve this problem.

The proposed scheme, SwERP, utilizes plural ERPs, where the selected ERP is switched between ERP A and ERP B at switching angle (ϕ_S). The contributions of this scheme are the decrease in dependency between estimated error distances and tilt angle, and the highest estimated error distances are limited at switching angle. Hence, lower RMSED can be achieved. In our evaluation, utilizing SwERP scheme provided the lowest achievable accuracy in the range of 298 and 463 mm through all FOV configurations. If we assume that Azimuth angulations error can be reduced, the achievable RMSED can be reduced down to the range of 231 and 577 mm. To sum up, SwERP schemes show the accuracy improvement over conventional, in the range of 72.68 % and 82.42 % depending on receivers' FOV configurations.

After analyzing the statistical data of error distance, we plot the performance of the three experimental configurations, both with and without Azimuth angulations error (β_{Err}),
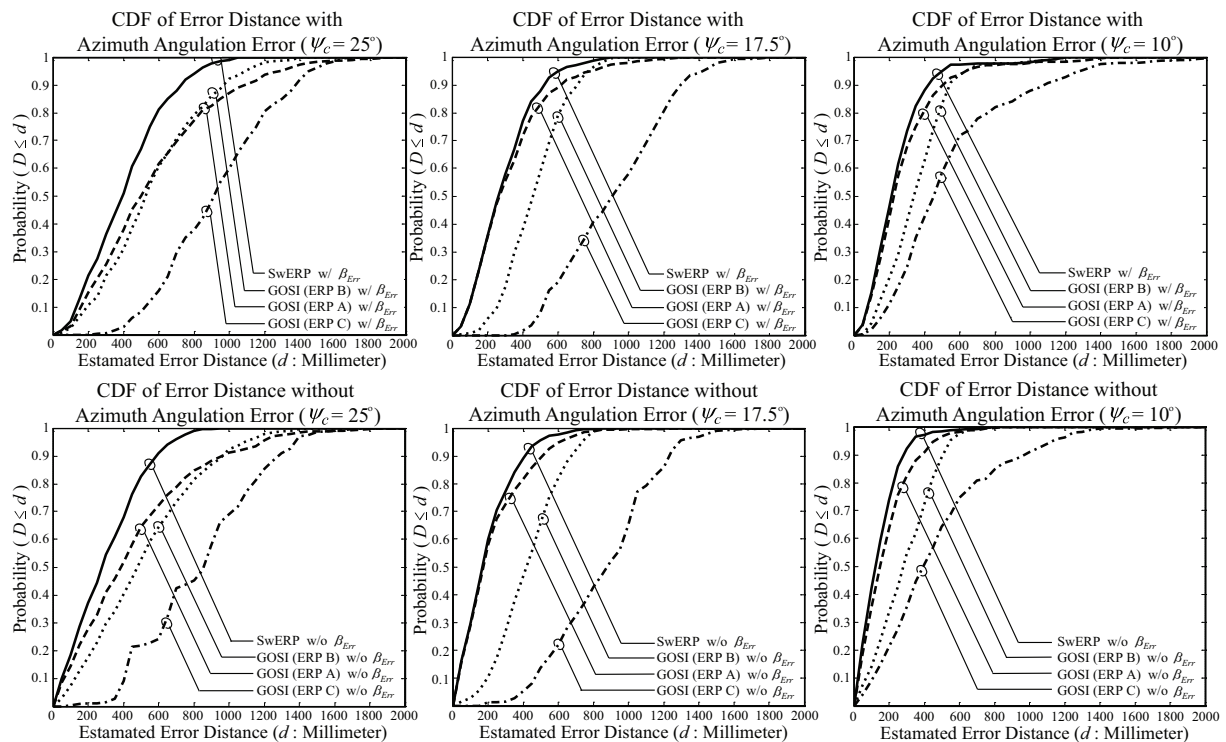
Figure 2.32: Cumulative distribution function of error distance from receiver's $\psi_c = 25$, 17.5 and 10 degree configuration.

using the error distance distribution as CDF in Fig. 2.32. The results confirm that SwERP provided higher accuracy improvement, particularly on wider FOV configuration, like the result provided in Fig. 2.32. Besides, reducing Azimuth angulations error, which is the characteristic of the embedded sensor, higher accuracy can be achieved. We analyze the precision performance at 90 % and 95 % of error distance, the details are provided in Table 2.10. In 90 % precision achieved from GOSI provided accuracy in the range of 503.8 and 968.7 mm, on different configurations. SwERP scheme provides accuracy in the range of 421.1 and 752.0 mm for 90 % precision. So as 90 % precision, SwERP scheme provides lower RMSED than GOSI, of which in the range of 500.1 and 820.1 mm for 95 % precision. Hypothetically, reducing Azimuth angulations can reduce error distance down to the range of 331.5 and 672.5 mm.

2.5.5 Uncertainty of Terminal's height (ΔH)

In the proposed system, only 6-axis sensor is embedded at the receiver. Vertical height (H) is calculated from preconfigured terminal's height (H_T) and broadcasted room height (H_R), which is transmitted via VLID. Due to the limited information, H cannot be precisely
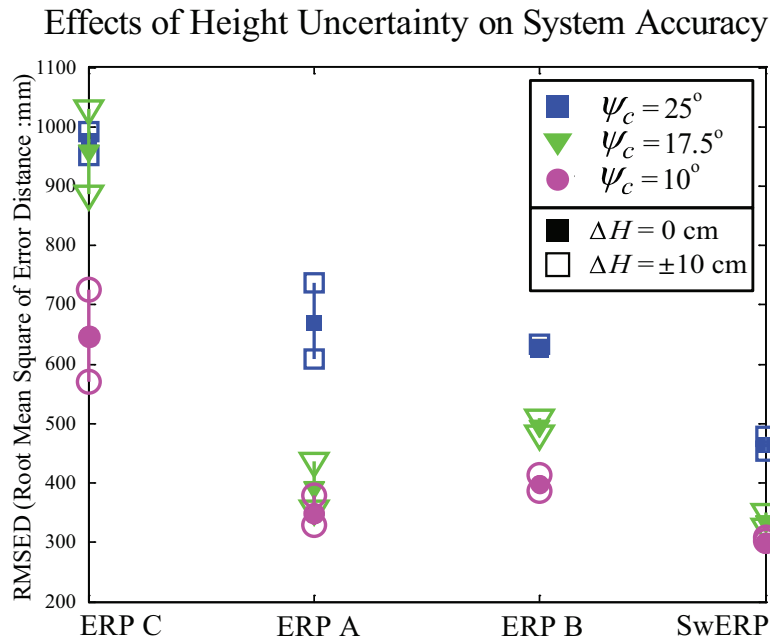
Figure 2.33: Effect of terminals height uncertainty on achievable RMSED of each positioning scheme $\psi_c = 25$, 17.5 and 10 degree configuration.

calculated and can be varied from to the posture of each user. The impact of H is evaluated in this section. From the observation during our experiment, we found out that our H_T is varied around ± 10 cm from the preconfigured value. In this evaluation, we used the experimental data from section 2.3. Thus, β_{Err} is included in the evaluation.

Fig. 2.33 shows the confidence interval of achievable RMSED created from ΔH of GOSI and SwERP schemes. The solid markers represent RMSED calculated from $H = 1500$ mm, and the hollow markers are calculated from $\Delta H + H = 1500 \pm 100$ mm. The results confirm that the proposed SwERP scheme provides lower RMSED with smaller confidence interval than GOSI. SwERP improves not only positioning accuracy but also the system reliability.

2.6 Conclusion

In this chapter, we discuss the design and implementation method of our proposed solution architect for lifetime evolution indoor positioning system based on visible light communication identification (VLID) system. In the approach, neither additional infrastructure nor modification is required on the transmitter side. In contrast, we install 6-axis sensor to provide tilt and Azimuth angulations for positioning estimation. From our study, we define FOV (ψ_c) Limit and Sensitivity ($R_X S$) Limit to justify the characteristic of the system after

embedding 6-axis sensor at the receiver.

Apart from basic infrastructure, we proposed a Switching estimated receiver position (SwERP) scheme based on FOV and sensitivity limits. The proposed scheme provides remarkable accuracy improvement and higher reliability than the case that embedding 6-axis sensor without utilizing any positioning scheme or GOSI. The results are confirmed by both analytical and numerical analysis, 440 experimental samples of 3 receiver's FOV configuration are collected in the area of $1200 \times 5000 \times 2050$ mm. Root mean square of error distance (RMSED) and cumulative distribution function (CDF) of error distance are used as performance indicator.

Main advantages of the proposed architecture are described as follows. Firstly, the proposed system utilizes existing infrastructure, neither modification nor additional infrastructure is required at the transmitter side. Thus, any new kind of investment can be avoided. Secondly, the system is eco-friendly, for the reason that no additional carbon footprint is created during construction, and VLC uses LED that consumes less energy during operation. Thirdly, accuracy achieved in the proposed system does not depend on transmitter orientation since only one transmitter is required for positioning estimation. Fourthly, both of the proposed positioning schemes use low complexity algorithm that can be implemented on portable device such as mobile phone.

Last but not the least, our investigation experimental results confirm that under conventional VLC narrower receiver's FOV can provide higher accuracy but communication accessibility is also limited owing to the FOV configuration. In our proposed scheme, SwERP that based on sensitivity limit, even wide FOV configuration can provide high accuracy. Thus, both accessibility and localization can achieve in the wide receiver's FOV configuration.

Chapter 3

Enhancement Modules for VLC Based Positioning Subsystem

In this chapter, we discuss the proposed enhancement modules for our proposed VLC based positioning subsystem, of which are required to enable SwERP scheme. As mention in section 2.4 that SwERP scheme is performed based on prior information of the closest transmitter and FOV limit required. Thus, we proposed two subsystems to enable the proposed SwERP scheme, which are nearest transmitter classification (NTC) method and physical layer simulation model based on FOV limit classification, respectively.

3.1   Nearest Transmitter Classification (NTC) Method

Nearest transmitter information is a mandatory requirement for utilizing Switching Estimated Receiver Position (SwERP) scheme, of which was proposed to enhance accuracy of Visible Light ID (VLID) positioning system. The conventional approach is achieved by controlling Sensitivity (R_xS) limit. Conversely, general distance estimation by optical received power can also be used. Both of the mentioned methods have disadvantage on implementation complexity and inaccuracy due to noise fluctuation, respectively. In this paper, we propose a nearest transmitter classification (NTC) method by utilizing Optical Orthogonal Code (OOC) with On-Off Keying (OOK) modulation at transmitters (T_xs), and perform oversampling at a receiver (R_x) to overcome the limitation of bandwidth resolution ($\mathcal{B}$). The results confirm that the proposed method can classify the nearest T_x accurately, with some tradeoff with computation complexity from the increment of oversampling factor (O_c).

3.1.1 Received Optical Power Based NTC (NTC_{OP}) Method

The NTC_{OP} classifies the nearest T_x based on received optical power. The optical received power of VLC system is shown in Fig. 2.12, and (2.12), which are modified from [24][40]

$$P_{r,k} = P_{t,k}H_{d,k}(0) + \underbrace{\int_{walls} P_{t,k}dH_{ref,k}(0) + N}_{\xi_k:\text{ Error}},$$

(3.1)

$P_{t,k}$ is the transmitted optical power and N denotes the noise. Hearafter, all the parameters with $(\cdot)_k$ denotes the index number of T_x ranging from 1 to N_T. $P_{r,k}$ is the received optical power calculated from line-of-sight (LOS) path ($H_{d,k}(0)$) and reflected paths ($dH_{ref,k}(0)$). We define $dH_{ref,k}(0)$ and N as error function (ξ_k), which represent undesirable value. Time domain of (3.1) can be expressed as

$$\underbrace{\frac{1}{2T}\int_{-T}^{T} y_k(t)dt}_{P_r^k \geqslant} = \underbrace{\frac{1}{2T}\int_{-T}^{T} (x_k(t) \otimes h_k(t)) + n_k(t)\,dt}_{P_t^k H_d^k(0) + \xi_k \geqslant},$$

(3.2)

where $x_k(t) \geqslant 0$ and $y_k(t)$ are transmitted and received optical pulse power, respectively. $n_k(t)$ represents Additive Gaussian White Noise (AGWN), $h_k(t)$ is the wireless optical channel that has both direct and reflected path. "$\otimes$" denotes convolution and $\lim T \to \infty$.

The method used in NTC_{OP} is similar to the method used in received signal strength indication (RSSI) [44], which estimated distances among $T_x s$ and R_x solely based on LOS path. Detail of the NTC_{OP} can be expressed as the following equations.

$$H_{d,k}(0) = \begin{cases} \dfrac{(m+1)A}{2\pi(D_{PL,k})^2} \cdot \underbrace{\cos^m(\varphi_k)T_s(\psi_k)g(\psi_k)\cos(\psi_k)}_{\Theta_k}, \\ \qquad 0 \leqslant \psi_k \leqslant \psi_c, \\ \qquad\quad 0, \\ \qquad\quad \psi_k > \psi_c, \end{cases}$$

(3.3)

$$D_{PL,k} = \begin{cases} \sqrt{\dfrac{(m+1)A}{2\pi} \cdot \dfrac{P_{t,k}}{P_{r,k} + \xi_k} \cdot \Theta_k}, & 0 \leqslant \psi_k \leqslant \psi_c, \\ +\infty, & \psi_k > \psi_c, \end{cases}$$

(3.4)

$$NTC_{OP} = \min[D_{PL,1}, D_{PL,2}, ..., D_{PL,N_T}],$$

(3.5)

where A is the physical area of the optical concentrator. $D_{PL,k}$ is the estimated distance between a $T_{x,k}$ and R_x, ψ_k is the angle of incidence, $T_s(\psi_k)$ is the gain of an optical filter, $m = -\ln 2/(\ln\cos\Phi_{1/2})$, and $\Phi_{1/2}$ is the semi-angle of transmitter. φ_k is an angle of irradiance

calculated from $\tan^{-1}(D/H)$ as shown in Fig. 2.11. The optical concentrator $g(\psi)$ is given as

$$
g\left(\psi\right) = \begin{cases} \dfrac{n^2}{\sin^2 \psi_c}, & 0 \leq \psi \leq \psi_c, \\ 0, & \psi > \psi_c. \end{cases}
\tag{3.6}
$$

ψ_c denotes the receiver's semi FOV. NTC_{OP} select D_{PL}^k that has the lowest value.

Interference from noise and reflected path can directly degraded accuracy of the conventional NTC_{OP}. The channel DC gain of the first reflection is [29]

$$
H_{ref}\left(0\right) = \begin{cases} \dfrac{(m+1)A}{2\pi^2 D_{1,k}^2 D_{2,k}^2} \rho dA_{wall} \cos^m\left(\varphi'\right) \cos\left(\alpha'\right) \\ \qquad \cos\left(\delta'\right) T_S\left(\psi\right) g\left(\psi'\right) \cos\left(\psi'\right), \\ \qquad\qquad 0 \leq \psi' \leq \psi_c, \\ \qquad\qquad 0, \\ \qquad\qquad \psi' > \psi_c, \end{cases}
\tag{3.7}
$$

where $D_{1,k}$ and $D_{2,k}$ are the distance between $T_{x,k}$ and reflective point (ref), and distance between ref and R_x. ρ is the reflectance factor, dA_{wall} is a reflective area of small region. α' and δ' are the angle of irradiance to ref, and the angle of irradiance to the receiver, respectively (Fig. 2.11). However the spreading gain of OOC code can mitigate the interference from noise and reflected path.

3.1.2 Optical Orthogonal Code (OOC)

VLC uses LED light bulbs, which are incoherent light sources, as T_x. Therefore, we use one dimensional OOK-OOC, which is the simplest form of Incoherent Optical Codec [30]. The OOC codeword is $(0,1) -$ sequences represented by $C = (n, w, \lambda_a, \lambda_c)$. n and w denote code length and number of '1', in each codeword, respectively. Autocorrelation of each codeword $X = (x_0, x_1, \cdots, x_{n-1})$ and cross-correlation between two distinct codewords X and Y, where $Y = (y_0, y_1, \cdots, y_{n-1})$, satisfy the following properties respectively [30][45].

$$
\left. \begin{aligned} \theta_{XX}\left(\tau\right) &= \sum_{i=0}^{n-1} x_i \cdot x_{i \oplus \tau} = \begin{cases} w, & \tau = 0, \\ \leqslant \lambda_a, & 1 \leqslant \tau \leqslant n-1, \end{cases} \\ \theta_{XY}\left(\tau\right) &= \sum_{i=0}^{n-1} x_i \cdot y_{i \oplus \tau} \leqslant \lambda_c, \qquad 0 \leqslant \tau \leqslant n-1 \end{aligned} \right\},
\tag{3.8}
$$

for $x_i, y_i \in \{0,1\}, \tau \neq 0, X \neq Y, \lambda_a = \lambda_c = \lambda$ and "$\oplus$" denotes modulo$-n$ addition. Thus, the largest possible cardinality is denoted as $|C|_{\max} = \Phi\left(n, w, \lambda\right)$. The C is said to be

Table 3.1: Codeword Sets of an Optimal $(341,5,1)-$Code [45]

S_1	0	1	85	21	5	S_{10}	0	17	264	203	165
S_2	0	2	170	10	42	S_{11}	0	19	88	267	220
S_3	0	3	111	104	53	S_{12}	0	22	90	55	152
S_4	0	6	222	106	208	S_{13}	0	23	293	252	118
S_5	0	9	268	151	105	S_{14}	0	24	206	83	150
S_6	0	11	45	76	198	S_{15}	0	25	54	169	221
S_7	0	12	103	75	212	S_{16}	0	26	269	86	113
S_8	0	13	305	227	43	S_{17}	0	37	147	217	81
S_9	0	15	107	146	164						

OOC$-$optimized when

$$|C| = \left\lfloor \frac{1}{w} \left\lfloor \frac{(n-1)}{(w-1)} \left\lfloor \cdots \left\lfloor \frac{(n-\lambda)}{(w-\lambda)} \right\rfloor \cdots \right\rfloor \right\rfloor \right\rfloor. \qquad (3.9)$$

In this research we use OOC which has combination of $n = 314, w = 5, \lambda = 1$, which provide $|C| = 17$. We use finite projective geometry to construct the code words [30][45].

The finite projective geometry $PG(d, q)$ is represented by a finite vector space as $V(d+1, q)$, where $d+1$ denotes the vectors dimension and q is a prime power of the finite $GF(q)$. There are $\left(q^{d+1} - 1\right) / (q - 1)$ points (n) in $PG(d, q)$, so as different lines in $V(d+1, q)$. Regarding projective geometry theorem, two codewords will intersect at no more than one point. Discrete logarithm is used to provide cyclic shift on the points of geometry.

Define ϑ as a vector in the space $V(d+1, q)$, and α is a primitive element of $GF(q^{d+1})$ which has the nonzero elements of oth through the $(q^{d+1}-2)^{\text{th}}$. Thus, the relationship between α and ϑ is defined as $\log_\alpha \vartheta = \gamma$, where γ is the $o-$th power of α. For an arbitrary point p in $PG(d, q)$, let $\log p$ denote the discrete logarithm of any vector on the line corresponding to p in $V(d+1, q)$ modulo$-n$ as in

$$\log p = 1 + \log p' \,(\text{mod } n), \qquad (3.10)$$

for the cyclic shift of some point p' on the same line as p.

In projective geometery the cyclic shift of a line is still a line in $PG(d, q)$. An orbit size of lines in $PG(d, q)$ is its size (n), of which $n = \left(q^{d+1} - 1\right) / (q - 1)$ and $w = q + 1$. The codewords of $C(314, 5, 1)$ can be obtained from Table 3.1, the reason for using these codewords is described in section 3.1.3.

Modeling of One-Dimensional OOC

We assume the evaluation situation is similar to that in [46] where all of T_xs are simultaneously broadcast to R_x. At any instantaneous time R_x receives signal from T_x of $1 \leqslant k \leqslant N_T$.

The light sources in the system are all incoherent. Therefore, the intensities of light signals that occur simultaneously are additive. Under mentioned assumption, the encoded signal from T_x of the $k-$th T_x is

$$x_k(t) = \mathcal{P}_k \cdot s_k(t) c_k(t), \tag{3.11}$$

where $\mathcal{P}_k, s_k(t)$ and $c_k(t)$ represent the kth of T_x's transmitted optical power, binary data signal, and $|C|$ for $1 \leqslant k \leqslant N_T$, respectively

$$s_k(t) = \sum_{m=-\infty}^{\infty} s_{m,k} \sqcap_{\tau_s} (t - m\tau_s), \tag{3.12}$$

$$c_k(t) = \sum_{l=-\infty}^{\infty} c_{l,k} \sqcap_{\tau_c} (t - l\tau_c), \tag{3.13}$$

where $s_{m,k}$ and $c_{l,k}$ are $m-$th bit of data and code $l-$th of $k-$th T_x. $\sqcap_{\tau_s}(t)$ and $\sqcap_{\tau_c}(t)$ indicate the rectangular pulse of duration τ_s and τ_c, which start at $t = 0$, respectively. The relationship between τ_s and τ_c is $\tau_c = \tau_s/n$, where τ_s is bit interval of data, τ_c is chip interval, and n is OOC codelength. The received optical signal at R_x is denoted by $y(t)$, where $y(t) = \sum_{k=1}^{N_T} y_k(t)$ and $y_k(t)$ is explained in (3.2).

Thus, the output of the first T_x can be expressed by [46]

$$z_1 = \frac{1}{\tau_c} \int_0^{\tau_s} y(t) c_1(t) dt \gtrless T_h \tag{3.14}$$

where the received optical pulse $y(t)$ is multiplied by the correct codeword $c_1(t)$ and sampled output of both the optical correlator and its equivalent matched filter at time $t = \tau_s$. Thus, the sampled signal is compared with threshold T_h, to decide whether the output is '0' or '1'.

3.1.3   System Description

The proposed method is based on the system model shown in [29]. Apart from introducing OOC-OOK to enable the proposed NTC_{OC}, at the R_x oversampling is performed in order to enhance the distance resolution ($\Delta \mathcal{D}_L$) of VLC channel, as shown in Fig. 1.13. We choose OOC ahead of other incoherent optical code division multiple access (OCDMA) codes for the following reasons. Firstly, OOC provided high bandwidth efficiency. Secondly, OOC possesses the ideal auto- and cross-correlations [45], which is the key driver in our proposed method.

Simulation Environment

Simulation area consists of a grid 18 transmitters, with grid size of 1 m × 1 m in room area of 6 m × 12 m × 3 m. Details of simulation can be found in Table 3.2, Fig. 3.1, and Fig. 3.2, where receivers are uniformly distributed along x and y axis. Each T_x transmits its own location ID ranging from '00001' to '10010'. OOC-OOK is implemented at the T_x as VLC modulator, each T_x is assigned to a OOC code. We assumed that all of the transmitters are

Table 3.2: Simulation Parameters I

Parameters	Quantity
Environment	6 m × 12 m × 3 m
Transmitter $(T_x : N_T)$	18
Transmitter's Height (h)	1.5 m
Receiver $(R_x : N_R)$	10,000 Trials
OOC Codewords $(C(n, w, 1))$	$C(314, 5, 1)$
Chip rate (r_c)	34.1 Mbps
T_x's Half-Power Angle $(\Phi_{1/2})$	50 Degree
Semi FOV (ψ_c)	50 Degree
Number of Reflection	0 Time
Tilt Angulation's (ϕ)	0 Degree

synchronized via PLC as reported in [47][48]. We define state '0' of the modulated signal as ON, and state '1' as OFF. We use $C(314, 5, 1)$ codewords, because it is the shortest optimal code length that can provide number of codewords very close to N_T in our evaluation. The details of NTC_{OC} method, and necessity of oversampling unit at R_x are presented in the next section.

Transmitter Signal to Noise Ratio : TSNR

Noise and reflection can degrade estimated $D_{PL,k}$ mentioned in (3.4). VLC uses illumination to transmit information; illumination design is another sophisticate field of study that deals with deliberating application of light to achieve some artistic or practical effect. Therefore, in this subsystem we use, TSNR instead of general SNR in order to study the NTCs performance in various type of illumination intensity. In this section, we discuss TSNR which is the ratio of signal power to the noise power distorting the signal [24], we model noise our system as

$$TSNR_{dB} = 10 \log \left(\frac{P_t}{\sigma_{Total}} \right)^2, \tag{3.15}$$

we define noise (σ_{Total}) as composites of thermal noise (σ_{Th}), and shot noise (σ_{St}). Definition of each term is provided as

$$P_t = \lim_{T \to \infty} \frac{1}{2T} \int_{-T}^{T} \left(\sum_{k=1}^{N_T} x_k(t) \otimes h_k(t) \right) dt, \tag{3.16}$$

where $x_k(t)$ is OOC encoded signal described in (3.11). Variance of shot noise is given as

$$\sigma_{St} = 2q P_r B_N + 2q I_{bg} I_2 B_N, \tag{3.17}$$
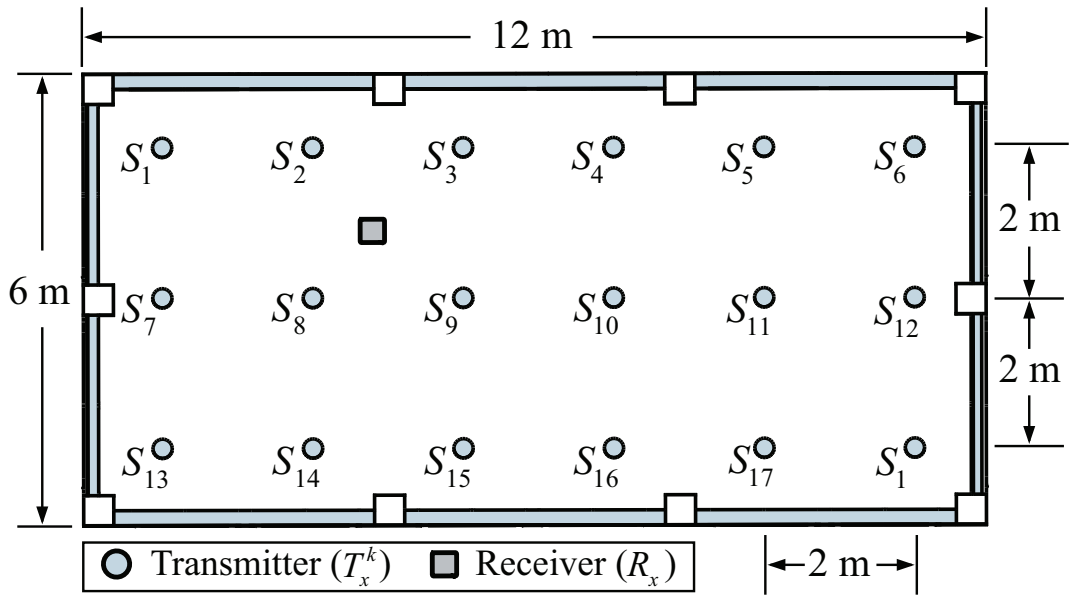
Figure 3.1: Block diagram of the modified VLC transceiver for the proposed NTC method.
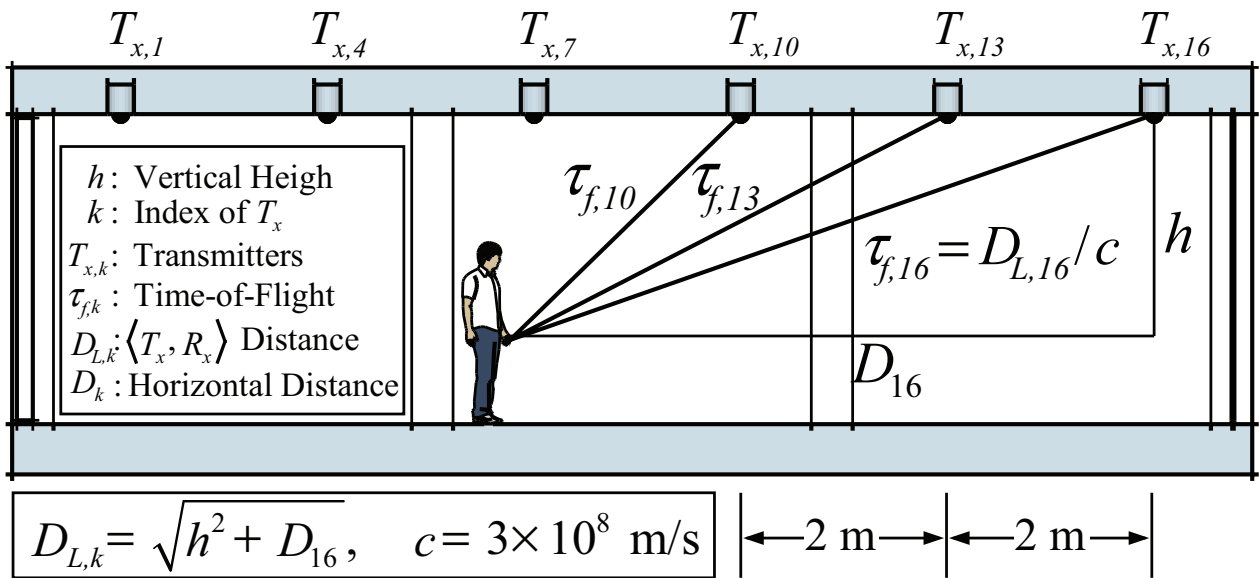
Figure 3.2: Simulation environment with the dimension of 6 m $\times$ 12 m $\times$ 3 m.

Table 3.3: Simulation Parameters II [24]

Open-loop Voltage Gain (G)	10
Fixed Capacitance (η)	112 pF/cm^2
FET Channel Noise Factor (Γ)	1.5
FET Transconductance (g_m)	30 ms
Absolute Temperature (T_κ)	298 K
Background Light Current (I_g)	$\sim$5100 μA
Chip Rate (r_c)	34.1 Mcps

where q is the electronic charge, B_N is equivalent noise bandwidth, I_{bg} is background current and we assume the background current from [49]. The noise bandwidth factors $I_2 = 0.562$. The thermal noise variance is

$$\sigma_{Th} = \frac{8\pi\kappa T_\kappa}{G}\eta A I_2 B_N^2 + \frac{16\pi^2\kappa T_\kappa\Gamma}{g_m}\eta^2 A^2 I_3 B_N^2, \qquad (3.18)$$

where Boltzmann's constant is denoted by κ, T_κ is absolute temperature, G is the open-loop voltage gain, η is the fixed capacitance of photodetector per unit area, Γ is the FET channel noise factor, g_m is the FET transconductance, and $I_3 = 0.0868$. The parameters in (3.17) and (3.18) are obtained from [24], and provided in Table 3.3.

3.1.4 Proposed OOC Based NTC (NTC_{OC}) Method

The principle of NTC_{OC} method is based on Time-of-Arrival (TOA) technique [44]. Distances in TOA are measured from time difference between $T_{x,k}$ and R_x as $c \cdot (\tau_k - \tau_0) = (D_{L,k} \pm \Delta\mathcal{D}_L)$. τ_k and τ_0 are time measured at R_x and $T_{x,k}$, respectively. $D_{L,k}$ is the actual distance between $\langle T_{x,k}, R_x \rangle$, $\Delta\mathcal{D}_L$ is one-way distance resolution, and c is light speed (3×10^8 m/s). The accuracy of TOA depends on $\Delta\mathcal{D}_L$, accurateness of τ measurement shown in Fig. 3.3, and is varied by time resolution (τ_{clk}) and bandwidth resolution ($\mathcal{B}$).

Bandwidth Resolution ($\mathcal{B}$)

In general TOA system, $\mathcal{B}$ decides the estimation accuracy [44]. Assume we want distance accuracy in the range of 30 cm. Thus, at least $(3 \times 10^{-1}$ m$/3 \times 10^8$ m/s$) = 1$ ns must be achieved. A rule of thumb, $\mathcal{B} = 1/(1$ ns$) = 1$ GHz, which is much higher than the current achievable chip rate ($r_c = 1/\tau_c = 200$ Mcps) for LED light bulb [50]. Therefore, we propose a novel method using OOC and perform oversampling at the R_x that can overcome the limitation of $\mathcal{B}$.
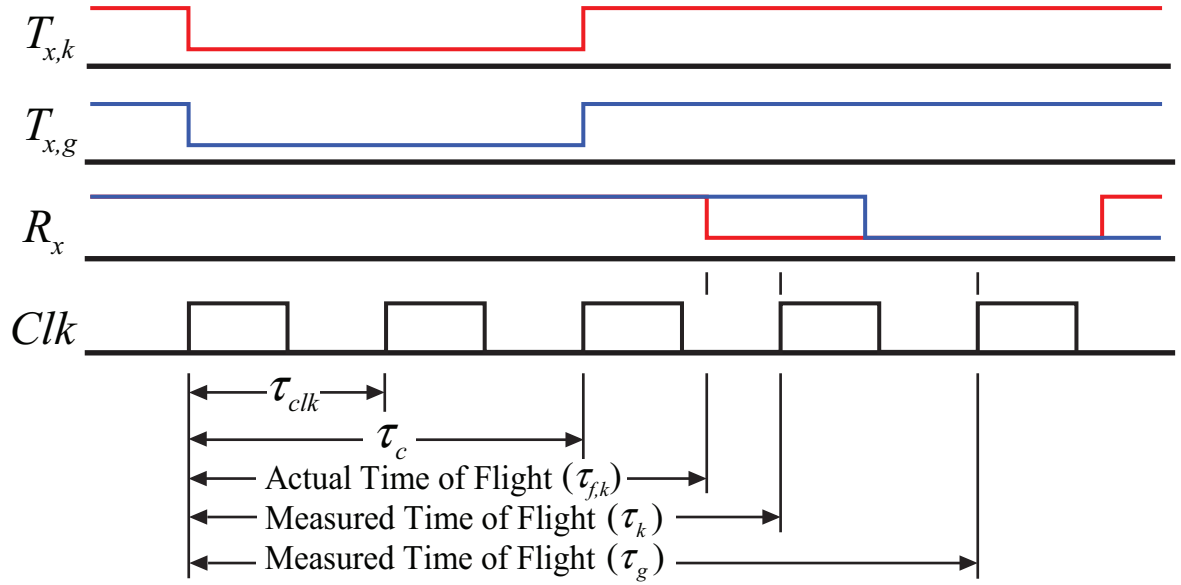
Figure 3.3: Time resolution (τ_{clk}) and its relationship with Time-of-Flight (τ_f^k).

Oversampling ($\uparrow \tau_{clk}$)

Generally, oversampling is being implemented for noise cancellation. In this subsystem, we took advantage of its necessity to yield the $\mathcal{B}$ limitation by utilizing the oversampling together with orthogonality of OOC to enhance time resolution (τ_{clk}). The achievable $\Delta\mathcal{D}_L$ of OOC encoded signal after oversampling is

$$\Delta\mathcal{D}_L = c/\left(2 \cdot r_c O_c\right) \tag{3.19}$$

where O_c is the oversampling factor. The conventional VLID system [28] is a low bit rate system, for the ease of calculation we assume that $r_c = 34.1$ Mcps. Hence, the transmitted data rate is equal to 100 kbps/T_x, of which is higher than that in [28]. Thus, the achievable $\Delta\mathcal{D}_L = (3 \times 10^8$ m/s$)\times(1/(68.2 \cdot O_c \times 10^6)$ s$) = 4.40/O_c$ m. For desired $\Delta\mathcal{D}_L$ of 30 cm, at least $O_c = 15$ is required.

Methodology

As mentioned in system description, we assume communication among T_xs are synchronous [47][48], and communication between T_xs and, R_x are asynchronous. Therefore, for the ease of evaluation, synchronization frame of IEEE 802.11 short preamble, of which has 56 '1's, are transmitted from T_xs for synchronization. The NTC_{OC} method classifies the T_x based on auto-correlation in (3.8) and (3.14), with $r_{clk} = 2r_c \cdot O_c$ at the receiver. Detail of the
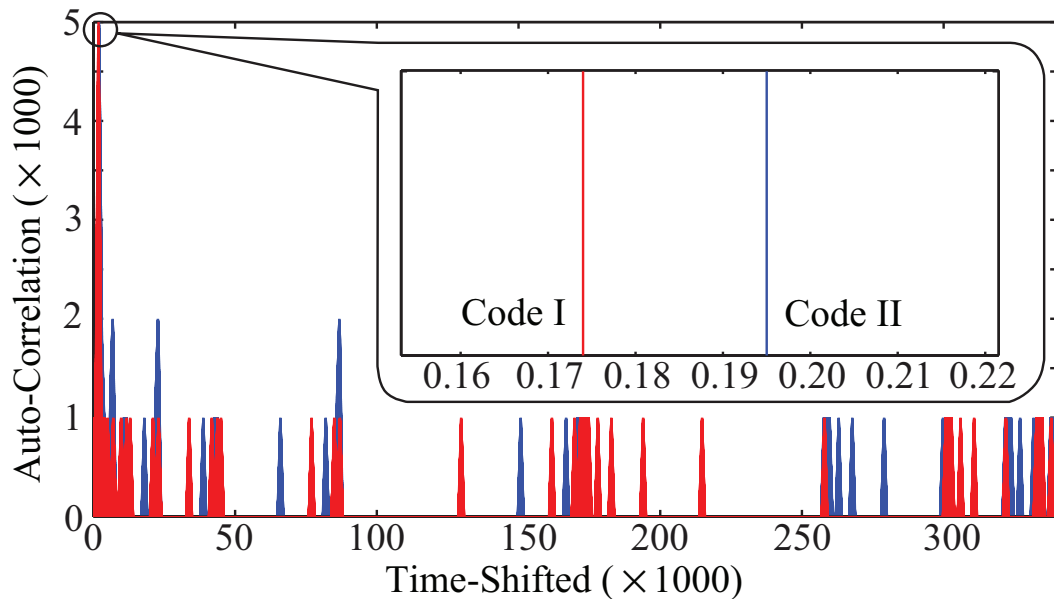
Figure 3.4: An impact of oversampling (O_c) on auto-correlation (θ_{XX}) function.

NTC_{OC} method is provided as

$$NTC_{OC} = \min_{\tau_k; k=1,2,...,N_T} \left[\theta_{XX} \left(\tau_1 \right), ..., \theta_{XX} \left(\tau_k \right) \right] \tag{3.20}$$

where τ_k is the time that provide $\theta_{XX} \left(\tau_k \right) = \left(w \cdot O_c \right)$, and w is OOC-codeweight. The proposed NTC_{OC} method selects the lowest τ from $k-$th T_x of the synchronization frame.

3.1.5 Performance Evaluation

In this section we discuss the effectiveness of the proposed NTC_{OC} by analyzing oversampling effects on the enhance classification rate over the conventional NTC_{OP}. Figure 3.4 shows sampling clock rate of 1000 time over τ_c. The result shows that auto-correlation peak can be correctly separable owing to the enhanced time resolution from oversampling. Nevertheless, computation complexity of auto-correlation function regarding (3.23) is increasing by factor of O_c^2. Therefore, optimized value of O_c that can enhance correct NTC classification is studied.

Figure 3.5 shows simulation result of the relationship between O_c and the nearest T_x correctly classified, in our studied environment. The result shows that with $O_c(10) = 10$, 80 % of nearest T_x correctly classified can be achieved. There is 70 % improvement between $O_c(10) = 10$ and $O_c(5) = 5$ with the computation increased by $O_c^2(10)/O_c^2(5) = 100/25 = 4$ times. The correctness of 90 % can be achieved with $O_c(50) = 50$ which require
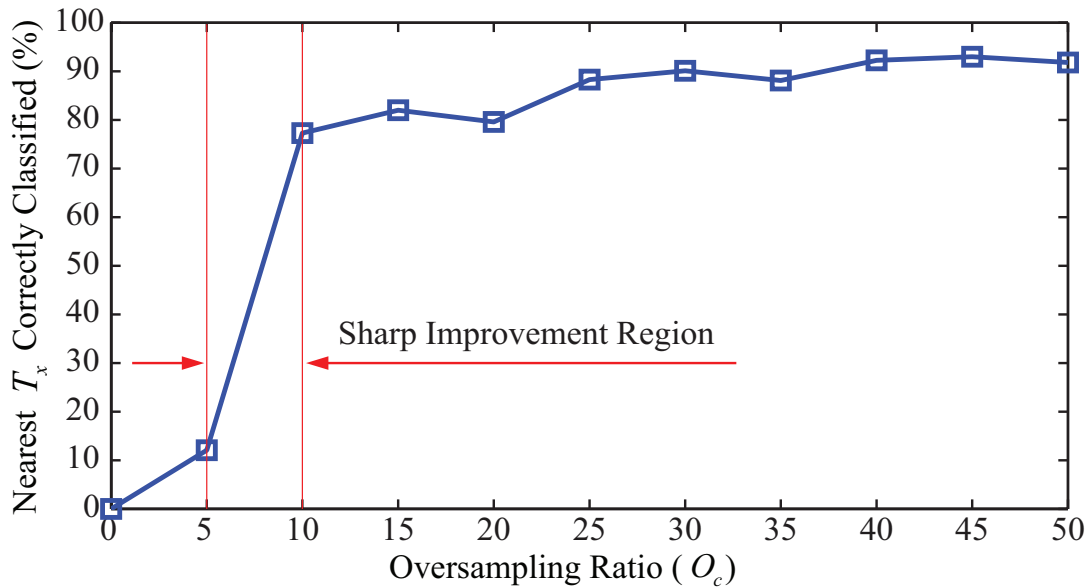
Figure 3.5: An illustration of oversampling ratio (O_c) and correctly classified nearest T_x.
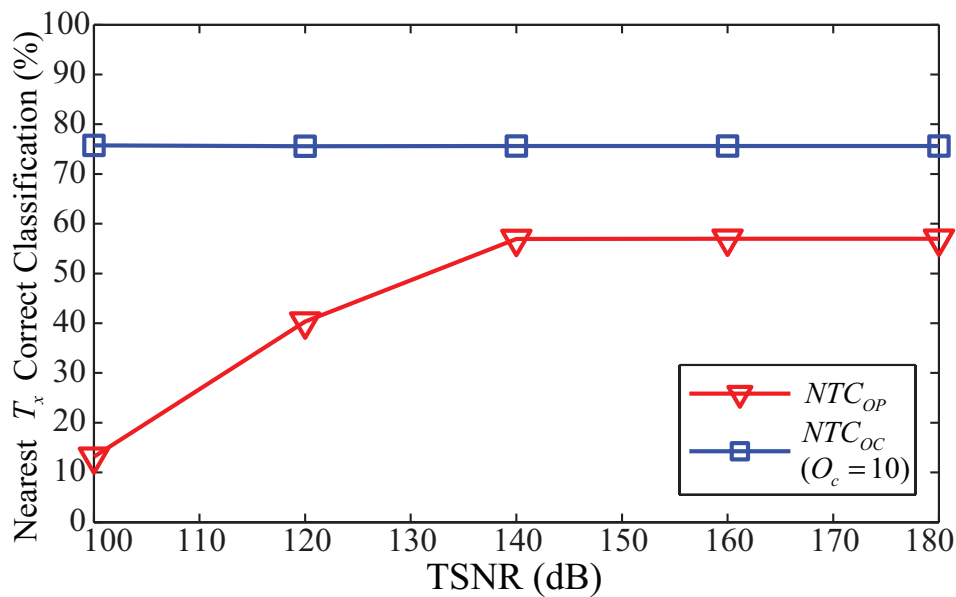
Figure 3.6: Performance of NTC_{OC} and NTC_{OP} in different TSNRs.

$O_c^2(50)/O_c^2(5) = 2500/25 = 100$ times higher computation than $O_c(5) = 5$. Therefore, we use $O_c(10) = 10$ which is the optimal value for the further evaluation.

The effectiveness of NTC_{OC} is shown in Fig. 3.6, where $x-$axis shows transmitter signal

to noise ratio and $y-$axis shows nearest T_x correct classification rate. The higest acheivable correct classification rate of the conventional NTC_{OP} is close to 60 % and cannot be improved. On the other hand, the highest correct classification rate of the proposed NTC_{OC} is equal to the value presented in Fig. 3.5, which is limited by O_c. The proposed NTC_{OC} provides high correct classification rate and high stability, owing to spreading gain and FOV limit that filter out the neighboring codes.

3.2 Physical Layer Simulation Model

The high positioning accuracy of SwERP scheme is achieved from Sensitivity (R_xS) Limit, Field-of-View (FOV) Limit, and assisted Azimuth and Tilt information from 6-Axis sensor. In this section, we propose a physical simulation model that can predict the latter three factors. The conventional Visible Light Communication (VLC) model uses only geometric optics (GO) to predict light propagation, which is not enough to define the FOV Limit. Thus, we propose a novel method using rotation matrix with cone function and Support Vector Machines (SVMs) to classify the boundary of FOV Limit. Based on Sensitivity and FOV limits, possible Azimuth and Tilt angulations are mathematically defined. Moreover, by including FOV Limit into the simulation, transmitters and their mirrors that are outside FOV Limit can be neglected, of which reduce at least 80 % of computation during GO calculation.

3.2.1 Geometric Optics : GO

Geometric Optics (GO) is a method used for estimating light propagation and its reflected paths for (2.7). We calculate reflection by using mirror image of transmitters as shown in Fig. 2.12. We define $[\cdot]_{\mathbf{MR}}$ as diagonal matrix whose component are mirror positions of walls on North, East, West, and South (NEWS) direction, and $[\cdot]_j^i$ as a $j \times 1$ matrix that only has a component on row i. $Diag(\cdot)$ represents a diagonal matrix.

$$\mathbf{Tx} = \begin{bmatrix} T_x(x) & T_x(y) & T_x(z) \end{bmatrix}^T \tag{3.21}$$

$$\mathbf{R_A} = \begin{bmatrix} R_x(x) & R_x(y) & R_x(z) \end{bmatrix}^T \tag{3.22}$$

$$\mathbf{T_{MR}} = Diag\left(\mathbf{Tx_N}, \mathbf{Tx_E}, \mathbf{Tx_W}, \mathbf{Tx_S}\right)$$

$$\begin{cases} \mathbf{Tx_W} = \mathbf{Tx} - [T_x(x)]_{j=3}^{i=1}, \mathbf{Tx_S} = \mathbf{Tx} - [T_x(y)]_{j=3}^{i=2} \\ \mathbf{Tx_E} = \mathbf{Tx} + [|T_x(x) - X_{\max}| + X_{\max}]_{j=3}^{i=1}, \\ \mathbf{Tx_N} = \mathbf{Tx} + [|T_x(y) - Y_{\max}| + Y_{\max}]_{j=3}^{i=2}, \end{cases} \tag{3.23}$$

$\mathbf{Tx}$ and $\mathbf{R_A}$ matrixes represent Cartesian coordination of a T_x and R_x, respectively. $\mathbf{Tx_N}, \mathbf{Tx_S}, \mathbf{Tx_E}$ and $\mathbf{Tx_W}$ are mirror positions of $\mathbf{Tx}$ calculated from NEWS walls. $Dist(\cdot)$

Table 3.4: Simulation Parameters III

Parameters	Quantity
Environment	6 m × 12 m × 3 m
Transmitter (T_x)	38
Receiver ($R_x : n$)	600,000 Trials
R_x's X-Axis ($R_x(x)$)	$U([0\ 6])$ m
R_x's Y-Axis ($R_x(y)$)	$U([0\ 12])$ m
R_x's Z-Axis ($R_x(z)$)	$1.5 + U([\text{-}0.1\ 0.1])$ m
T_x's Half-Power Angle ($\Phi_{1/2}$)	50 Degree
Semi FOV (ψ_c)	20, 30, 40 Degree
Number of Reflection	1 Time

denotes Euclidean distance. $X_{\max}$ and $Y_{\max}$ are maximum value of x and y axis, respectively as shown in Table 3.4.

Reflection coordinate on each wall can be derived from the following equations

$$\underbrace{\mathbf{R_A^*} + (\mathbf{T_{MR}} - \mathbf{R_A^*})\,\mathbf{T}}_{T_x \text{mirrors to } R_x \text{ line equation}} = \underbrace{\begin{matrix}\mathbf{W_{MR}^{k=0}} \\ +\left(\mathbf{W_{MR}^{k=1}} - \mathbf{W_{MR}^{k=0}}\right)\mathbf{U} \\ +\left(\mathbf{W_{MR}^{k=2}} - \mathbf{W_{MR}^{k=0}}\right)\mathbf{V}\end{matrix}}_{\text{Walls (NEWS) equation}} \quad (3.24)$$

$$\underbrace{\mathbf{R_A^*} - \mathbf{W_{MR}^{k=0}}}_{\mathbf{A}} = \underbrace{\begin{bmatrix}\mathbf{R_A^*} - \mathbf{T_{MR}} \\ \mathbf{W_{MR}^{k=1}} - \mathbf{W_{MR}^{k=0}} \\ \mathbf{W_{MR}^{k=2}} - \mathbf{W_{MR}^{k=0}}\end{bmatrix}^T}_{\mathbf{E}} \begin{bmatrix}\mathbf{T} \\ \mathbf{U} \\ \mathbf{V}\end{bmatrix} \quad (3.25)$$

$$\underbrace{\begin{bmatrix}\mathbf{T} & \mathbf{U} & \mathbf{V}\end{bmatrix}^T}_{\text{Reflection points}} = \mathbf{E^{-1}A} \quad (3.26)$$

We define $\mathbf{R_A^*} = Diag(\mathbf{R_A}, \mathbf{R_A}, \mathbf{R_A}, \mathbf{R_A})$. $\mathbf{T}, \mathbf{U}$ and $\mathbf{V}$ are 4×4 diagonal matrixes that represent eigenvalue of reflection points from wall NEWS, respectively. $\mathbf{W_{MR}^k}$ contains k-th sample of $\mathbf{W_{MR}}$. In (3.24), 3 samples are required to construct each wall equation, thus $k = \{0, 1, 2\}$.

3.2.2 Proposed Method

FOV of VLC receiver can be viewed as cone function. Intersection of a cone and plane define FOV Limit of the system, which create quadratic functions. All of the possible conic sections are illustrated in Fig. 3.7. The conventional conics equation cannot be used, because ERP
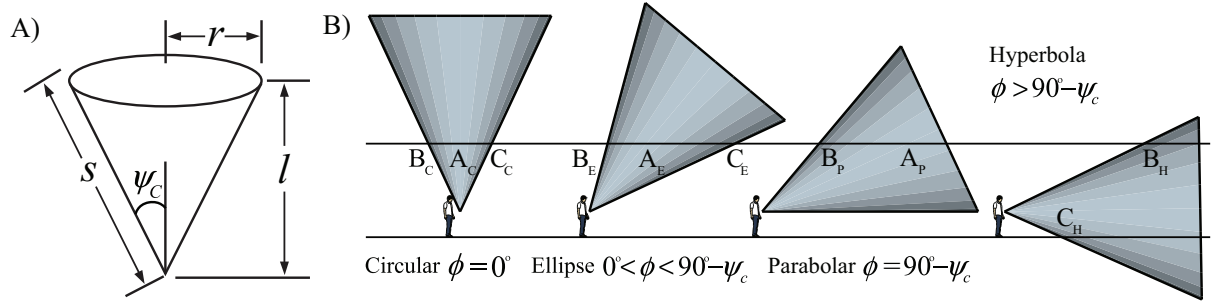
Figure 3.7: An illustration of A) 3D cone function B) All possible conic sections and conditions

A (calculated from ϕ) is undefined. Therefore, we propose a novel method using rotation matrix with cone function and Support Vector Machines (SVMs) to classify the boundary of FOV Limit. Cone function is shown in Fig. 3.7 and (3.27)

$$\mathbf{C} = \begin{bmatrix} X_A \\ Y_A \\ Z_A \end{bmatrix} = \begin{bmatrix} \dfrac{l-u}{l}r\cos(\varpi) & \dfrac{l-u}{l}r\sin(\varpi) & u \end{bmatrix}^T \tag{3.27}$$

for $\psi_c = \tan^{-1}(r/l), u \in [0, l], \varpi \in [0, 2\pi)$ and $l = 15$ m.

3.2.3 Rotation Matrix

Rotation matrix is a matrix that performs a rotation in Euclidean space. Rotation matrix is denoted as $\mathbf{R}$, in our case $\mathbf{R} = \mathbf{R_z}(\beta) \cdot \mathbf{R_x}(\phi)$. The rotated cone function is defined as

$$\mathbf{C_N} = \mathbf{R} \cdot \mathbf{C} + \mathbf{R_A} = \begin{bmatrix} X_B & Y_B & Z_B \end{bmatrix} \tag{3.28}$$

$$\mathbf{R_z}(\beta) = \begin{bmatrix} \cos(\beta) & \sin(\beta) & 0 \\ -\sin(\beta) & \cos(\beta) & 0 \\ 0 & 0 & 1 \end{bmatrix}, \tag{3.29a}$$

$$\mathbf{R_x}(\phi) = \begin{bmatrix} 1 & 0 & 0 \\ 0 & \cos(\phi) & \sin(\phi) \\ 0 & -\sin(\phi) & \cos(\phi) \end{bmatrix}, \tag{3.29b}$$

where $\mathbf{R_z}(\beta)$ and $\mathbf{R_x}(\phi)$ are rotation matrix of Azimuth and Tilt plane, which $\beta \in [0, 2\pi)$ and $\phi \in [0, \pi/2]$. Therefore, $\mathbf{R}$ is denoted as

$$\mathbf{R} = \begin{bmatrix} \cos(\beta) & \sin(\beta)\cos(\phi) & \sin(\beta)\sin(\phi) \\ -\sin(\beta) & \cos(\beta)\cos(\phi) & \cos(\beta)\sin(\phi) \\ 0 & -\sin(\phi) & \cos(\phi) \end{bmatrix}. \tag{3.30}$$

Closed form equation of FOV Limit can be derived by, rewriting Z_B of (3.28) in term of u. Z_B is the height of rotated cone that intersected with plane. Hence, $Z_B = H$ where H is vertical height (Fig. 2.11), and $r = l \cdot \tan(\psi_c)$ for the boundary of cone. FOV Limit matrix is defended as

$$\mathbf{FOV_{Lt}} = \mathbf{R_{2D}} \cdot \mathbf{C} + \mathbf{Rx_{2D}} \tag{3.31}$$

$$\mathbf{Rx_{2D}} = \begin{bmatrix} R_x(x) & R_x(y) \end{bmatrix}^T \tag{3.32}$$

$$u = \frac{lZ_B + l\sin(\phi)r\sin(\varpi)}{l\cos(\phi) + \sin(\phi)r\sin(\varpi)} \tag{3.33}$$

$$\mathbf{R_{2D}} = \begin{bmatrix} \cos(\beta) & \sin(\beta)\cos(\phi) & \sin(\beta)\sin(\phi) \\ -\sin(\beta) & \cos(\beta)\cos(\phi) & \cos(\beta)\sin(\phi) \end{bmatrix} \tag{3.34}$$

3.2.4 Support Vector Machines

Support vector machines (SVMs) are supervised learning methods that use the training algorithm to builds a model that predicts if a new input falls into which category. SVM use training set to create hyperplane between categories of training set. Training set is defined as

$$\mathcal{D} = \{(x_i, y_i) \,|\, x_i \in \mathbb{R}^p, y_i \in \{-1, +1\}\}_{i=1}^n \tag{3.35}$$

$$y_i = \begin{cases} +1, & \text{if } x_i \in \{\mathbf{FOV_{Lt}} | r \in [0, l\tan(\psi_c)]\} \\ -1, & \text{if } x_i \in \{\mathbf{FOV_{Lt}} | r \in (l\tan(\psi_c), \infty)\} \end{cases} \tag{3.36}$$

the x_i is $p-$dimensional real vector with n training samples obtained from $\mathbf{FOV_{Lt}}$. Samples of $y_i = +1$ are values inside the conics, and $y_i = -1$ are values outside the conics. Optimal functional margin (γ) between training sample and hyperplane ($\gamma = \hat{\gamma} / \|w\|$). In order to prevent non-convex constrain, the geometric margin ($\hat{\gamma}$) is rescaled to 1. Hence, problem set is

$$\min_{\gamma, \omega, b} \frac{1}{2} \|w\|^2 \tag{3.37}$$
$$\text{s.t. } y_i\left(w^T \mathcal{K}(x_i, x_j) + b\right) \geqslant 1, \; i, j = 1, \; ..., \; n$$

$$\mathcal{K}(x_i, x_j) = \phi(x_i)^T \phi(x_j) = (1 + x_i x_j)^2 \tag{3.38}$$

(w, b) are weighting factors that determine the offset of hyperplane from the original along the vector w, which is perpendicular to hyperplane. Thus, solving this problem will result in (w, b) with the smallest possible γ with respect to the training set. $\mathcal{K}(x_i, x_j)$ is denoted as Quadratic Kernel function, which is used to map observations from inner product of (x_i, x_j)
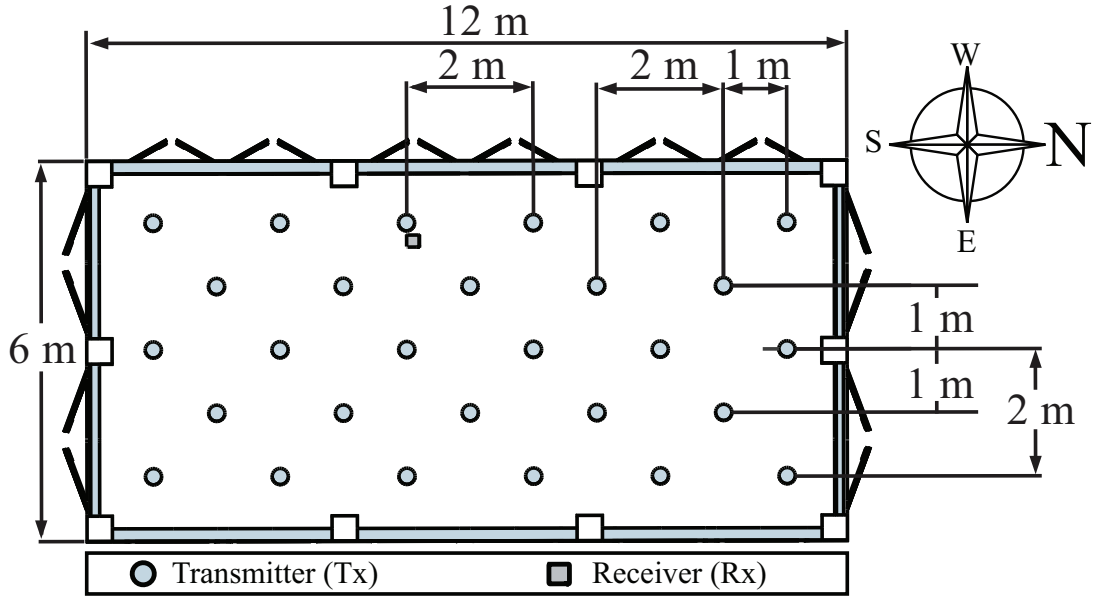
Figure 3.8: an illustration of simulation environment with the dimension of 6 m $\times$ 12 m $\times$ 3 m.

into $(\phi(x_i), \phi(x_j))$ in order to gain linear structure.

$$
\begin{aligned}
\mathcal{L}(w, \alpha) &= \tfrac{1}{2} \|w\|^2 + \sum_{i=1}^{n} \alpha_i g_i(w) \\
&= \tfrac{1}{2} \|w\|^2 - \sum_{i=1}^{n} \alpha_i \left[y_i \left(w^T K(x_i, x_j) + b \right) - 1 \right]
\end{aligned}
\tag{3.39}
$$

$$
\begin{aligned}
\theta_{\mathcal{D}}^* &= \max_{\alpha} \min_{w} \mathcal{L}(w, \alpha) \\
&\leqslant \min_{w} \max_{\alpha} \mathcal{L}(w, \alpha) = \theta_{\mathcal{P}}^*
\end{aligned}
\tag{3.40}
$$

(w, b) in (3.38) can be obtained with the condition that $\theta_{\mathcal{D}}^* = \theta_{\mathcal{P}}^*$, which is also refered to as Karush-Kuhn-Tucker (KKT) conditions [51].

3.2.5 System Model

In this subsystem we propose physical layer simulation model for a visible light communication system, which is a part of our previous research [52]. Simulation model consists of 3 parts, VLC transmitters (T_x), receiver (R_x), and 6-axis sensor embedded at the receiver. Simulation area consists of 38 transmitters, in room area of 6 m $\times$ 12 m $\times$ 3 m. Details of simulation can be found in Table 3.4 and Fig. 3.8, where receivers are uniformly distributed along x and y axis. Vertical height (H) between T_x and R_x is assumed as

$$
H(h) = 1.5 \text{ m} + U(\Delta f(h))
\tag{3.41}
$$
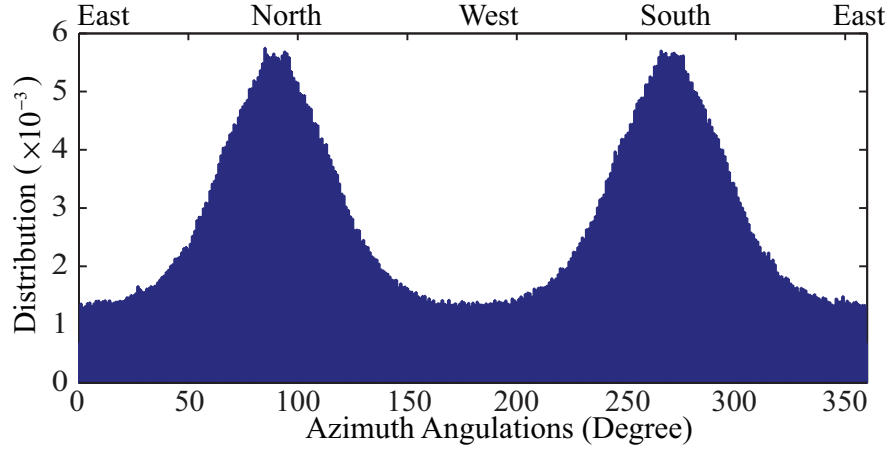
Figure 3.9: Azimuth angulations distribution from simulation environment.

$U(\Delta f(h))$ is the uncertainty range. The probability density function (PDF) of $\Delta f(h)$ is expressed as

$$\Delta f(\cdot) = \begin{cases} \dfrac{1}{b-a}, & \text{for } a \leqslant (\cdot) \leqslant b \\ 0, & \text{for } (\cdot) < a \text{ or } (\cdot) > b \end{cases} \tag{3.42}$$

(a, b) are range value equal to $(-0.1, +0.1)$ m, respectively [52]. Azimuth (β) and Tilt (ϕ) angulations are generated from pairwise between $T_x(x, y)$ and $R_x(x, y)$ denoted as **TR**, which is uniformly selected from

$$Dist\left(T_x\left(x,y\right), R_x\left(x,y\right)\right) \leqslant H\left(x\right) \cdot \cot\left(\Phi_{1/2}\right) \tag{3.43}$$

The condition in (3.43) is selected based on transmitter half-power angle $(\Phi_{1/2})$.

We assumed that no angulations errors as in [52]. Hence, Tilt and Azimuth angulations can be calculated as

$$\phi\left(h, \psi_c\right) = \tan^{-1}\left(Dist\left(\mathbf{TR}\right)/H\left(h\right)\right) + U\left(\Delta f\left(\psi_c\right)\right) \tag{3.44}$$

$$\beta\left(x, y\right) = \begin{cases} \tan^{-1}\Theta, & \text{for } Dist\left(\mathbf{TR}\right)/\Xi > 0 \\ \tan^{-1}\Theta + 180^o, & \text{for } Dist\left(\mathbf{TR}\right)/\Xi < 0 \end{cases} \tag{3.45}$$

where $\Theta = \left(T_x\left(y\right) - R_x\left(y\right)\right)/\Xi$, and $\Xi = \left(T_x\left(x\right) - R_x\left(x\right)\right)$. $U(\Delta f(\psi))$ is the uncertainty range created from FOV, which have PDF that shown as in (26) with value of $(-\psi_c, +\psi_c)$. Intuitively, $\beta(x, y)$ should be a uniform distribution. However, to prevent the case that $\beta(x, y)$ is pointing to direction that has no transmitters, we use relationship of **TR** to define $\beta(x, y)$.

3.2.6 Performance Evaluation

Figure 3.10 and 3.11 are visible light propagation path calculated from geometric optics explained in (3.21) to (3.26). The input distribution of Azimuth (β) angulation is presented
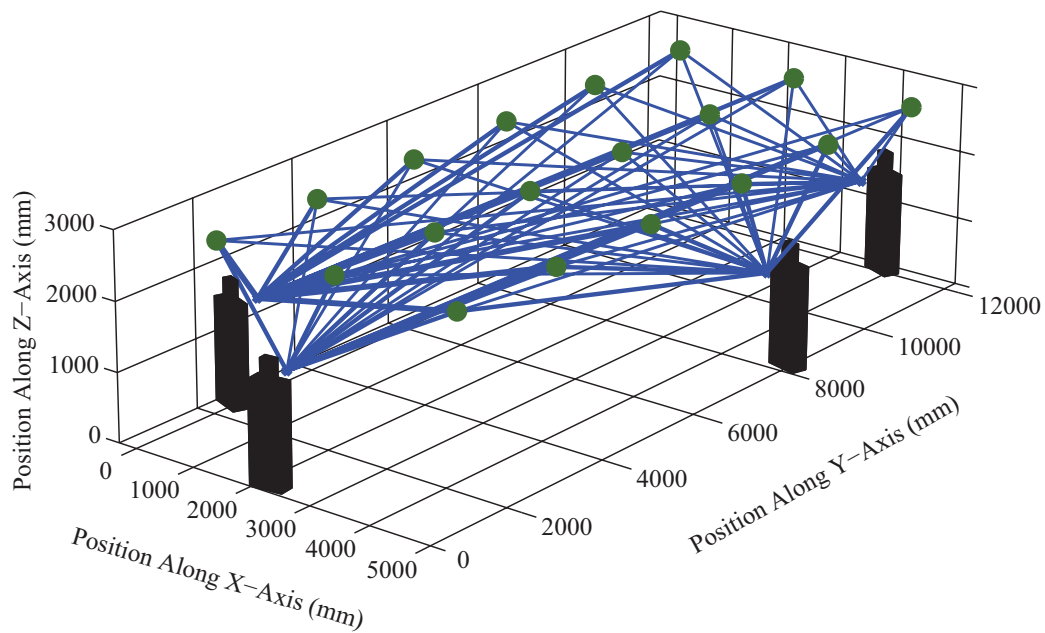
Figure 3.10: All possible LOS propagation paths calculated from geometric optics.
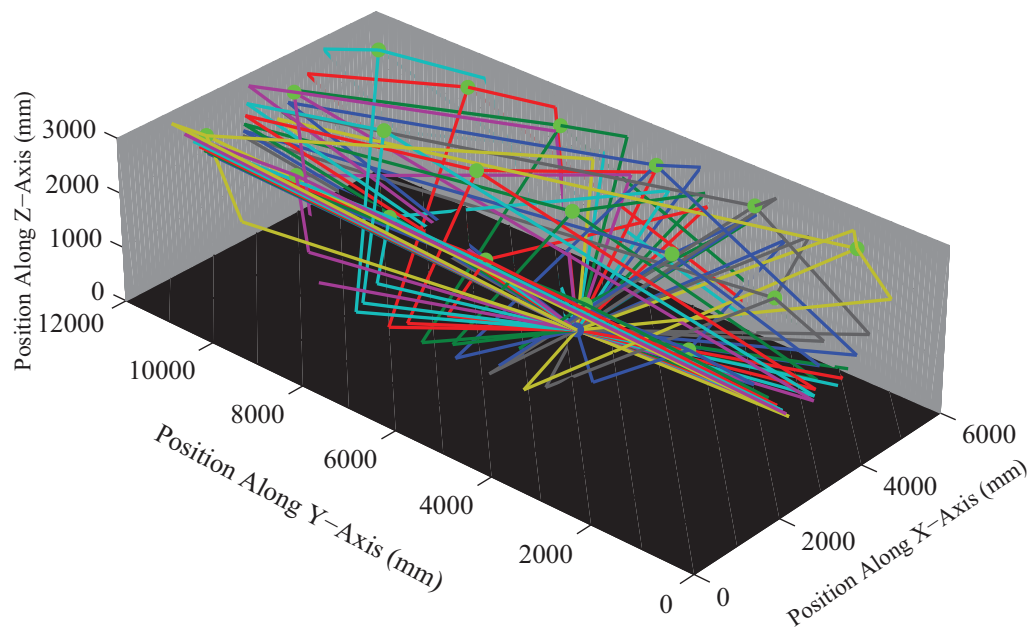
Figure 3.11: Reflected propagation paths calculated from geometric optics.
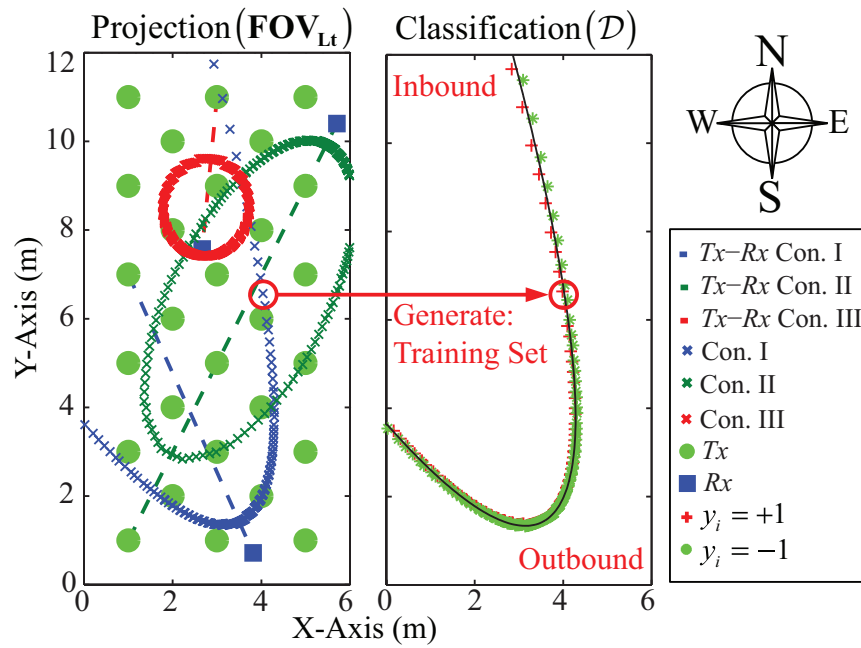
Figure 3.12: Example of FOV's cone projection and training set for SVM.
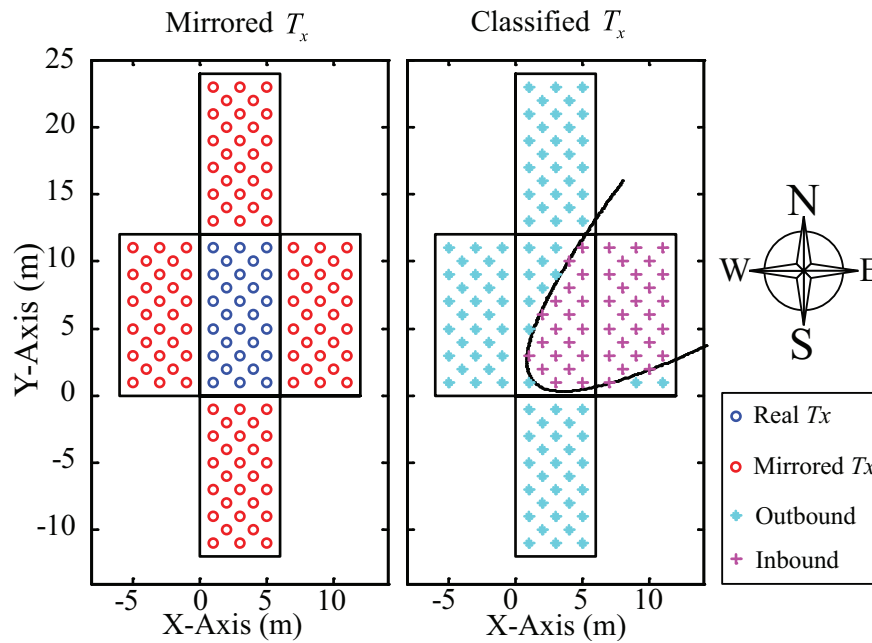
Figure 3.13: An illustration of transmitters and its mirrors. Only transmitter and its mirrors that classified as inbound region are calculated
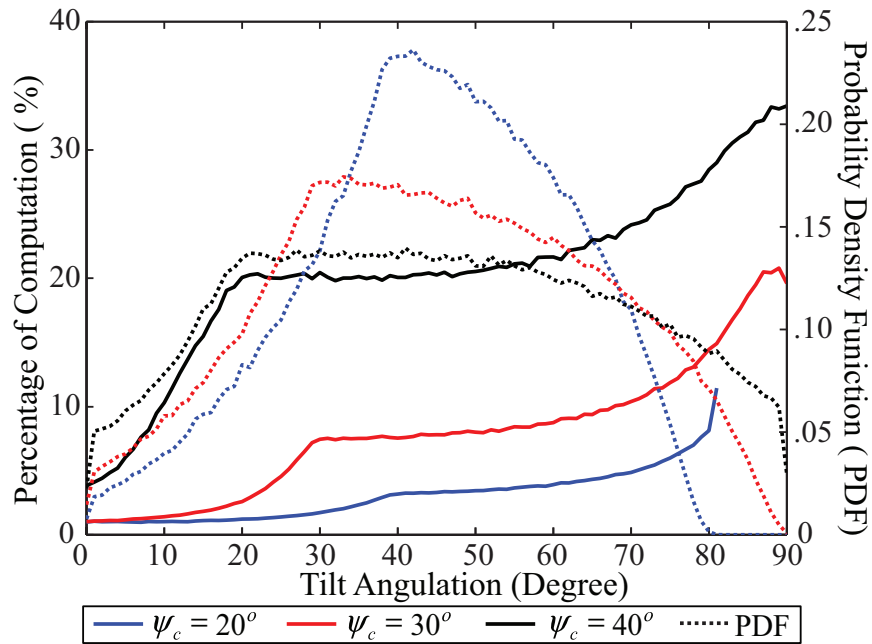
Figure 3.14: The proposed method percentage of computation over conventional system. In general cases only 20 % of computation is required
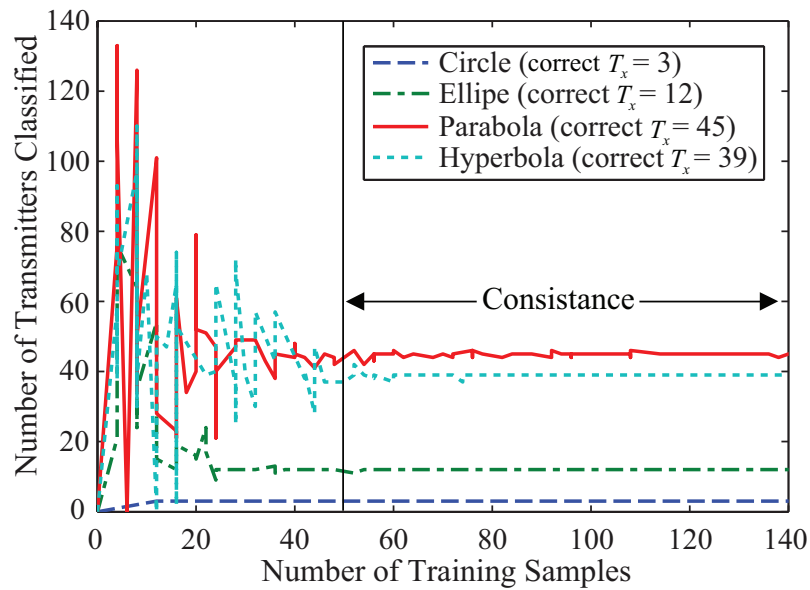
Figure 3.15: Number of training samples required for SVM to classify each type of conics section

in Fig. 3.9. Figure 3.12 illustrates conic sections ($\mathbf{FOV_{Lt}}$) and a set of training samples ($\mathcal{D}$) for SVM. Square symbol represents R_xs, circle represents T_xs and dashed line represents **TR**. Training samples ($\mathcal{D}$) are generated from $\mathbf{FOV_{Lt}}$ as described in (3.36), where $y_i = +1$ (inbound) and $y_i = -1$ (outbound) conditions; represented by "+" and "*", respectively in Fig. 3.12. The solid line represents decision boundary of (3.37). Figure 3.13 shows the mirrored position of T_xs from Figs. 2.12 and 3.12. Only T_xs that have inbound condition are calculated in (2.5)$-$(2.8) and (3.21)$-$(3.26). Because the outbound T_xs have condition that $\psi > \psi_c$, of which $H_d(0)$ and $H_{ref}(0)$ are equal to 0.

We analyze effectiveness of the proposed model by percentage of calculated T_x, and training samples required for SVM. Figure 3.14 left-axis shows percentage of calculated T_x, and right-axis shows PDF of simulated Tilt angulations. The results confirm that percetage of calculated T_x can be reduced over 80 % in the entire cases. Figure 3.15 shows relationship between training set's size, and correctness of classification achieved by SVM. The complexity of SVM method is increased in proportion to the size of training sets. However, with only 50 samples for training set, 25 samples for inbound and 25 samples for outbound condition, classifier can perform accurately in the entire cases.

3.3 Conclusion

In this chapter, we proposed enhancement modules for SwERP scheme, of which is proposed based on sensitivity and FOV limits. Sensitivity limit is originally used to find the nearest transmitter information. The first proposed module is focused on developing a nearest transmitter classification (NTC) method by utilizing Optical Orthogonal Code (OOC) with On-Off Keying (OOK) modulation at transmitters (T_xs), and perform oversampling at a receiver (R_x) to overcome the limitation of bandwidth resolution ($\mathcal{B}$). Furthermore, based on FOV limits we propose a physical simulation model for 6-Axis sensor assisted VLC based positioning system.

Nearest Transmitter Classification Method

Firstly, we propose a nearest transmitter classification method called NTC_{OC} based on TOA technique for Switching Estimated Receiver Position (SwERP) scheme. Hypothetically, TOA technique can provide highest positioning accuracy rely on the bandwidth resolution ($\mathcal{B}$). Optical Orthogonal Code (OOC) and oversampling are implemented at R_x to overcome the limitation of $\mathcal{B}$. We analyze the effectiveness of our proposed method by nearest T_x correct classification over the varied transmitter signal to noise ratio, and oversampling factor versus extra computation complexity during auto-correlation function calculation. The results confirm that the proposed method can classify the nearest T_x accurately, with some tradeoff with system complexity from the increment of oversampling factor (O_c).

Physical Simulation Model

We propose a physical simulation model for a 6-axis assisted VLC based positioning system. SVM and 3D rotation matrix are used to calculate precise FOV Limit. Based on the Sensitivity and FOV Limits, possible Azimuth and Tilt angulations are mathematically defined. We discover that the propose model can reduce computation redundancy during GO calculation over 80 % in the entire evaluation cases.

Chapter 4

MRSS Fingerprinting Subsystem Architecture

In this chapter, we discuss the method of design and implementation for multi-band received signal strength (MRSS) fingerprinting architecture. The proposed VLC based positioning architect chapter 2 has a curial communication barrier as visible light cannot penetrate through blockage such as when terminal is inside pocket. Furthermore, remote positioning cannot always be achieved in VLC based positioning system, due to the previously mentioned condition. In the main objective of our proposed architecture is not to introduce any extra infrastructure to perform localization. Therefore, only transmitted signal from existing infrastructures (e.g. WLAN, digital broadcasting system, cellular network) and other emerging wireless technology infrastructures are used for localization purpose. In cooperation with multi-band capable receiver; such as cognitive radio [2], receiver can simultaneously access to the numerous frequency bands without installing any extra infrastructures. Moreover, radio wave provides higher accessibility than VLC based positioning system as explained in chapter 2. Thus, more pervasive positioning can be achieved even without LOS between transmitter and receiver.

4.1   Basic Infrastructure

The proposed MRSS fringerprinting architecture is developed based on RSS fingerprinting, radio map [12], which is the statistical approach. Rather than estimating distance to the transmitters and performing triangulation to estimate position, RSS fingerprinting estimates positions by recognizing correlation between measured RSS and the premeasured RSS database; denoted as fingerprint. Thus, exact locations of the wireless infrastructures are not required to perform localization. There are two major advantages of our propose MRSS fingerprinting architecture. Firstly, the fingerprint at each location can be created by RSS from numerous types of existing wireless network infrastructures, as a result of deploy-

ing frequency diversity on RSS fingerprinting, without prior knowledge of those transmitter locations. Secondly, Fingerprinting method is a database approach that can initiate highly compatible platform as shown in Fig. 4.1. MRSS fingerprints are constructed from both singleband and multiband radio terminal. Therefore, any type of terminal that has premeasured RSS recorded in MRSS fingerprints can utilize the MRSS fingerprint for localization. The core elements of our proposed architect are harvesting terminals, wireless infrastructure, and localization engine. The detail and functionality of each element are elaborates in the following sections.

4.1.1 Cognitive Radio

We assume that harvesting (premeasuring) terminals in this evaluation are cognitive radio terminals. Cognitive radio is regarded as a future solution for the spectrum scarcity problem, by providing multiband capability terminal. The multiband aspect of cognitive radio is the basis of this subsystem for indoor positioning information. Cognitive radio requires location information to perform opportunistic spectrum usage management [2]. However, cognitive radio terminals are not commercially applicable in market yet. Thus, we use dualband WLAN (2.4/5.2 GHz) as the replacement for ideal cognitive radio terminal. The underlying challenge is to prove that existing multi-type wireless infrastructures can be used to provide reliable and economical solution for location information.

4.1.2 Existing Infrastructure

In the recent years, the market of wireless communication and multimedia service experienced a large increased, driven by the fast growing of internet database services [54]. There have been several evolutions of mobile generations (from 2G to 4G), many new infrastructures had been introduced to support its advance function while the old infrastructures are still operating. The perspective of today's information society require a versatility of devices, including home appliances, vehicles, personal computers, sensors, actuators, all of which can be globally connected via internet protocol (IP). The objective of this proposal is to create a lifetime evolution indoor positioning system that still can be used by our descendant. Thus, we design the proposed architecture to be compatible with existing infrastructure and any emerging technologies without introducing any extra infrastructure. RSS access method is the key technology to enable our propose architecture owing to its high compatibility and accessibility regardless of modulation schemes, as explained in section 1.2.1.

The proposed architecture is illustrated in Fig. 4.1, MRSS Fingerprinting server is the only infrastructure we introduced to the architecture. Multiband and singleband terminal are used to premeasuring RSS of broadcasting channel from existing wireless infrastructure such as WLAN, WiMax, WCDMA and other emerging technology such as LTE+. The premeasured RSS can be collected through internet from either any type of wireless access technology, or via smart pay system transaction at convenient story, subway, . . . etc. In this

MRSS Fingerprinting

Internet

Router

WLAN

ASN-GW

RNS: LTE+

P-GW

S-GW

GGSN

WiMax

AP

((•))

BS

HLR

eNodeB

RFID

RNS: HSPA

SGSN

MSC

RNC

BSS: GSM

BSC

Multiband
Terminal

NodeB

BTS

Convenient Store,
Vending Machine, Subway, ..., etc.

Existing Infrastructure

BTS:	Base transceiver station	RNC:	Radio network controller
BSC:	Base station controller	NodeB:	3G base station
BSS:	Base station subsystem	eNodeB:	LTE base station
MSC:	Mobile switching center	SGW:	Serving gateway
HLR:	Home location register	PGW:	Packet data network gateway
SGSN:	Serving GPRS support node	ASNGW:	Access services network GW
GGSN:	Gateway GPRS support node	BS:	WiMax base station
GPRS:	General packet radio service	AP:	Access point

Figure 4.1: Infrastructure of MRSS fingerprinting based positioning system.

chapter, we are trying to prove that by implementing frequency diversity on conventional RSS fingerprinting, higher achievable positioning accuracy can be realized.
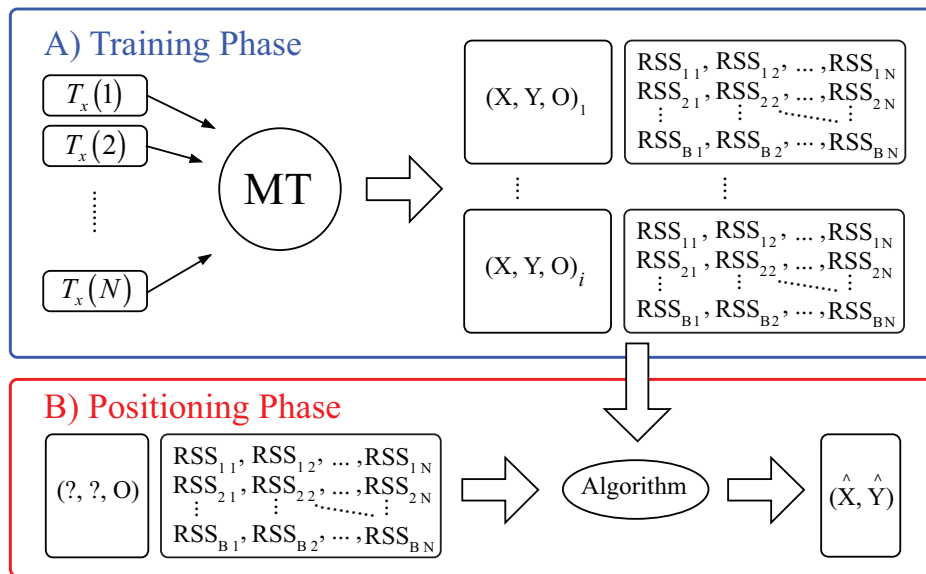
Figure 4.2: Multiband RF Fingerprint diagram A) Training phase, MRSS are premeasured. B) Positioning phase, instantaneous MRSS are compared with MRSS database.

4.1.3 Principle of MRSS Fingerprinting

So as conventional RSS fingerprinting, MRSS fingerprinting consists of two phases, which are training and positioning phases as shown in Fig. 4.2. In the training phase, fingerprint of each location is created as reference database. In the positioning phase, the instantaneous measured RSSs are compared to the fingerprint, from the training phase to estimated location. The details of both are provided in the following subsection.

Training Phase

The MRSSs are premeasured in order to create database, fingerprint, as illustrated in Fig. 4.2A. Generally MRSS Fingerprint, $\mathfrak{MF}$, is comprised of Fingerprint, $\mathfrak{F}$, from each frequency band, $[1,2, \ldots, \mathfrak{B}]$, as shown in

$$\mathfrak{MF} = [\mathfrak{F}_1, \mathfrak{F}_2, \ldots, \mathfrak{F}_{\mathfrak{B}}] \tag{4.1}$$

The location fingerprints and their labels, location information $\mathfrak{L}$, are usually denoted as a tuple of $(\mathfrak{MF}, \mathfrak{L})$. The received signal strength of dataset, premeasured during training phase is referred to as a training set [14]. In this subsystem, we define the location information as two-dimensional system which can be expressed as (4.2). The location information components are stored as coordinate x and y, with the orientation $\{o|o \in \{$North, East,

West, and Sout}}.

$$\mathfrak{L} = \left\{ (x, y, o) \, | \, x, y \in R^2, o \in \{N, E, W, S\} \right\} \tag{4.2}$$

To create a fingerprint, as described in [14][32], a number of RSSs are measured during a period of time for each location. In this subsystem, the average RSS of each access points are used as main indicator for fingerprint. The premeasured RSS from N access points can be written as a vector of average RSS elements, ρ_N, as shown in

$$\mathfrak{F} = (\mu_1, \mu_2, \ldots, \mu_N)^T \tag{4.3}$$

The extra fingerprint information, (e.g. standard deviation, skewness) for each RSS element, which is suggested in [12], can be added into the fingerprint as another vector:

$$\mathfrak{D} = (\sigma_1, \sigma_2, \ldots, \sigma_N)^T \tag{4.4}$$

The equation (4.4) is also applied to the standard deviation vector of MRSS, $\mathfrak{MD}$. The usages of multi-band fingerprint are provided in the following sections.

Positioning Phase

The measured RSS is compared with RSS database which was built in the training phase, as in Fig. 4.2B. In this subsystem we use deterministic type of algorithm based on nearest neighbor (NN) classifiers. The basic concept of NN is that the measured RSS is classified to the closest fingerprint value to estimate the position. Presume that a set of $\mathfrak{l}$ location multi-band fingerprints is denoted by $\{\mathfrak{MF}_1, \mathfrak{MF}_2, \ldots, \mathfrak{MF}_{\mathfrak{l}}\}$, each of which has one-to-one matching with $\{\mathfrak{L}_1, \mathfrak{L}_2, \ldots, \mathfrak{L}_{\mathfrak{l}}\}$. In the positioning phase, the measured MRSS is defined as $\mathfrak{S}$ which is the mean value of MRSS in a short measured period of time. Assuming that wireless networks have N transmitters with $\mathfrak{B}$ frequency bands, $\mathfrak{S}$ can be described as in

$$\mathfrak{S} = \begin{bmatrix} s_{11} & s_{12} & \cdots & s_{1B} \\ s_{21} & s_{22} & \cdots & s_{2B} \\ \vdots & \vdots & \ddots & \vdots \\ s_{N1} & s_{N2} & \cdots & s_{NB} \end{bmatrix} \tag{4.5}$$

where entries in each column show RSSs values from B different frequency band and each row show RSSs values from N different APs. Each location of multi-band fingerprint i in the database can be expressed as

$$\mathfrak{MF}_i = \begin{bmatrix} \rho_{11}^i & \rho_{12}^i & \cdots & \rho_{1B}^i \\ \rho_{21}^i & \rho_{22}^i & \cdots & \rho_{2B}^i \\ \vdots & \vdots & \ddots & \vdots \\ \rho_{N1}^i & \rho_{N2}^i & \cdots & \rho_{NB}^i \end{bmatrix} \tag{4.6}$$

where entries in each column show average value of MRSS from B different frequency band and each row show average value of MRSS from N different APs. Thus, machine learning algorithms, explained chapter 1, are applied on $\mathfrak{S}$ and $\mathfrak{MF_i}$ in order to find the most similar pair of signal vector.

4.2 Wireless Chanel Characteristics

Propagation models are fundamental tools for analyzing wireless network characteristics for design and implementation purpose. A propagation model predicts what will happen to the transmitted signal through different environment at the receiver. In general, there are five attributes that varied transmitted signal characteristics are propagation loss, reflection, diffraction, transmission and scattering, of which partially explained in section 1.4. The signal is wakened and distorted in particular ways from the five mentioned attributes. The purpose of the design is to ensure that transmitted information is to be successfully delivered to the receivers after implementation. In our proposed architecture, we only use existing infrastructure, since no transmitters design are required, thus propagation models are solely used to explain the characteristic our proposed architecture.

In the early days of cellular system deployment, the Hata-Okumura model was very widely used for predicting the coverage of cell sites [20]. Unfortunately, this model was developed in relatively flat areas so it did not explicitly design for indoor environment which is the main focus of our proposed architecture. The result was poor coverage, impaired system performance. Currently, there are more advanced and sophisticated models available, Choosing and applying the appropriate propagation model is an important aspect of wireless system design [20]. Some sample of propagation models are explained in the following sections.

4.2.1 Empirical Model

Empirical models are created based on observations or measurements. For propagation models, these measurements are typically done in the field to measure path loss, delay spread, or other channel characteristics. Empirical models are widely used in mobile radio and cellular system engineering. The measurements are then used to refine empirical propagation models used in the system-planning tool [20]. We provide example the sample models are those currently being used for system dimensioning. Lastly, we elaborate the suitability on our proposed architecture.

IEEE 802.16 (SUI) Models

The IEEE802.16 standards empirical model was developed for bands above 11 GHz, the mentioned model was published in [55][56]. For frequencies below 11 GHz was proposed by

Table 4.1: Model Constants for IEEE 802.16 Model for 2.5 2.7 GHz Band

Model constant	Terrain Type A	Terrain Type B	Terrain Type C
a	4.6	4.0	3.6
b	0.0075	0.0065	0.005
c	12.6	17.1	20

Table 4.2: Terrain Types

Terrain types	Delay spread	Rice k factor	Doppler
A	Low	High	Low
	Low	High	Low
B	Low	Low	Low
	Moderate	Low	High
C	High	Low	Low
	High	Low	High

Stanford University Interim (SUI). The basic path loss model and categorization of propagation environments was taken from [57]. This basic path loss equation is illustrated as follows:

$$L = A + 10\gamma \log\left(\frac{d}{d_0}\right) + X_f + X_h + s \quad \text{for} \quad d > d_0 \tag{4.7}$$

where d is the distance in meters, $d_0 = 100$ meters, h_b is the base station height above ground in meters (10 m $< h_b <$ 80 m), with

$$A = 20 \log\left(\frac{4\pi d_0}{\lambda}\right) \tag{4.8}$$

and

$$\gamma = \frac{a - bh_b + c}{h_b} \tag{4.9}$$

The constants a, b and c are chosen on the basis of one of three environments designated as A, B or C as shown in Table 4.1

The terms X_f and X_h are correction factors for frequency and receiver (remote terminal) antenna height above ground, respectively. These corrections are defined as

$$X_f = 6.0 \log\left(\frac{f}{2000}\right) \tag{4.10}$$

$$X_h = -10.8 \log\left(\frac{h_m}{2.0}\right) \quad \text{for Terrain Types A and B} \tag{4.11}$$

$$X_h = -20.0 - \log\left(\frac{h_m}{2.0}\right) \text{ for Terrain Type C} \qquad (4.12)$$

where f is the frequency in MHz and h_m is the receiver (remote terminal) height above ground in meters.

The term s is a lognormal-distributed path loss factor that takes into account shadow fading from trees and structures. From [58], the standard deviation of s is typically 8.2 to 10.6 dB, depending on the terrain type explained in Table 4.2.

COST-231 Hata Model

The COST-231 Hata model [59] was devised as an extension to the HataOkumura model [60][61]. The HataOkumura model is an empirical model developed for the 500 to 1500MHz frequency range using measurements done by Okumura [61] and equations fitting to the path loss curves by Hata [60]. The COST-231 model also has correction for urban, suburban, and open areas. Further extensions to these models could perhaps adapt them to the MMDS band. For these reasons, the COST-231 Hata is included here. The basic path loss equation for urban areas is

$$\begin{aligned}
L_u = 46.3 &+ 33.9 \log_{10} f - 13.82 \log_{10} h_b - ah_m \\
&+ (44.9 - 6.55 \log_{10} h_b) \log_{10} d + c_m dB
\end{aligned} \qquad (4.13)$$

$$ah_m = (1.1 \log_{10} f - 0.7) h_m - (1.56 \log_{10} f - 0.8) \qquad (4.14)$$

where:

c_m = 0 dB for medium sized city and suburban centers.
c_m = 3 dB for metropolitan centers.
f = frequency in MHz.
d = distance from the T_x to the R_x in kilometers
h_b = height of the T_x above ground in meters
h_m = height of the R_x above ground in meters

The COST-231 Hata model has many of the same limitations for detailed system planning as the SUI models. Nonetheless, because of their simplicity, they are widely used for system dimensioning and other generic system concept formulations.

Both of the mentioned empirical models, mentioned in sec. 4.2.1, are not suitable for our propose architecture due to the reason that (4.5) in any position generated from different frequency has high correlation and cannot be used to improve accuracy on our proposed system. The estimated received signal strengths predicted from empirical models are very rough. Thus, we use ray-tracing which is one of the physical models and perform experiments to explain our proposed system.

4.2.2 Ray-Tracing

Ray-tracing is one of the site-specific simulation models, which is widely used to investigate the radio wave behavior in both indoor and outdoor environment. In recent years, a propagation modeling approach known as ray-tracing has seen considerable interest. Ray-tracing is a method based on combining geometric optics (GO), the uniform theory of diffraction (UTD), and other scattering mechanisms, which can predict electromagnetic wave propagation. The notion of a 'ray' is fundamental to ray-tracing, which is the same as explained in (3.2.1). It arises in GO where EM energy is considered to be flowing outward from a radiating source in ray tubes.

Ray-tracing itself is a long-used technique that can be traced back to Maxwell established a connection between optics and electromagnetism in 1873. The current ray-tracing model is based on Kouyoumjian and Pathak [62] who devised the UTD, which applied a Fresnel integral to correct for the singularities at the shadow and reflection boundaries. Thus, ray-tracing is applicable for dealing with a wide variety of high-frequency electromagnetic problems in which can explain the contribution of our proposal. The ray-tracing has one limitation that wavelength used in the simulation must be much smaller than the dimensions of the physical features involved. Thus, Ray-tracing is a 'model' provides useful results especially new type of systems that are not conveniently available with empirical models. The mechanisms involved in ray-tracing models are in the form of 5 propagation primitive', which are free-space propagation, specular reflection, diffraction, diffuse wall scattering and wall transmission in combination.

The result is that each ray upon reaching the receiver has undergone a cascade of interactions that determine its amplitude, phase, and time delay. The details of each of the propagation primitives were discussed in section 1.4. An important assumption in the use of ray-tracing, GO, and UTD, is that the physical dimensions of the scattering objects are large compared to the wavelength. Using this assumption, the interaction of the propagation primitives with the rays can be considered separately. As mentioned, the amplitude and phase of the EM field at the receiver represented by an arriving signal ray can be found by considering the impact on the ray of all the interactions with the propagation environment it has had in transit from the transmitter to the receiver. The field at the receiver is thus given by

$$E_r = \frac{1}{s_f'} \sqrt{\frac{P_T G_T Z_0}{4\pi}} \left[\prod_i \mathbf{R}_i \right] \left[\prod_n A\left(s_n', s_n\right) \overline{\overline{\mathbf{D}_n}} \right] \left[\prod_l A_{scat,l} \right] \left[\prod_k A_{tran,k} \right] \qquad (4.15)$$

where:
Note that the diffraction coefficient and diffraction spatial attenuation factor are specific to the path lengths into and away from the nth wedge from wherever the illuminating source and onward receiving point or surface are located. If diffuse wall scattering or wall transmission occur along the ray path, the additional attenuation factors shown as terms 4 and 5 of (4.15) are included. Regarding the (4.15), estimated (4.5) in each position can be differed from

s'_f is the total ray trajectory length

$\sqrt{\frac{P_T G_T Z_0}{4\pi}}$ is the free-space attenuation component where Z_o is the plane wave free-space impedance, P_T transmitter power, and G_T transmitting antenna gain

$\mathbf{R}_i$ is the reflection coefficient from section 1.4.1 for the $i-$th reflection on the ray path (a complex number)

$\overline{\overline{\mathbf{D}}}_n$ is the diffraction coefficient from section 1.4.2 for the $n-$th diffraction wedge on the ray path (a complex number)

$A\left(s'_n, s_n\right)$ the spatial attenuation factor diffraction coefficient from section 1.4.2

$A_{scat,l}$ is the scattering coefficient if scattering is included for objects in the model

$A_{tran,k}$ is the wall transmission coefficient if the model

frequency diversity, caused by wavelength property, reflection, diffraction, and transmission. We proved our claim by performing experiment, of which will be deliberated in the next section.

4.3 Proposed System

This chapter proposes a MRSS fingerprinting architecture, which employs based on frequency diversity over the conventional RSS fingerprinting. By deploying frequency diversity on RSS fingerprinting, higher achievable positioning accuracy can be realized, as a result of the increment of RSS fingerprint resolution, and also the increment of correct estimation probability in positioning phase. However, the improvements are arguably not only caused by the effects of frequency diversity but also by the RSS of additional transmitters. Therefore, in our experiment, we use transmitters that simultaneously transmit dual band signal, to prove that positioning accuracy can be enhanced solely by the effect of frequency diversity.

Based on the previous researches, the conventional RSS fingerprinting method utilizing only one frequency band of signal, the achievable accuracy have been reported in the range of 1.5 5 meter, depending on the experimental configuration [9][12][31][32]. In order to evaluate the effectiveness of the proposed system, we performed experiment under the area of 103 m^2. The K-Nearest Neighbor (KNN) classifier is utilized in the positioning phase. The results confirm that by deploying MRSS, achievable mean error distance (MED) approach closer to the error distance lower bound compared with the single-band system.

4.3.1 Characteristic Between LOS and NLOS

As mentioned in the previous section we use frequency diversity from existing infrastructure to enhance the fingerprinting resolution. In this section we discuss the limitation of proposal architecture; we focus on proving that frequency diversity itself can enhance fingerprint-
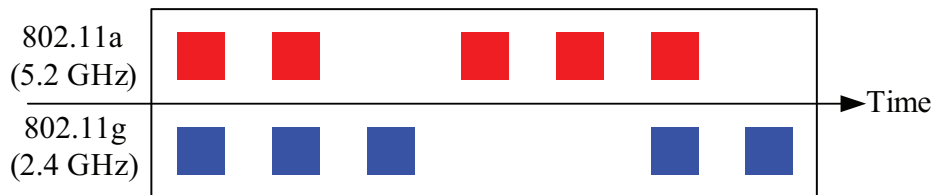
Figure 4.3: Frequency time diversity technique.

ing. Thus, we confine our studied environment as the transmitter that can simultaneously transmit multiband signals for evaluating the impact of frequency diversity effect on RSS fingerprinting resolution. The equation (4.15) shows that only free-space path loss itself cannot alternate RSS level of each frequency band. However, the effects of reflection, diffraction, transmission which are explain in section 1.4. We provide over analytical through the following subsection.

Methodology

The objective of deploying multiband signal, frequency diversity, in RSS fingerprinting is to enhance its database resolution. Wavelength has property to alter specular reflection points in each frequency band. Dynamic shadowing [63] can cause the signal to be unperceivable in a certain period of time. Hence, in the modeling, we utilize frequency time diversity for the opportunistic deployment of multiband fingerprint system, as illustrated in Fig. 4.3. In the following sections, methodologies and performance analysis used in training phase, positioning phase, frequency correlation analysis and correct estimation probability analysis will be discussed.

Training Phase

In training phase, frequency time diversity technique is deployed in order to cope with time coherence of dynamic shadowing and wavelength property. The frequency time diversity technique records all the RSSs from each frequency band during the measurement period. Only the measurable RSSs from each frequency band are used to create $\mathfrak{MF}$ for each position.

The $\mathfrak{F}$ of each frequency band is stored separately, referred to multiband received signal strength (MRSS) fingerprint, in order to enhance the $\mathfrak{MF}$ resolution. Hence, the database size of MRSS scheme is $\mathfrak{B}$ times higher than single band RSS fingerprint.

4.3.2 KNN MRSS Fingerprinting

In positioning phase, mentioned in section 4.1.3, the closest distance of signal distance, between $\mathfrak{S}$ and $\mathfrak{MF}$, is calculated by $Dist(\cdot)$ function [9][31]. The NN classifier uses the $\mathfrak{MF}_i$

that has the shortest signal distance, compare to S, among the j neighboring points; $\mathfrak{MF}_{\mathfrak{j}}$.

$$Dist\left(\mathfrak{S}, \mathfrak{MF}_{\mathfrak{i}}\right) \leqslant Dist\left(\mathfrak{S}, \mathfrak{MF}_{\mathfrak{j}}\right), \forall \mathfrak{j} \neq \mathfrak{i} \tag{4.16}$$

We modified the generalized distance, defined in [32], by RSS of multi-band signal as an additional value, as shown in (4.17). The N value is the number of access point, where B denotes the number of frequency bands that are utilized.

$$L_p^l = \frac{1}{N}\left(\sum_{i=1}^{N}\frac{1}{\omega_i}\cdot\frac{1}{B}\left|\sum_{j=1}^{B}\frac{1}{\omega_j}\left((\rho_{ij} - S_{ij})^p\right)^{1/p}\right|^p\right)^{1/p} \tag{4.17}$$

In order to realize the innate data structure of experimental results, we used an unweighted signal distance ($\omega_i = 1$ and $\omega_j = 1$). Furthermore, we illustrated achievable estimated error distance, by utilizing Manhattan distance ($p = 1$) and Euclidean distance ($p = 2$) in signal space for NN classifier in (4.16); from conventional method (singleband signal: $B = 1$) and the proposed method (multi-band signal: $B > 1$). Positioning accuracy based on NN classifier in muliband characteristics has not been studied. Thus, we study the achievable accuracy from both Manhattan and Euclidean distances, in order to maximize the capability of NN classifier.

In multiband fingerprint positioning phase, we use deterministic model such as NN and KNN [14][31]. In KNN, where K $\geqslant$ 2, those with the shortest signal distance are chosen; the average coordinates of K points can be used as the estimated position. Intuitively, KNN should provide higher accuracy, since the misclassification of the shortest signal distance point can be occurred easily due to fluctuation of RSS at the receiver; as a result from multi-path propagation. Hence, there is no reason to only pick the nearest one and abandon other nearby points.

4.3.3 Frequency Correlation Analysis

The main objective of deploying frequency diversity on RSS fingerprinting method, denoted as MRSS, is to increase fingerprint resolution. The resolution of fingerprint increased in proportion to independence of measured RSSs, which can be proved by analyzing the pairwise correlation coefficient of RSS between frequency bands at each fingerprint location.

The correlation coefficient (ρ) is a real number that falls in a range of 0 and 1. It is calculated by

$$\rho_{I,J} = \frac{\operatorname{cov}\left(I, J\right)}{\sigma_I \sigma_J} = \frac{E\left(\left(I - \mu_I\right)\left(J - \mu_J\right)\right)}{\sigma_I \sigma_J} \tag{4.18}$$

where μ_I, and ρ_I are the mean value and standard deviation of variable I, respectively. Likewise, μ_J and μ_J are mean value and standard deviation of variable J. If two signals are independent to each other, the correlation coefficient will be 0. If two signals are correlated, the correlation coefficient will approach 1 or -1, in the case of an increasing and decreasing linear relationship, respectively.

4.3.4 Correct Estimation Probability Analysis

The enhancement of accuracy is relevant to the increment of correct estimation probability at each nearest position, denoted as NCEP. For the preliminary analysis, we modified correct estimation probability, which is proposed in [64], to illustrate NCEP of our system model. Let $C_l^{k,q} = Dist\left(\mathfrak{S}, \mathfrak{MF}_i^{k,q}\right) - Dist\left(\mathfrak{S}, \mathfrak{MF}_{l,j}^{k,q}\right)$ be the comparison variable. The variable $C_l^{k,q}$ compares the signal distance, as shown in (4.17)), between measured MRSS, as in (4.5) of (a) the correct MRSS fingerprint location $\mathfrak{MF}_i^{k,q}$ and (b) the $l-$th incorrect MRSS fingerprint location $\mathfrak{MF}_j^{k,q}$. The index l runs from 1 to L excluding the correct location denoted by the index from l to $l+k$. The index k is the order of nearest neighbor classifier that runs from 1 to K, regarding K in KNN classifier. The index q shows sequence of nearest position which runs from l to $l+k$. The number L corresponds to number of entries in MRSS fingerprint location. Then, the probability of correct estimation probability at each nearest position can be written as:

$$
\begin{aligned}
P_c^{k,q} = P\Big\{ &C_1^{k,q} \leqslant 0, ..., C_{l-1}^{k,q} \leqslant 0, ..., \\
C_{l+k}^{k,q} \leqslant 0, ..., &C_L^{k,q} \leqslant 0 | q : l, .., l+k-1 \Big\}
\end{aligned}
\tag{4.19}
$$

Equation (4.19) is the probability of returning the correct location from KNN classifier for the proposed MRSS fingerprinting based indoor location system when the correct positions are ranging from $l-1$ to $l+k$ and there are L fingerprint locations in the database entries. Intuitively assuming perfect correct estimation probability, $P_c^{k,q} = 1$ such that $q = [l, l+k]$, the maximum value of K that provides highest achievable accuracy is 4. Furthermore, the lower bound of achievable accuracies of each K is calculated by assuming that $P_c^{k,q} = 1$, of which the results are shown in latter section.

4.4 Experimental Setup

We made experiment in both LOS and NLOS environments at the University of Electro-Communications and Keio University, respectively. The experiment in both environment, we use dual band of IEEE802.11 a/b/g, of which both 2.4 and 5.2 GHz frequency bands are simultaneously transmitted from the same Access Points (APs); likewise, dual band NEC Aterm WL54SU2, is used as a receiver. The experimental configurations of LOS and NLOS environments are illustrated in Fig. 4.4 and Fig. 4.5, respectively. Where 6 units of dual bands APs (802.11a/b/g) are used as transmitters and Air Magnet Survey Pro (version 6) is used for acquiring RSS values during training phase.
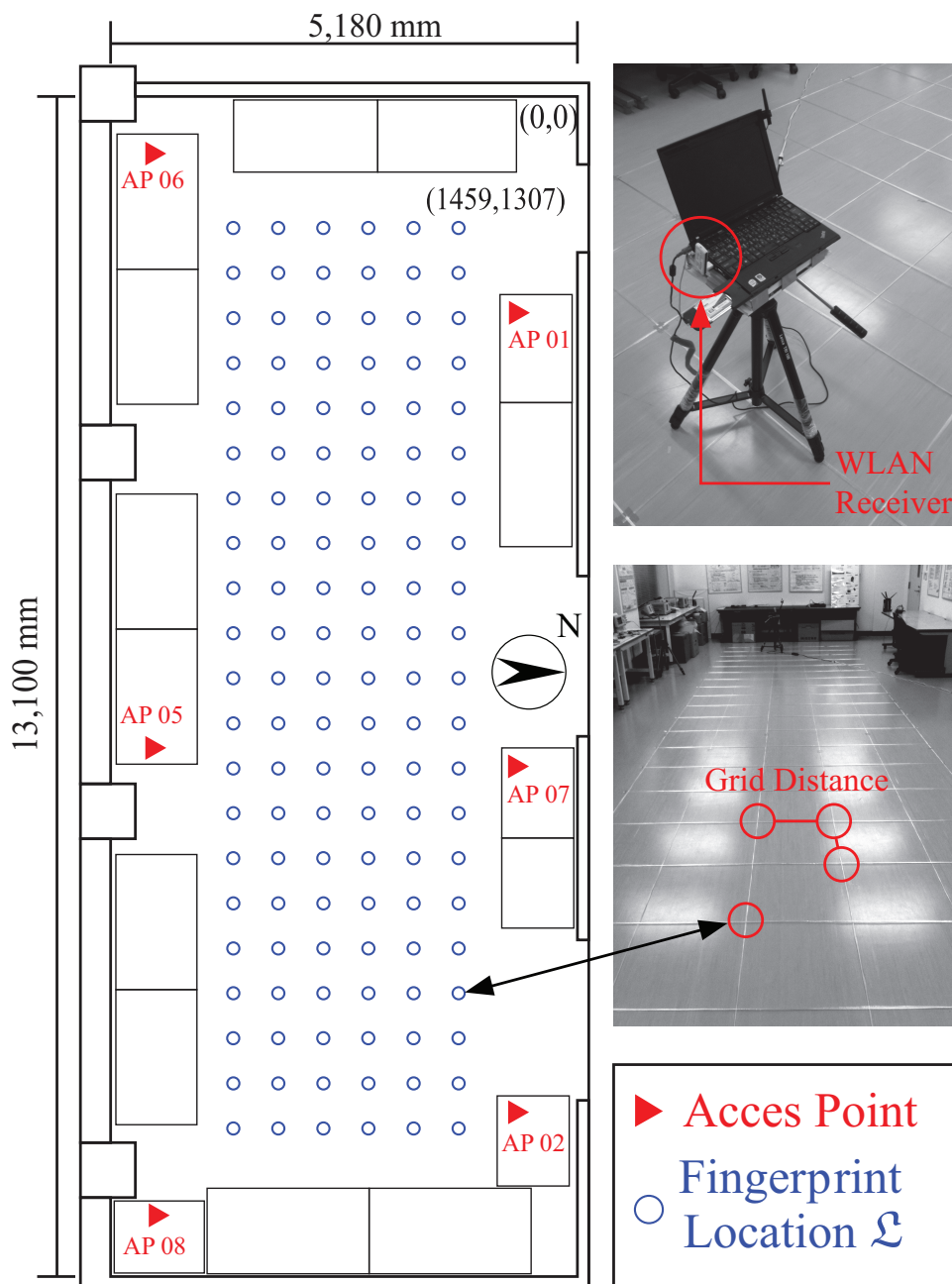
Figure 4.4: Experimental site configuration at The University of Electro-Communications, Choufu Campus, Advanced Wireless Communication Research Center (AWCC) building, 4th floor; 6 APs was distributed in every room around experimental area.
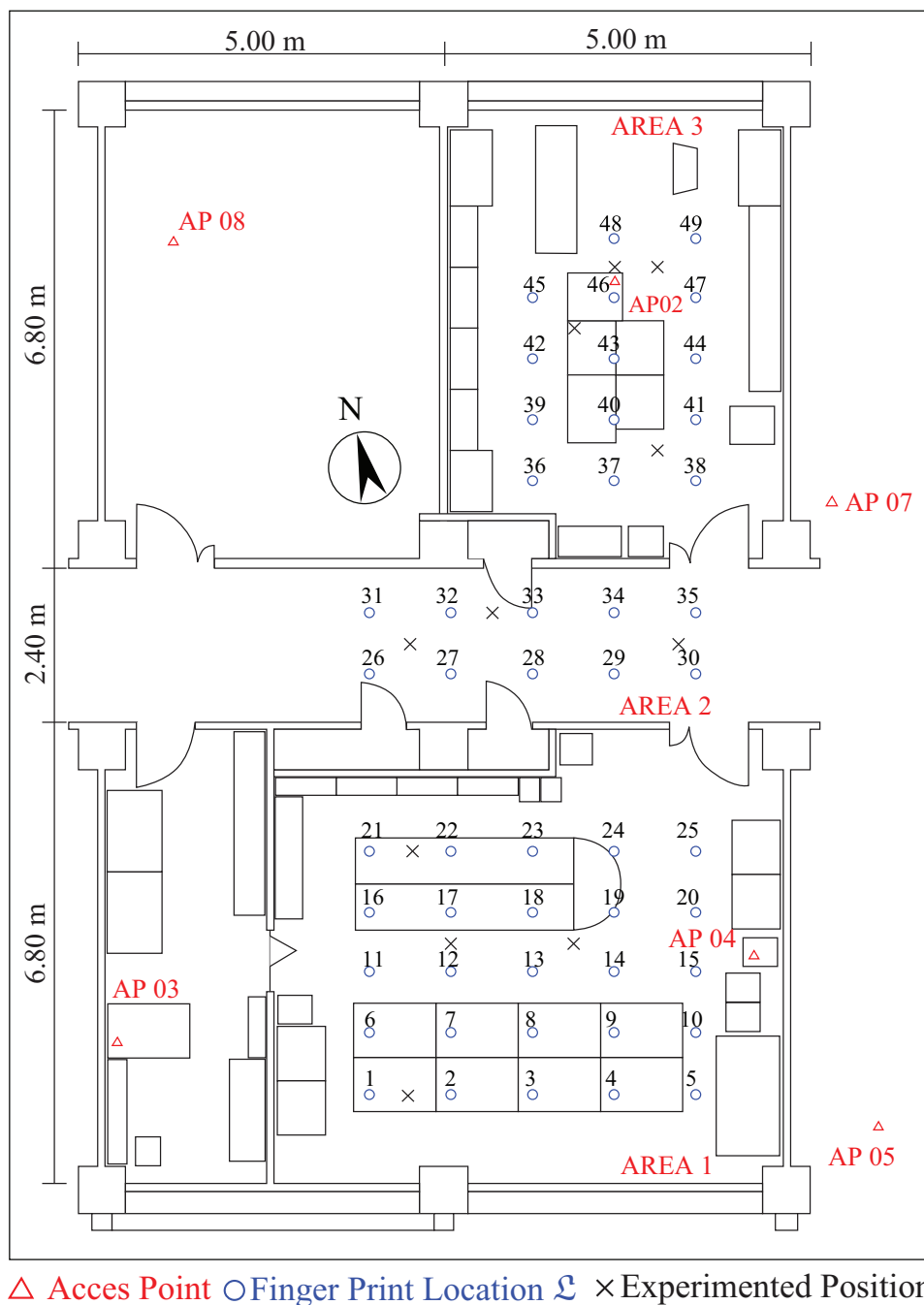
Figure 4.5: Experimental site configuration at Keio University, Yagami Campus, building 24, 3rd floor, Nakagawa laboratory; 6 APs was distributed in every room around experimental area.

4.4.1   LOS Environment

The objective of this experiment is to confirm our hypothesis discussed in section 4.3.1 that in LOS environment, the obtained RSS of multi-frequency signals show high similarity between each frequency band. The experiment were conduct with 126 fingerprint locations in the area of 67.85 m^2, shown as circle symbols in Fig. 4.4. RSS of both 2.4 and 5.2 GHz were measured, sampling rate 150 msec, with attribute of 1 second per RSS sample. Fingerprint location grid size is set to 0.5 × 0.5 m. The observation time at each fingerprint location is set to 20 mins. Details of the experimental configuration are explained in Table 4.3. The results that confirm our hypothesis are shown in the following section.

4.4.2   NLOS Environment

NLOS environment can be regarded as the most challenges for research on positioning, in this research we use NLOS to increase the positioning accuracy. Experimental parameters of the training phase are described in Table 4.4. The experiments were conducted with 49 fingerprint locations in the area of 103 m^2, shown as circle symbols in Fig. 4.5. The most of the experimental parameters are the same as used in LOS environment, except for the gird size of fingerprint location which are 0.89 × 1.2 m. In order to demonstrate the effects of deploying frequency diversity in RSS fingerprint, all the APs utilize the same dual channel of Ch.2 and Ch.40. Terminal orientation is set toward north at every fingerprint locations. In the positioning phase, we sampled RSSs from 12 positions shown as × symbols in Fig. 4.5, terminal orientation is set heading toward north. The KNN classifier with both Manhattan and Euclidean signal distances are utilized to illustrate the proposed system performance. The parameters of experimental configuration are shown in Table 4.5. The S is measured 60 seconds from each sample position, window sizes ($\mathfrak{W}_{\mathfrak{z}}$) are varied from 1 second to 10 seconds to show the impact of observation time in positioning phase over the achievable accuracy. The results of the proposed method are shown in the following section.

4.5   Performance Evaluation

The evaluations of the proposed system are divided into 5 parts, which are the comparison time series of RSS between 2.4 and 5 GHz frequency bands, illustration of LOS and NLOS MRSS fingerprint in different view, frequency correlation, correct estimation probability and effectiveness of proposed system, which is evaluated by mean error distance from estimated position. The results of each case are elaborated through the following subsections.

4.5.1   RSS Time Series

The RSS from each AP shows the unique characteristic between frequency bands at each position, which make MRSS fingerprint resolution enhanced. The enhancement contributed

Table 4.3: Training Phase Experimental Parameters of LOS Environment

Parameters	Quantity
Channel (B)	Ch.2 (2.4 GHz), Ch.40 (5 GHz)
Number of AP (N)	6 APs
Grid Size	0.5×0.5 meter
Fingerprint Location (l)	126 Positions
Measurement Time	20 mins/ position
Symbol Period	1 sec/symbol
Sampling Rate	150 msec
Terminal Orientation (o)	North

Table 4.4: Training Phase Experimental Parameters of NLOS Environment

Parameters	Quantity
Channel (B)	Ch.2 (2.4 GHz), Ch.40 (5 GHz)
Number of AP (N)	6 APs
Grid Size	0.89×1.20 meter
Fingerprint Location (l)	49 Positions
Measurement Time	20 mins/ position
Symbol Period	1 sec/symbol
Sampling Rate	150 msec
Terminal Orientation (o)	North

Table 4.5: Positioning Phase Experimental Parameters of NLOS Environment

Parameters	Quantity
Channel (B)	Ch.2 (2.4 GHz), Ch.40 (5 GHz)
Number of AP (N)	6 APs
Experimented Position	12 Positions
Measurement Time	60 sec/ position
Window Size ($\mathfrak{W}_{\mathfrak{z}}$)	$1 - 10$ sec/symbol
Sampling Rate	150 msec
Terminal Orientation (o)	North
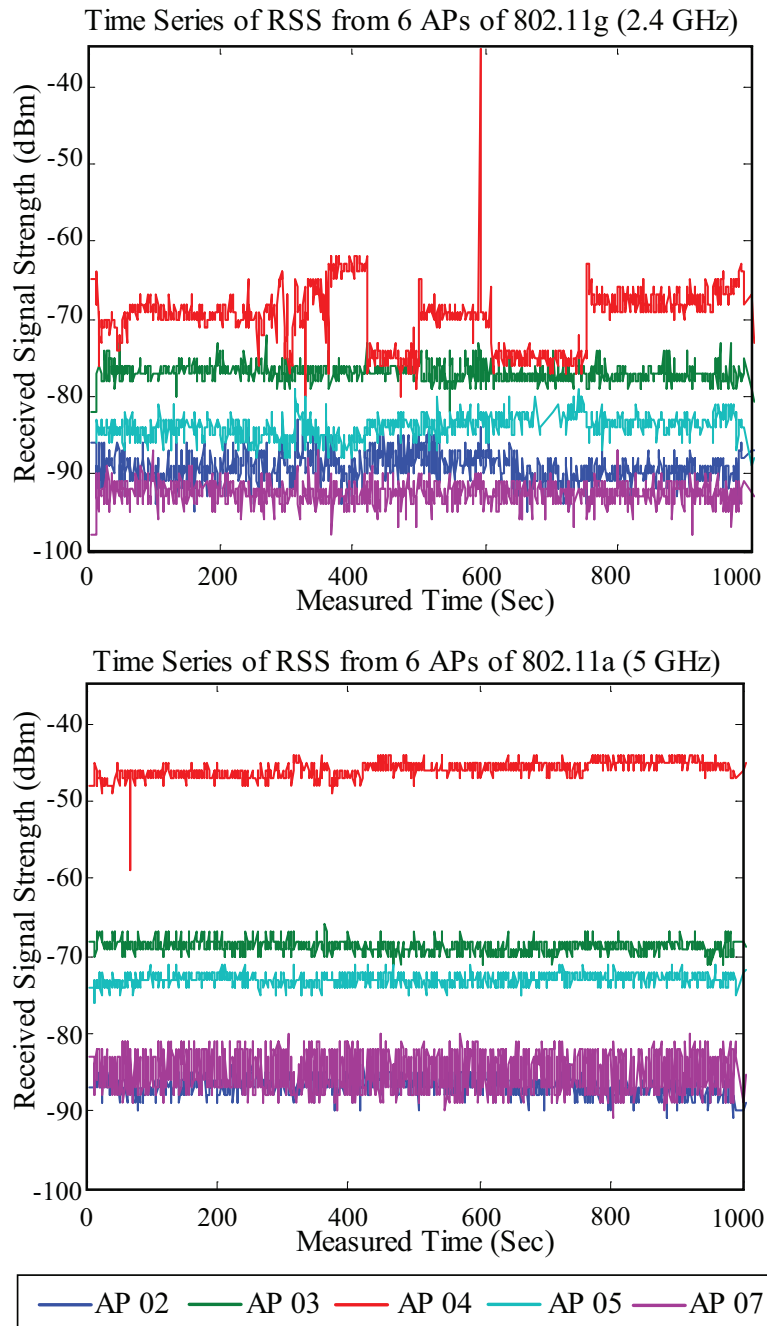
Figure 4.6: Time series of MRSS of both frequency band (2.4 and 5 GHz) at position 11. The x−axis shows the measured time in second. The y−axis shows received signal strength in dBm.
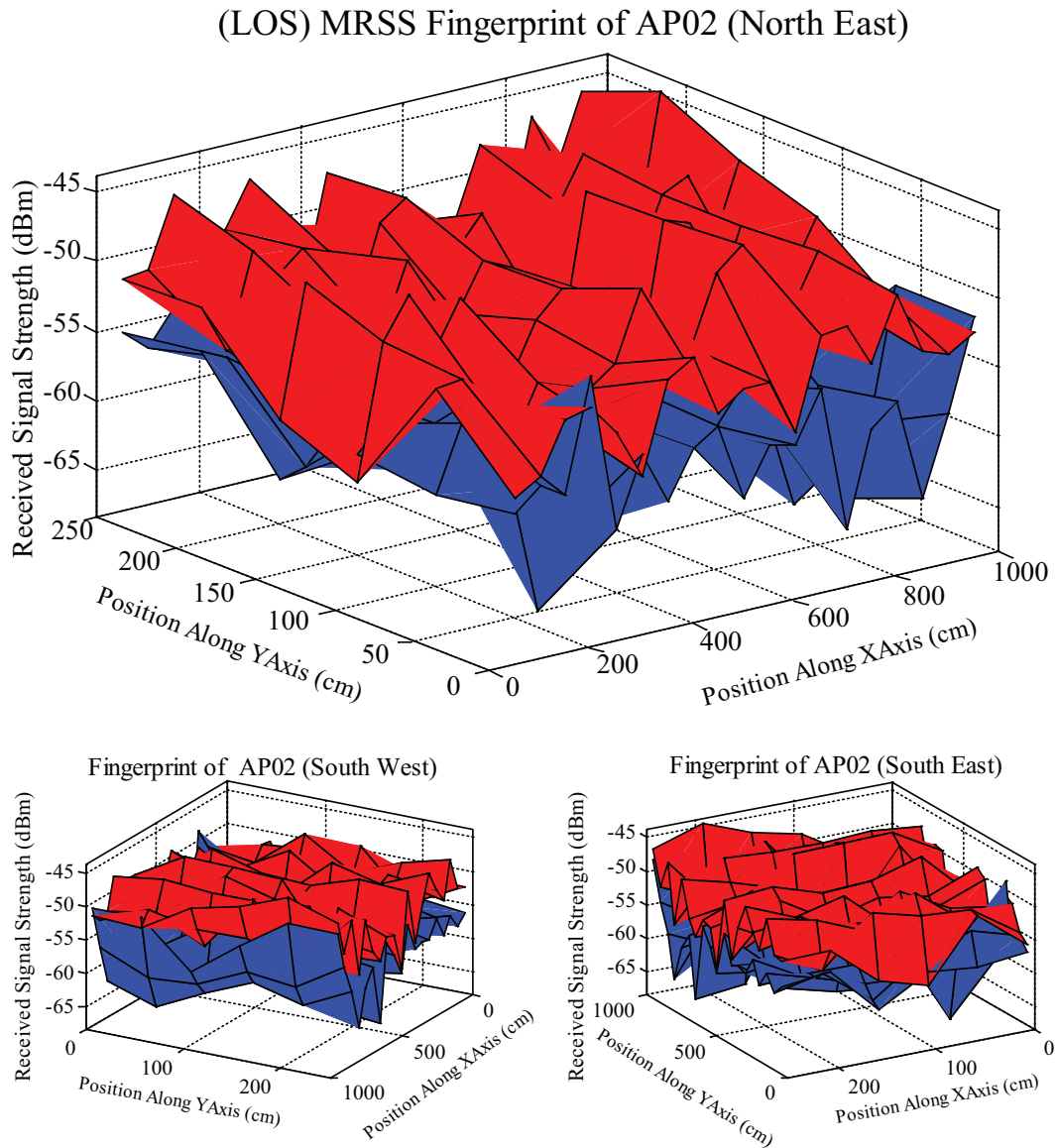
Figure 4.7: The received signal strength of multiband fingerprint from AP 02 (LOS environment). The $x-$axis and $y-$axis shows the location of experimental site in centimeter. The $z-$axis shows the received signal strength level in dBm.

to wavelength property, reflection, diffraction and transmission, which causes the frequency diversity. Figure 4.6 illustrates MRSS time series, of a location close to AP08, from MRSS fingerprint entries. The results show that RSS from 2.4 GHz frequency band of some AP has higher fluctuation than the RSS of 5 GHz frequency band. Moreover, RSS from 2.4 GHz
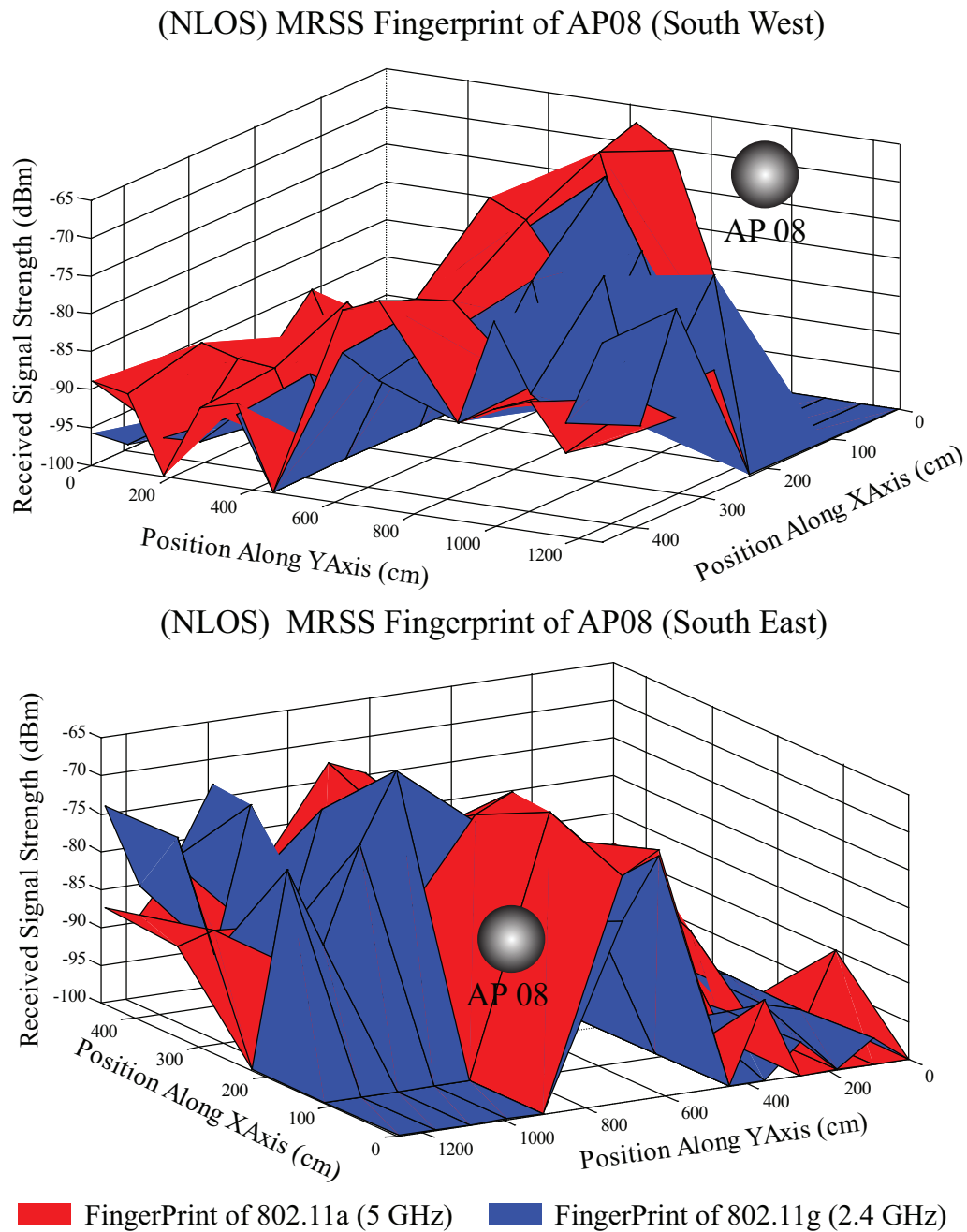
Figure 4.8: The received signal strength of multiband fingerprint from AP 08. The $x-$axis and $y-$axis shows the location of experimental site in centimeter. The $z-$axis shows the received signal strength level in dBm.

frequency of AP08 band shows high fluctuation during human presence, which is caused by EM wave transmission through human body; as described in section 1.4.3.

4.5.2 MRSS Fingerprint

Figure 4.8 shows the $\mathfrak{MF}$ of AP 08 in NLOS environment at Keio University. Upper figure illustrates MRSS fingerprint viewing toward southwest direction of the experimental site, and lower figure illustrates MRSS fingerprint viewing toward south east. The signal from AP08 has no line-of-sight to any positions in fingerprint location (l). Figure 4.8 shows the average RSS level measured at each fingerprint location of 2.4 and 5.2 GHz bands. The result shows that when radio wave transmitted through different material, attenuation of each frequency band was substantially different. At some fingerprint locations, only RSS of 5.2 GHz frequency band is receivable, as a result to wavelength property described in section 1.4.

Furthermore, Fig. 4.8 shows that there are intersections between RSS fingerprints of each frequency band. Thus, deploying frequency diversity on RSS fingerprint, MRSS, is able to increase fingerprint resolution. On the other hand, Figure 4.7 shows the $\mathfrak{MF}$ of AP 02 in LOS environment at The University of Electro-Communications. The results show high similarity between each frequency band.

4.5.3 Frequency Correlation

The proposed system, MRSS fingerprinting, working on the basis that frequency diversity can improve fingerprint resolution. The resolution of fingerprint in section 4.3.3, increases in proportion to degree of independence of measured RSSs. In this section, we analyze the correlation between 2.4 and 5.2 GHz frequency bands, of which both are generated from the same APs, among fingerprint locations by utilizing (4.18).

The fingerprint locations are classified into 3 groups as follows. Firstly, location 1 is laboratory area, NLOS environment with high obstacle denoted by fingerprint locations 1 to 25. Secondly, location 2 is building hallway, NLOS environment with no obstacle, designated as fingerprint locations 26 to 35. Lastly, fingerprint locations 36 to 49 are regarded as location 3 that is in the area of a conference room where two line-of-sights from AP02 exist.

Figure 4.9 illustrates frequency correlation coefficient among fingerprint locations created from 6 units of dual-band AP. The results show that without LOS, all the entire fingerprint locations show low frequency correlation between 2.4 and 5 GHz frequency band.

4.5.4 Correct Estimation Probability

The performance of indoor positioning systems is majorly evaluated by achievable accuracy from positioning estimation. Positioning accuracy achieved from KNN method is relevant to grid sizes of the fingerprint location and correct estimation probability at each nearest
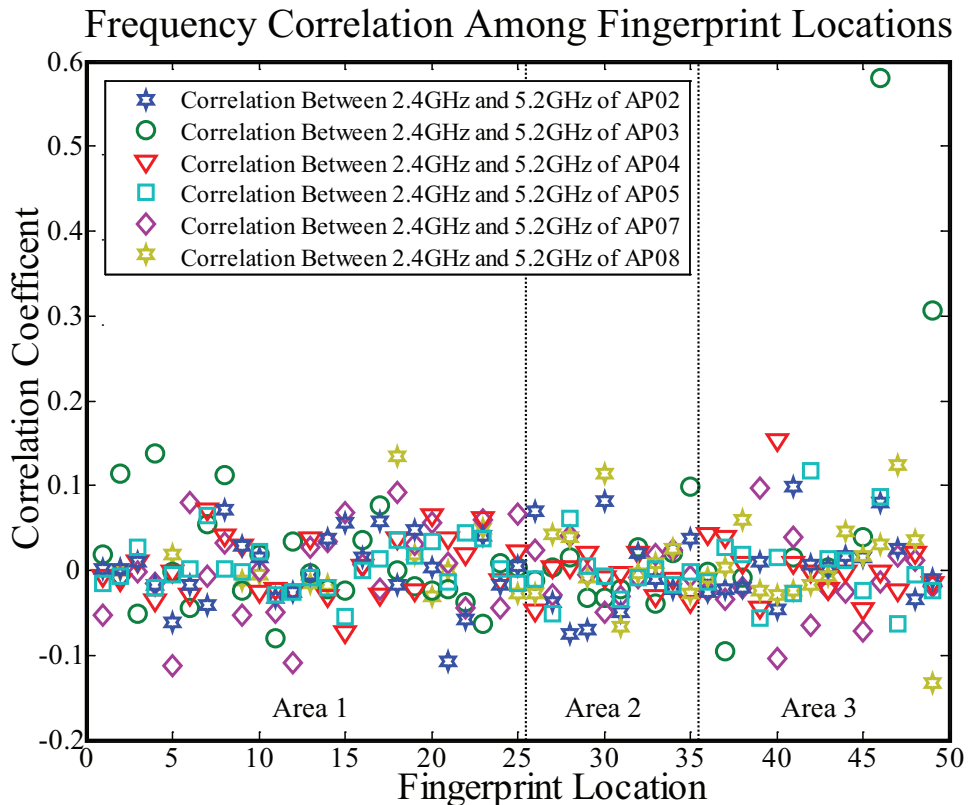
Figure 4.9: Frequency correlation among fingerprint locations, which created from 3 types of area consisting of 49 locations.

position, NCEP, between MRSS fingerprint and instantaneous measured RSS in positioning phase.

Intuitively achievable accuracy is increasing if grid sizes of fingerprint locations become smaller. Nevertheless, with multi-path propagation and dynamic shadowing, the NCEP became very low. This means that the nearest neighbor positions are misclassified into the much further position, and error distance is increased. Thus, the higher the NCEP is, the higher the achievable accuracy can become. In this section, correct estimation probability between the proposed system (MRSS fingerprint), and the conventional single band RSS fingerprint is calculated by (4.19).

Figures 4.10 and 4.11 illustrate NCEP ($P_c^{k,q}$) comparison among K-th nearest position calculated by 4NN method, where $k = 4$ and $q = l, , l + 3$, incorporating with Manhattan (L_1) and Euclidean (L_2) distance as in (4.17). X-axis shows window size ($\mathfrak{W}_{\mathfrak{z}}$) of average RSS per sample ($\mathfrak{S}$) during positioning phase, as in (4.5). Y-axis shows correct estimation probability of each K-th nearest position estimated by 4-NN classifier. The NCEP of 1st, 2nd, 3rd and 4th nearest positions are denoted as $P_c^{4,l}$, $P_c^{4,l+1}$, $P_c^{4,l+2}$ and $P_c^{4,l+3}$, sequentially.
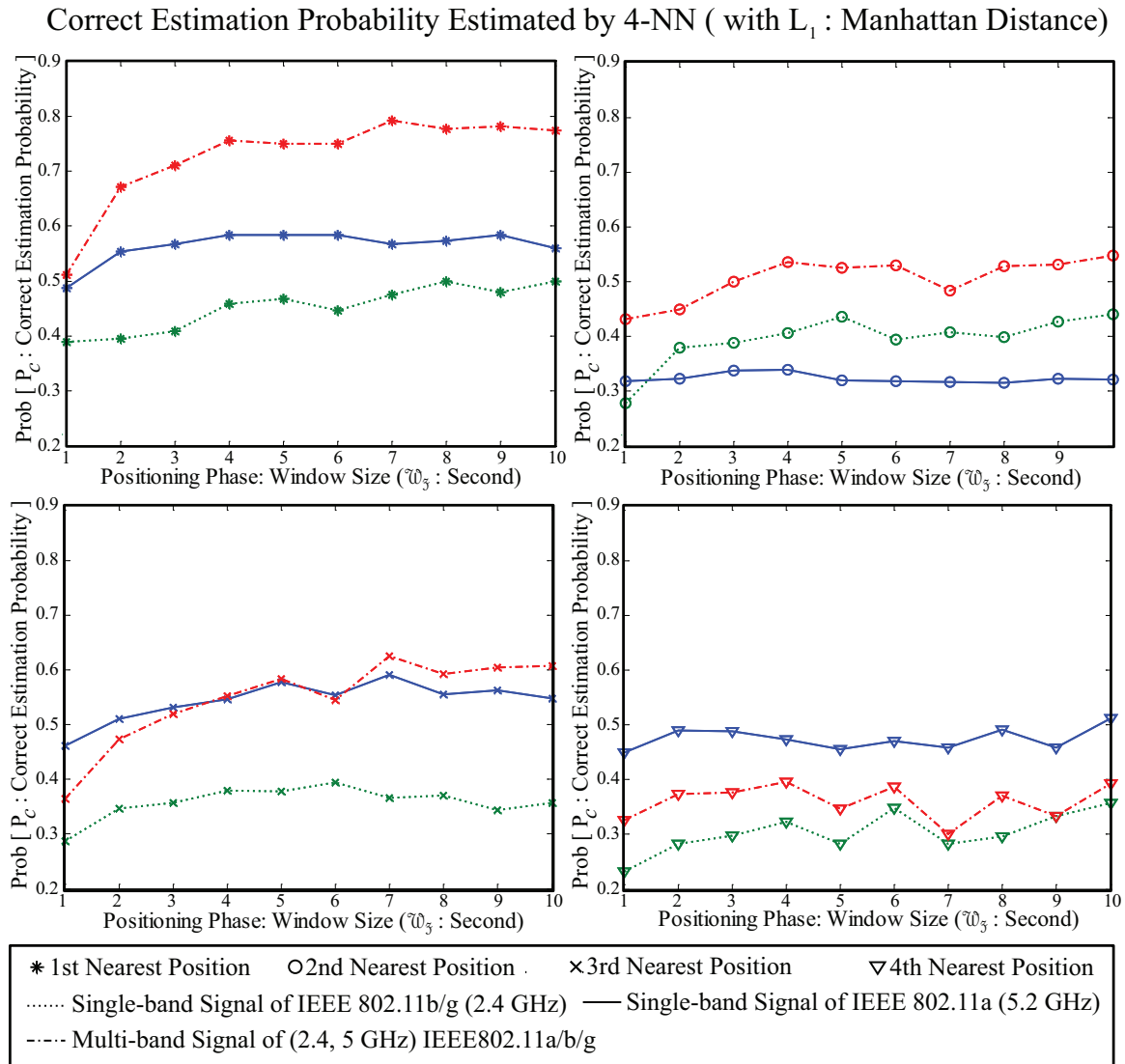
Figure 4.10: Comparison of correct estimation probability at each nearest position, NCEP, achieved by 4NN classifier utilizing Manhattan (L_1) distance.

In Figs. 10, asterisk, circle, cross, triangle symbol represent correct estimation probability of 1st, 2nd, 3rd and 4th nearest positions, respectively.

The results confirm that by deploying frequency diversity on single-band RSS fingerprint, denoted as MRSS fingerprint, the achievable NCEP at 1st and 2nd nearest positions are significantly enhanced over both Manhattan and Euclidean distances. Besides, utilizing Manhattan distance together with KNN method provides significant improvement, comparing with the one achieved by Euclidean distance. The highest achievable NCEP is equal to
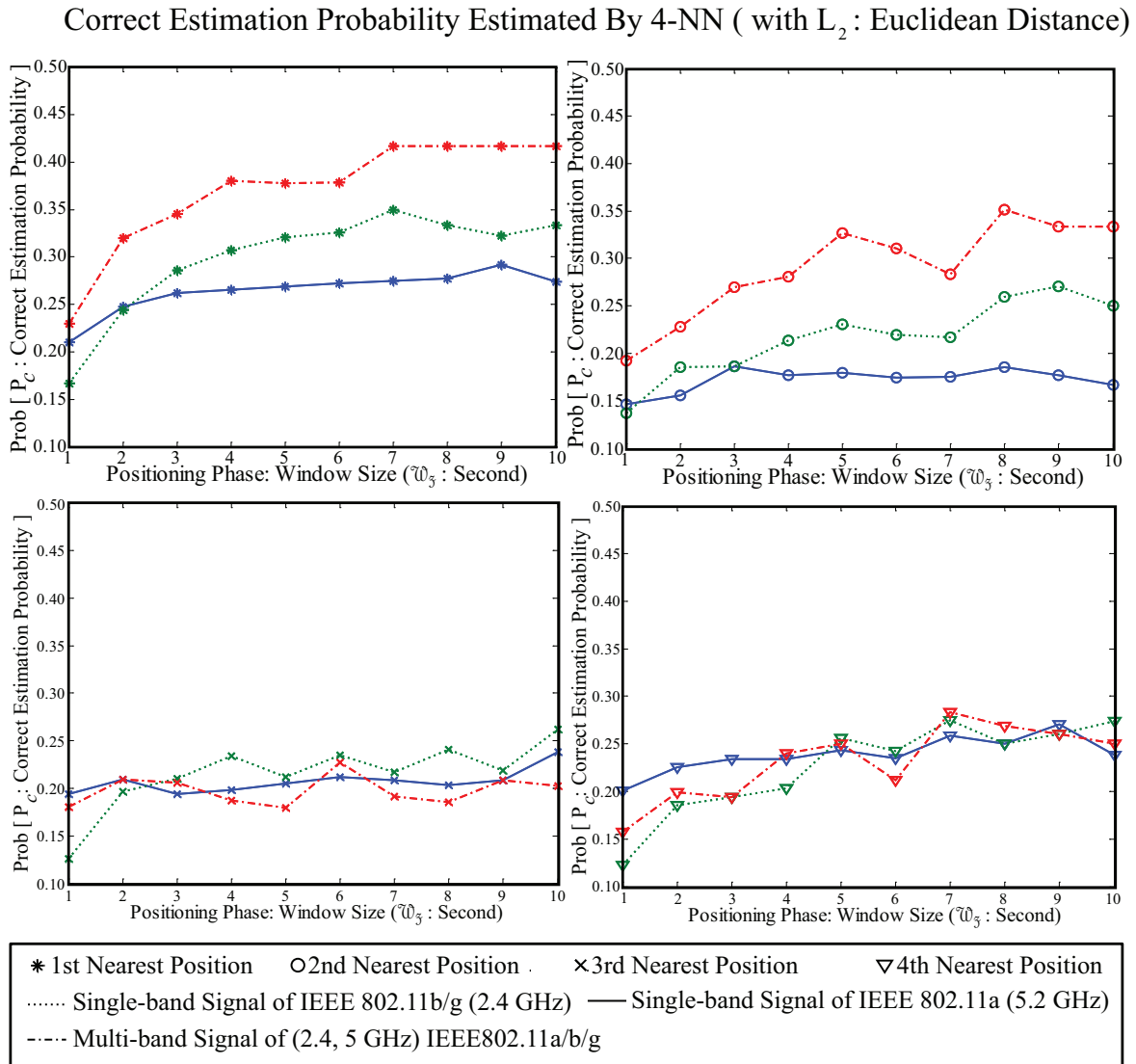
Figure 4.11: Comparison of correct estimation probability at each nearest position, NCEP, achieved by 4NN classifier utilizing Euclidean (L_2) distance.

0.79, which shows enhancement over 67.8 percent comparing with single-band of 2.4 GHz, and 28.6 percent in the case of 5.2 GHz band. Tables 4.6 and 4.7 show comparison of NCEP improvement between conventional single-band RSS fingerprint system and the proposed MRSS fingerprint system.

Table 4.6: Correct Estimation Probability Enhancement at Each Nearest Position Achieved by 4NN Classifier of L_1: Manhattan Distance

$\mathfrak{W}_{\mathfrak{z}}$ (sec)	Percentage of Improvement (L_1: Manhattan Distance)							
	MRSS over IEEE802.11a (%)				MRSS over IEEE802.11g (%)			
	$P_C^{4,1}$	$P_C^{4,2}$	$P_C^{4,3}$	$P_C^{4,4}$	$P_C^{4,1}$	$P_C^{4,2}$	$P_C^{4,3}$	$P_C^{4,4}$
2	21.4	39.2	-7.4	-23.6	70.1	18.4	36.4	32.4
4	29.5	58.5	1.0	-16.5	64.8	32.1	45.2	22.6
6	28.6	66.7	-1.4	-17.7	67.8	34.6	38.5	10.9
8	35.5	67.6	6.7	-24.5	55.6	32.6	60.0	25.0
10	38.3	70.4	10.9	-23.3	54.8	24.3	70.0	10.0

Table 4.7: Correct Estimation Probability Enhancement at Each Nearest Position Achieved by 4NN Classifier of L_2: Euclidean Distance

$\mathfrak{W}_{\mathfrak{z}}$ (sec)	Percentage of Improvement (L_2: Euclidean Distance)							
	MRSS over IEEE802.11a (%)				MRSS over IEEE802.11g (%)			
	$P_C^{4,1}$	$P_C^{4,2}$	$P_C^{4,3}$	$P_C^{4,4}$	$P_C^{4,1}$	$P_C^{4,2}$	$P_C^{4,3}$	$P_C^{4,4}$
2	29.3	46.6	0.0	-11.9	30.8	23.2	6.8	7.2
4	43.1	58.8	-5.3	2.2	23.7	31.7	-20.0	17.9
6	38.9	78.3	7.1	-9.7	16.3	41.4	-3.2	-12.5
8	50.0	90.0	-9.1	7.4	25.0	35.7	-23.1	7.4
10	52.2	100	-15	5.0	25.0	33.3	-22.7	-8.7

4.5.5 Achievable Accuracy

In this section, we evaluate the effectiveness of multiband fingerprint by comparing to the conventional single-band system Fig. 4.5 shows the experimental environment. The triangle symbol shows the location of APs, the circles represent fingerprint location ($\mathfrak{L}$) in the training phase and × symbol represents the experimental location in the positioning phase. We use K-Nearest Neighbor (KNN) classifier to indicate the performance with mean error distance (MED), of which signal distance are calculated by utilizing both Manhattan distance (L_1) and Euclidean distance (L_2) as shown in (4.16) and (4.17). Figure 4.12 illustrates relationship between positioning phase window size ($\mathfrak{W}_{\mathfrak{z}}$) and MED achieved from L_1 and L_2. In Fig. 4.12 the achievable MED among KNN methods are compared with error distance lower bound, which is calculated from experimental position, as illustrated by × symbols in Fig. 4.5, and KNN by assuming that NCEP = 1.

In both L_1 and L_2, achievable mean error distance of conventional methods (single-band of both 2.4 and 5 GHz) decreased in inverse proportion to K-order of KNN method. The
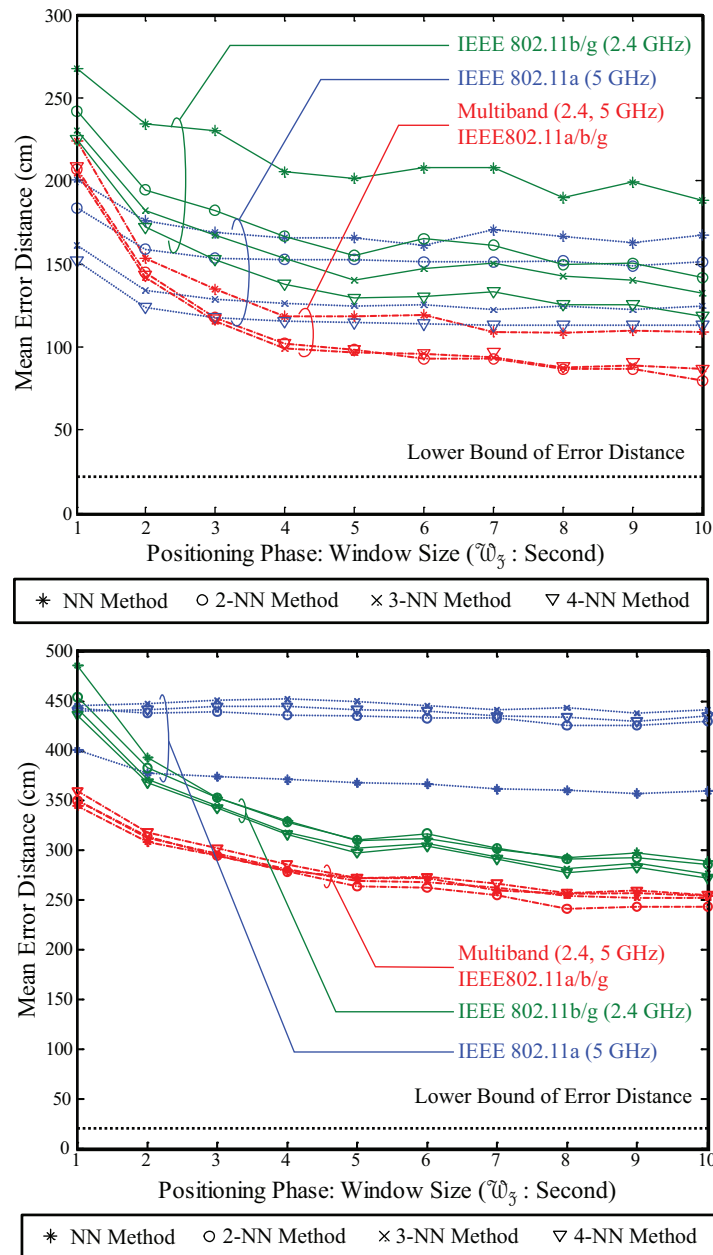
Figure 4.12: The mean error from L_1 and L_2, consequentially, comparison of single band and multiband, among KNN methods. The x-axis shows $\mathfrak{W}_{\mathfrak{z}}$ of the measured MRSS during training phase.

proposed method MRSS fingerprint provides the lowest MED, as the result of increment of achievable NCEP illustrated in Figs. 4.10 and 4.11. Our experimental configuration, 2NN

Table 4.8: Achievable Accuracy Comparison Among Dist(L_1): Manhattan Distance and Algorithms.

Window Size		Dist(L_1): Manhattan Distance			
($\mathfrak{W}_{\mathfrak{z}} = 10$ sec)		NN(cm)	2NN(cm)	3NN(cm)	4NN(cm)
Singleband	5.2 GHz	167.19	151.07	124.81	112.77
	2.4 GHz	188.75	141.63	132.82	118.16
Multiband 5.2, 2.4 GHz		109.03	79.52	86.88	86.47
Mean Error Lower Bound		46.28	19.68	24.49	34.72

Table 4.9: Achievable Accuracy Comparison Among Dist(L_2): Euclidean Distance and Algorithms.

Window Size		Dist(L_2): Euclidean Distance			
($\mathfrak{W}_{\mathfrak{z}} = 10$ sec)		NN(cm)	2NN(cm)	3NN(cm)	4NN(cm)
Singleband	5.2 GHz	359.41	429.04	440.87	434.13
	2.4 GHz	288.53	285.32	275.69	271.32
Multiband 5.2, 2.4 GHz		253.56	243.32	251.83	254.99
Mean Error Lower Bound		46.28	19.68	24.49	34.72

classifier with both L_1 and L_2 provides the lowest MED, which matched our experimental configuration shown in Fig. 4.5. In addition, the results confirm that the proposed system, MRSS, provide estimated accuracy improvement over 50 % in the case of utilizing L_1 and over 10 % in the case of utilizing L_2. Details are provided in Tables 4.8 and TB:Mean2. In summary, Figs. 4.10, 4.11 and 4.12 show that achievable accuracy is increased in proportion to NCEP. MED approaches mean error distance lower bound as NCEP at every positions approaching 1, as shown in Tables 4.8 and 4.9.

The achievable MED is varied in different experimental configurations; such as the number of APs, and fingerprint location grid sizes; as reported in [9][12][31][32]. However, in this subsystem, we proved that frequency diversity enhances positioning accuracy. In NLOS environment, correlation between frequency bands are low, thus, the fingerprint resolution is enhanced. During positioning phase, the increment of fingerprint resolution provides higher NCEP, which increases in proportion to achievable accuracy.

4.6 Conclusion

We propose MRSS fingerprinting based indoor location subsystem, which deploy frequency diversity over the conventional RSS fingerprint system. The advantage of fingerprinting

approach is that transmitter locations are not required for positioning estimation; on the other hand database of utilization area must be premeasured. Thus, with multi-frequency band capable receiver such as cognitive radio terminal or dual-band WLAN receiver together with fingerprinting approach, will be able to access to numerous frequency bands. Hence, positioning estimation can be achieved without installing extra wireless infrastructure.

We proved that achievable accuracy can be enhanced as a result of frequency diversity using dual band WLAN (2.4 and 5.2 GHz are simultaneously transmitted) transmitters from the same locations. The experiments were conducted to confirm our hypothesis, in the area of 103 m^2 with 6 units of APs; as shown in Fig. 4.5.

The accuracy achieved from fingerprinting approach increased in proportion to its resolution. In order to enhance fingerprint resolution, multiband received signal strength, MRSS, fingerprint, MF, were created by using both frequency and time diversity. The increment of fingerprint resolution hypothesis was supported by frequency correlation analysis, provided in section 6.3, which showed very low correlation between frequency bands among fingerprint locations.

Effectiveness of the proposed system was evaluated by analyzing correct estimation probability at each nearest position, NCEP, and achievable accuracy estimated by Mean Error Distance, MED. The MED varied with experimental sites and configurations, such as number of APs, fingerprint location grid sizes. On the other hand, NCEP is more generalized. The results confirmed that by adding the effect frequency diversity at the nearest position, NCEP of the proposed system increased over 50 %. In addition, estimated MED is decreased in proportion with NCEP.

In conclusion, MRSS fingerprinting based indoor positioning system created from both 2.4 and 5.2 GHz. shows significant improvement over the conventional single-band RSS fingerprint system. The higher accuracy contributes to the correct estimation between RSS in positioning phase $\mathfrak{S}$, and $\mathfrak{MF}$ in MRSS fingerprint entry.

Chapter 5

Conclusion and Future Development

This dissertation has developed a solution architecture as a design tool and recommends a set of design guidelines in order to accelerate the deployment process. The proposed architect is developed based on eco-friendly approach, no extra infrastructure is introduced in order not to create extra carbon footprint. Moreover, the operational and installation cost can be minimized owing to our infrastructure less proposal. The architecture is well balance between the accuracy, the location granularity, capacity, operational cost and complexity. The proposed architecture has three subsystems, which are VLC based positioning system, MRSS fingerprinting system and machine learning algorithms that use to enhance the two preceding subsystems.

The VLC based positioning subsystem was investigated in chapters 2 and 3. The systematic studies on both empirical and analytical were used to analyze the VLC based positioning system, and discover its unique properties. We define two properties, FOV Limit and Sensitivity Limit, of which are the preliminary requirement to enable our proposed switching estimated receiver position (SwERP) scheme. The results show more than 80% accuracy improvement over the conventional visible light identification system (VLID). The uniqueness of this proposed subsystem is its low computation complexity and high accessibility; due to the reason that only one transmitter is required for positioning estimation. In chapter 3, we introduced two additional subsystems to fulfill SwERP scheme requirement.

Based on exhaustive measurements in chapter 4, we found out that MRSS random process is non-stationary, the mean is more or less constant and could be used as the fingerprint of a location. We found a great improvement by incorporating frequency diversity into conventional RSS fingerprinting. From theoretical and empirical point of view, we proved that MRSS can improve positioning accuracy over 50% compare to the conventional RSS fingerprinting. MRSS fingerprinting can improve correct estimation probability of 1 NN up to 80%, which is the key factor to the accuracy improvement. The greatest advantage of MRSS fingerprinting subsystem is any existing infrastructure can be utilized as the sources of signal.

5.1 Contributions

This section list the major contribution of this thesis:

- The proposed architecture does not require any extra infrastructure. Therefore, investment and operational cost can be minimized to ensure the success of implementation. Moreover, from this approach minimal carbon footprint is created from additional location information server. Thus, we proved that the proposed architecture is an eco-friendly solution.

- We made both theoretical and analytical studied to study the proposed systems characteristics, which are based on our extensive measurement. We used the unique characteristic of each studied subsystem to proposed positioning schemes that can greatly enhance positioning accuracy. Moreover, both of the subsystems are compliment to each other.

- We provided an example of a design guideline which will be useful for designing the indoor positioning by identifying major parameters that contribute to the performance of both indoor positioning subsystem.

- We introduced machine learning algorithms to ensure the lifetime evolution of the proposed architecture. Machine learning algorithms are applied in many stages ranging from analyzing the subsystems characteristic to positioning estimation. Furthermore, both of the selected core subsystem technologies are designed based on daily life basis infrastructures that provide illumination and communication.

5.2 Future Development of The Proposed Architecture

The research in this dissertation provides methodology for designing and implementation of core system architecture for lifetime evolution indoor positioning system. The current algorithms used in the proposed architecture for positioning estimation are not optimized. The main purposes of the previously proposed algorithms are used to illustrate that the proposed system can operate correctly as our objective. Thus, there are still great rooms for accuracy improvement.

The propose solution architecture is still has limitations. Firstly, VLC based indoor positioning subsystem has an unavoidable communication barrier, owing to the visible light property which cannot penetrate through opaque object. Thus, we introduce MRSS fingerprinting subsystem to compensate this lack of accessibility. Secondly, the proposed MRSS fingerprinting subsystem also has disadvantage, of which is the requirement abundant manpower during training phase. Both of the subsystem disadvantages can be resolved by using VLC based positioning system to calibrate MRSS fingerprinting during training phase, as shown in Fig. 5.1. However, fully extent investigation the mentioned method is required.
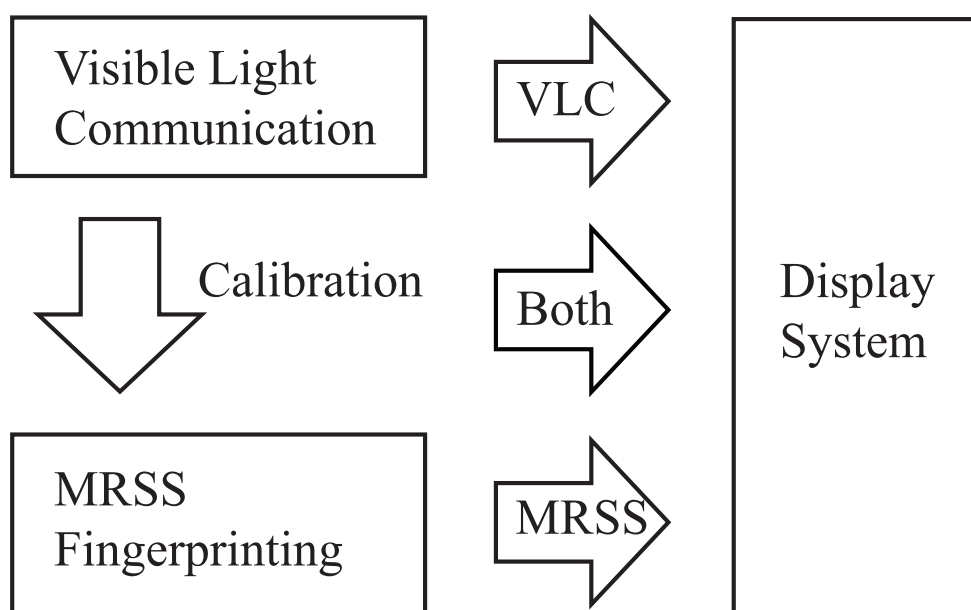
Figure 5.1: The future posibility of the proposed indoor positioning architect block diagram, VLC based positioning system is used to calibrate MRSS fingerprinting.

Bibliography

[1] H. Saito,"Wide Area Ubiquitous Network: New Wireless Network for Sensors and Actuators," *NTT Technical Review*, vol. 6, no. 3, pp. 1-5, 2008.

[2] J. Mitola III and G. Q. Jr. Maguire,"Cognitive radio: making software radios more personal," *Personal Communications, IEEE*, vol. 6, no. 4, pp. 13-18, Aug. 1999.

[3] E. Dahlman, S. Parkvall, and J. Skold,*4G: LTE/LTE-Advanced for Mobile Broadband*, Academic Press, 1 edition, 2011.

[4] P. Krishnamurthy, "Position Location in Mobile Environments," *NSF Workshop on Context-Aware Mobile Database Management*, Jan. 2002.

[5] T. S. Rappaport, J. H. Reed, and B. D. Woerner, "Position location using wireless communications on highways of the future," *Communications Magazine, IEEE*, vol. 10, no. 34, pp. 33-41, Oct.1996.

[6] K. Pahlavan, and X. Li and J.P. Makela, "Indoor geolocation science and technology," *Communications Magazine, IEEE*, vol. 40, no. 2, pp. 112-118, Feb. 2002.

[7] J. Hightower, and G. Borriello, "Location systems for ubiquitous computing," *Computer*, vol. 34, no. 8, pp. 57-66, Aug. 2001.

[8] A. M. Ladd, K. E. Bekris, A. Rudys, L. E. Kavraki and D. S. Wallach, "Robotics-Based Location Sensing Using Wireless Ethernet," *Wireless Networks*, vol. 11, pp. 189-204.

[9] K. Kaemarungsi, *Design of Indoor Positioning Systems Based on Location Fingerprinting Technique*, PhD thesis, University of Pittsburgh, 2005.

[10] M. J. Meyer and et al., "Wireless enhanced 9-1-1 service making it a reality," *Bell Labs Technical Journal*, 1996.

[11] A. Bensky, *Wireless Positioning Technologies and Applications*, Artech house, 2008.

[12] M. A. Youssef, A. Agrawala, and A. U. Shankar, "WLAN location determination via clustering and probability distributions," *Pervasive Computing and Communications, 2003. (PerCom 2003). Proceedings of the First IEEE International Conference on*, pp. 143-50, Mar. 2003.

[13] M. Deffenbaugh, J. G. Bellingham, and H. Schmidt, "The relationship between spherical and hyperbolic positioning," *OCEANS '96. MTS/IEEE. 'Prospects for the 21st Century'. Conference Proceedings*, vol. 2, pp. 590-595, Sep. 1996.

[14] P. Bahl, and V. N. Padmanabhan, "RADAR: an in-building RF-based user location and tracking system," *INFOCOM 2000. Nineteenth Annual Joint Conference of the IEEE Computer and Communications Societies. Proceedings. IEEE*, vol. 2, pp. 775-784, 2000.

[15] h T. Roos, P. Myllymaki, H. Tirri, P. Misikangas, and J. Sievanen, "A probabilistic approach to wlan user location estimation," *International Journal of Wireless Information Networks*, vol. 9, no.3, pp.155-164, Jul. 2002.

[16] R. Want, A. Hopper, V. Falcao, and J. Gibbons, "The active badge location system," *ACM Transactions on Information Systems*, vol. 40, no. 1, pp. 91-102, Jan. 1992.

[17] A. Harter, A. Hopper, P. Steggles, A. Ward, and P. Webster, "The anatomy of a context-aware application," *in Proc. ACM International Conference on Mobile Computing and Networking (MOBICOM99)*, Aug. 1999.

[18] J. Hightower, R. Want, and G. Borriello, "An indoor 3D location sensing technology based on RF signal strength," *Techical Report UW CSE 2000-02-02*, Feb. 2000.

[19] N. B. Priyantha, A. Chakraborty, and H. Balakrishnan, "The cricket location-support system," *in Proc. ACM International Conference on Mobile Computing and Networking (MOBICOM'00)*, pp. 32-43, Aug. 2000.

[20] H. R. Anderson, *Fixed Broadband Wireless System Design*, John Wiley, Urbana, Chicago, and London, 1 edition, Feb. 2003.

[21] R.J. Luebbers, "Finite conductivity uniform GTD versus knife edge diffraction in prediction of propagation path loss," *IEEE Trans. Antennas and Propagation*, vol. AP-32, no. 1, pp. 70-76, Jan. 1984.

[22] M. A. Youssef, A. Agrawala, and A. U. Shankar, "WLAN location determination via clustering and probability distributions," *in Proc. IEEE International Conference on Pervasive Computing and Communications (PerCom'03)*, vol. 2, pp. 23-26, Mar. 2003.

[23] J. D. Parsons, *Mobile Radio Propagation Channel*, John Wiley, Chichester, U.K., edition 2, Feb. 2000.

[24] T. Komine and M. Nakagawa, "Fundamental analysis for visible-light communication system using LED lights," *IEEE Trans. Consumer Electronics*, vol. 50, no. 1, pp. 100-107, Feb. 2004.

[25] S. Sesia, I. Toufik, and M. Baker, *LTE, The UMTS Long Term Evolution: From Theory to Practice*, Wiley, Apr. 2009.

[26] V.Badea and R.Eriksson, *Indoor navigation with pseudolites (fake GPS sat.)*, Master thesis, Linkpings University, 2005.

[27] Japan Electronics and Information Technology Industries Association, standard CP-1221, Mar. 2007.

[28] Japan Electronics and Information Technology Industries Association, standard CP-1222, Jun. 2007.

[29] T. Komine and M. Nakagawa, "Integrated system of white LED visible-light communication and power-line communication," *IEEE Trans. Consumer Electronics*, vol. 49, no. 1, pp. 71-79, Feb. 2003.

[30] H. Yin and D. J. Richardson, *Optical Code Division Multiple Access Communication Networks: Theory and Applications*, Springer, edition 1, Feb. 2009.

[31] S. Saha, K. Chaudhuri, D. Sanghi, and P. Bhagwat, "Location Determination of a Mobile Device using IEEE 802.11b Access Point Signals," *in Proc.IEEE WCNC'03*, pp. 1987-1992, Mar. 2003.

[32] P. Prasithsangaree, P. Krishnamurthy, and P. K. Chrysanthis, "On Indoor Position Location with Wireless LANs," *in Proc. IEEE Personal, Indoor and Mobile Radio Communications Symposium (PIMRC'02)*, pp.1987-1992, Sep. 2002.

[33] P. Castro, P. Chiu, T. Kremenek, and R. Muntz, "A probabilistic room location service for wireless networked environments," *in Proc. ACM International Conference on Ubiquitous Computing (UbiComp'01)*, Sep. 2001.

[34] N. J. Nilsson, *Introduction to Machine Learning*, Draft of Incomplete Notes.

[35] Osram declare banned on incandescent lamp by 2012, *EU-directive*, 2005.

[36] J.Kanter, "Europe's Ban on Old-Style Bulbs Begins," *The New York Times*, Aug. 31, 2009.

[37] Philips declare phase out of general lighting service, based on *Energy Independence and Security Act (EISA)*, Section−321, 2007.

[38] M.Lavelle, "FAQ:The End of the Light Bulb as We Know It ", U.S.News & World Report, Dec. 19, 2007.

[39] Samsung Electronics, ETRI, VLCC and University of Oxford, "Visible Light Communication - Tutorial ", IEEE 802.15 TG7, Jan. 2009.

[40] J.M. Kahn and J. R. Barry, "Wireless Infrared Communications," Proc. of the IEEE, vol. 85, pp. 265-298. Feb. 1997.

[41] L. Garcia, *Probability and Random Processes for Electrical Engineering*, Prentice Hall, 2nd Edition, Aug. 1993.

[42] V. Torra, Y. Narukawa, *Modeling Decisions Information Fusion and Aggreation Operators*, Springer. Jun. 2007.

[43] K. Smith, "On the Standard Deviations of Adjusted and Interpolated Values of an Observed Polynomial Function and its Constants and the Guidance They Give Towards a Proper Choice of the Distribution of the Observations," *Biometrika*, vol.12, no.1, pp. 185.

[44] A. Bensky, *Wireless Positioning: Technologies and Applications*, Artech House, 2007.

[45] J. A. Salehi, F. R. K. Chung, and V. K. Wei, "Optical Orthogonal Codes: Design, Analysis, and Applications," *IEEE Trans. on Information Theory*, Vol.35, No.3, pp. 595 - 605, May 1989.

[46] J. A. Salehi and C. A. Brackett, "Code division multiple-access techniques in optical fiber networks-part II: Systems performance analysis," *IEEE Trans. on Communications*, Vol.37, No.8, pp. 834-842, Aug. 1989.

[47] S. Tsuzuki, N. Takeichi, M. Hamada, and Y. Yamada, "A Proposal of Synchronization Beacon Systems Over Power-Line for Indoor Fine-Grained Localization," *IEEE International Symposium on Power Line Communications and Its Applications*, pp. 143-148, Oct. 2006.

[48] K. Watanabe, D. Umehara, S. Denno, and M. Morikura, "An Initial Acquisition Method for Channel Synchronization on In-Home Power Line Communications," *IEEE International Symposium on Power Line Communications and Its Applications*, pp. 137-142, Apr. 2009.

[49] A. J. C. Moreira, R, T, Valadas and A. M. de Oliveira Duarte, "Optical Interference Produced by Artificial Light," *Journal on Wireless Networks*, vol. 3, pp. 131-140, 1997.

[50] X. Qu, S.C. Wong and C.K. Tse, "Noncascading Structure for Electronic Ballast Design for Multiple LED Lamps with Independent Brightness Control," *IEEE Trans. on Power Electronics*, vol.25, no.2, pp. 331-340, Feb. 2010.

[51] J. Nocedal and S. J. Wright, *Numerical Optimization*, Springer Publishing, 2000.

[52] C. Sertthin, T. Ohtsuki and M. Nakagawa,"6-Axis Sensor Assisted Low Complexity High Accuracy-Visible Light Communication Based Indoor Positioning System," *IEICE Tran. Commun.*, Vol. E93-B No. 11, pp. 2879-2891, Nov. 2010.

[53] R. Battiti, M. Brunato, and A. Villani,"Statistical Learning Theory for Location Fingerprinting in Wireless LANS," *ELSEVIER, Computer Networks*, vol 47, no. 6, pp. 825-845, Apr. 22, 2005.

[54] R. Prasad and M. Ruggieri, *Technology Trends in Wireless Communications*, Artech House, Apr. 2003.

[55] IEEE Computer Society Working Group 802.16,"IEEE Recommended Practice for Local and Metropolitan Area Networks Part 16: Air Interface for Fixed Broadband Wireless Access Systems," *IEEE Standard 802.162001. Institute of Electrical and Electronic Engineers*, Apr. 2002.

[56] IEEE Computer Society Working Group 802.16,"IEEE Recommended Practice for Local and Metropolitan Area Networks Coexistence of Fixed Broadband Wireless Access Systems," *IEEE Standard 802.16.22001, Institute of Electrical and Electronic Engineers*, Sep. 2001.

[57] V. Erceg, et al."An empirically based path loss model for wireless channels in urban environments," *IEEE Journal of Selective Areas in Communications*, vol. 17, no. 3, pp. 12051211, Jul. 1999.

[58] IEEE 802.16 Working Group. "Channels models for fixed wireless applications," *Document 802.16.3c-01/29r4*. Jul. 2001.

[59] EURO-COST-231, Revision 2, "Urban transmission loss models for mobile radio in the 900 and 1800MHz bands," Sep. 1991.

[60] M. Hata, "Empirical formula for propagation loss in land mobile radio services," *IEEE Transactions on Vehicular Technology*, vol. VT-29, no. 3, pp. 317325, Sep. 1981.

[61] Y. Okumura, E. Ohmori, T. Kawano, and K. Fukuda, "Field strength and its variability in VHF and UHF land-mobile radio-service," *Rev. Elec. Communications Lab.*, vol. 16, no.910, Sep. 1968.

[62] R.G. Kouyoumjian and P.H. Pathak, "A uniform theory of geometric diffraction for an edge in a perfectly conducting surface," *Proceedings of the IEEE*, vol. 62, pp. 14481461, Nov. 1974.

[63] C.Oestges, N.Czink, B.Bandemer, P.Castiglione, F.Kalten-berger and A.Paulraj, "Experimental Characterization of Indoor Multi-Link Channels," *in Proc. IEEE Indoor and Mobile Radio Communications Symposium (PIMRC'09)*, Sep. 2009.

[64] K. Kaemarungsi and P.Krishnamurthy, "Modeling of Indoor Positioning Systems Based on Location Fingerprinting," *IEEE INFOCOM'04*, Mar. 7-11, 2004.